FLUCTUATIONS AND PATTERNS IN ULTRATHIN FLUID FILMS

ENRIQUE RODRÍGUEZ FERNÁNDEZ

A dissertation submitted by in partial fulfillment of the requirements
for the degree of Doctor of Philosophy in

Mathematical Engineering

Universidad Carlos III de Madrid

Advisor: Rodolfo Cuerno Rejado

Leganés, March 2022

Agradecimientos

Finalizar la escritura de la memoria de esta tesis cierra simbólicamente un período de 6 años transitado junto a muchas personas a las que tengo mucho que agradecer.

En primer lugar a mi director, Rodolfo, por haberme dado la oportunidad de embarcarme en este proyecto, por su infinita dedicación, paciencia y apoyo y sobre todo por lo fácil y agradable que ha sido trabajar junto a él. Sin todo ello hubiera sido imposible recorrer un camino tan difícil. El mejor director que podría haber imaginado tener. También a los profesores del departamento de Matemáticas junto a los que he podido dar mis primeros pasos como docente, especialmente a Julio Moro, con quien fue un placer estrenarme en mi primer curso de álgebra lineal.

A los compañeros con los que he compartido el despacho 2.1.D14. Me llevo un muy buen recuerdo de los primeros años con Carla, del maravilloso humor de Yanely, del inestimable apoyo y calidez de Alejandro y de los buenos momentos y tertulias compartidos con Jorge y Juan.

A las personas que me han acompañado en los años que he pasado en Madrid. La estancia hubiera sido muy dura sin la compañía y el calor de grandes amigas como Cris, mi nexo entre la vida cántabra y la madrileña, o Patri, la mejor compañera de piso que he tenido y que después se ha convertido en (si cabe) aún mejor amiga. Y la mención más importante, sin duda, la de Álvaro (y Trudó), con quienes he tenido la enorme suerte de compartir la mayor parte de este camino y a quienes debo los momentos más felices de estos años.

A los amigos que llegaron de lejos para iluminar los momentos más duros: Marcos, Alejandro, Rubén, Andrés, Jaime y muchos más.

A los viejos amigos que en la distancia no han dejado nunca de estar ahí y cuyos brazos me han acogido de vuelta y han marcado la diferencia en este último año que no hubiera podido imaginar sin ellos: Sandra, Agustín, Ana, Esther, Jony, Noelia, Rocío...

Y dejando para el final lo más importante, a mi familia: a mi hermano, a mis padres, a mi abuela. A quienes más debo sin duda haber llegado hasta aquí.

Contents

Introduction

Self-organization processes, in which some form of collective behavior arises from local interactions in a physical system, are promising mechanisms in the context of manufacturing at ultra small scales, where processing techniques are technically challenging. In many cases, the approach is to induce self-organization or self-assembly phenomena on the system surface —which indeed acquires an increased importance at small scales because of the enhanced surface-to-volume ratio— as a result of which a desired surface morphology is achieved, with different properties depending on its intended application.

In this thesis, we consider two important examples of self-organization processes which take place at the surfaces of many small non-equilibrium systems. One of them, kinetic roughening, reflects the dominance of fluctuations in the surface morphology, with strong correlations which are quite similar to those of an equilibrium system at a continuous phase transition. The second, opposite self-organization process is the formation of ordered patterns. In the thesis, we will deal with the control of the level and type of various surface properties, like roughness and other, and the conditions for the emergence of a varying degree of spatial order in patterns via spontaneous physical processes.

We work in the context of ultrathin fluid films on solid substrates, focusing on the role of the physical effects that become relevant at these very small scales —but not so much at larger scales—, while other loose their relevance. One of these aspects is the thermal noise. The other one is the interaction between the fluid surface and the substrate, that play a key role in the two reference physical systems we are going to study: an ultrathin fluid film falling down an inclined plane —where the dynamics of the fluid surface follows the celebrated Kuramoto-Sivashinsky (KS) equation— and a ferrofluid ultrathin film under a magnetic field.

Both kinetic roughening and pattern formation usually exhibit some kinds of universal behavior. The universality classes in the kinetic roughening processes that occur in several approximations of the KS equation are widely studied in this the-

sis. These universality classes are characterized by both how the fluctuations scale with space and time and how these fluctuations are statistically distributed. We will deal with the emergence of symmetries in the fluctuation distributions that are unexpected considering the bare microscopic interactions; the non-trivial relation between the universality class of closely related models; with a novel physical mechanism that induces the transition between different universality (sub)classes as the system temperature and hence the dominant nature of the fluctuations (chaotic or stochastic) changes, and finally with some anomalous kinetic roughening processes in the limit of vanishing viscosity and surface tension. Finally, on the other hand, the formation of highly ordered patterns is assessed in the context of ultrathin ferrofluid films under a magnetic field, due to the spontaneous physical break-up of the film into drops. The conditions under which higher levels of order are achieved will be described. This is intended as a proof-of-concept, previous step that could encourage experiments being performed for this type of systems.

The thesis is divided into eight chapters; Chapters 1 to 3 introduce the phenomena, models and tools which will be considered in Chapters 4 to 8, each one with its own conclusions section. In the final chapter, the main conclusions are summarized from a unified perspective, and future research lines are also discussed.

We next explain briefly the content of each one of the thesis chapters:

- In Chapter 1 the self-organization processes which are assessed in several thin film contexts throughout this thesis are discussed. On the one hand, the spontaneous evolution towards pattern formation, focusing on the level of order achieved, and on the other hand the evolution towards highly disordered and scale invariant systems, namely, kinetic roughening.

- In Chapter 2, the derivation of the Kuramoto-Sivashinsky (KS) equation in the context of a thin fluid film falling down an inclined slope is discussed in detail. Further considerations to be taken into account when the fluid is not thin but *ultra*thin are made. Several equations related with particular cases of the fluid film falling down an inclined slope context, which will be assessed elsewhere in the thesis, are also presented.

- In Chapter 3, the main numerical and analytical tools used throughout this thesis are presented. On the one hand, numerical methods for the integration of the different thin film models. Weakly nonlinear equations are integrated by

means of a pseudo-spectral method, while strongly nonlinear models are integrated in real space using semi implicit finite-difference methods. Analytical methods based on dynamic renormalization group (DRG) for the study of the asymptotic behavior of critical behavior are also discussed.

- In Chapter 4, the universality class of kinetic roughening for the Burgers equation with non conserved noise is assessed, focusing on the fluctuation statistics which result to be Gaussian, hence restoring the up-down symmetry which was not present in the nonlinear term and allowing for exact linear approximations in terms of the universality class.

- In Chapter 5, the universality class of the Burgers equation with conserved noise is assessed and put in contrast with the universality class of the KPZ equation. It is shown how although the relation between the scaling exponents from both equations is straightforward, this is not the case for the fluctuation statistics.

- In Chapter 6, a novel transition between two different universality subclasses is assessed in the context of an ultrathin fluid film falling down an inclined slope under thermal fluctuations, with the temperature being the parameter that governs that transition. A parallel transition between chaotic and stochastic nature of the fluctuations, which exhibit different probability distributions on each universality subclass, is demonstrated.

- In Chapter 7, the Burgers and KPZ equations are studied in the zero viscosity limit. A novel universality class with anomalous scaling behavior is described for the inviscid KPZ case in 1D. A discrete model based on the evolution of an Ising system that seems to belong to the same universality class as the inviscid KPZ equation is also presented.

- In Chapter 8, the formation of patterns in ultrathin ferrofluid films is assessed, focusing on the role of the interaction between the fluid and the substrate. The conditions for which the highest level of order is achieved are described.

Published articles

1. E. Rodríguez-Fernández and R. Cuerno, *Gaussian statistics as an emergent symmetry of the stochastic scalar Burgers equation*, Phys. Rev. E **99**, 042108 (2019). DOI: 10.1103/PhysRevE.99.042108.
   The contents published in this paper are included in Chapter 4. This article is also available in arXiv.org:1809.02158, where a former version is titled *Gaussian statistics as an emergent symmetry far from equilibrium.*

2. E. Rodríguez-Fernández and R. Cuerno, *Non-KPZ fluctuations in the derivative of the KPZ equation or noisy Burgers equation*, Phys. Rev. E **101**, 052126 (2020). DOI: 10.1103/PhysRevE.101.052126.
   The contents published in this paper are included in Chapter 5. This article is also available in arXiv.org:1905.00081, where it is titled *The derivative of the Kardar-Parisi-Zhang equation is not in the KPZ universality class.*

3. E. Rodríguez-Fernández and R. Cuerno, *Transition between chaotic and stochastic universality classes of kinetic roughening*, Phys. Rev. Research **3**, L012020 (2021). DOI: 10.1103/PhysRevResearch.3.L012020.
   The contents published in this paper are included in Chapter 6. This article is also available in arXiv.org:2009.11804.

Financial support

Chapter 1

Self-organization processes in thin fluid films

Surface dynamics has attracted the interest of physicist and engineers during the last decades. Some properties of materials, like heat and mass transport, or electronic and optical properties, are influenced by the morphology of their physical surface at small scales. In this context, one important context within surface physics is the physics of thin fluid films.

Novel material manipulation and characterization techniques have allowed the control of fluid dynamics at the micro and nano scales; this has been the origin of microfluidics [4] and nanofluidics [5]. These new disciplines have raised high expectations due to the wide range of potential applications, e.g. to biomedicine, energy, the environment, electronics, photonics, and drug delivery systems [6, 7]. These new application areas require novel physics-based approaches for engineering and fabrication that go beyond the traditional methods. Self-organization processes (complex behavior of surface dynamics in which the material self-organizes itself to achieve e.g. a high level of spatial order, or else self-affine scale-free disordered configurations) are promising as new mechanisms for the manufacturing of these microscopic and nanoscopic systems.

Fluid mechanics is a field in which many self-organization phenomena can be found [7]. In this thesis, two opposite behaviors are going to be studied in the frame of the dynamics of ultrathin fluid films: self-organization towards high spatial order (formation of ordered patterns), which appears in fluid systems like convection rolls and ferrofluids, and self-organization towards high spatiotemporal disorder (kinetic roughening), which occurs in several fluid systems due to e.g. turbulence.

Throughout this thesis we will deepen the study of several thin fluid film sys-
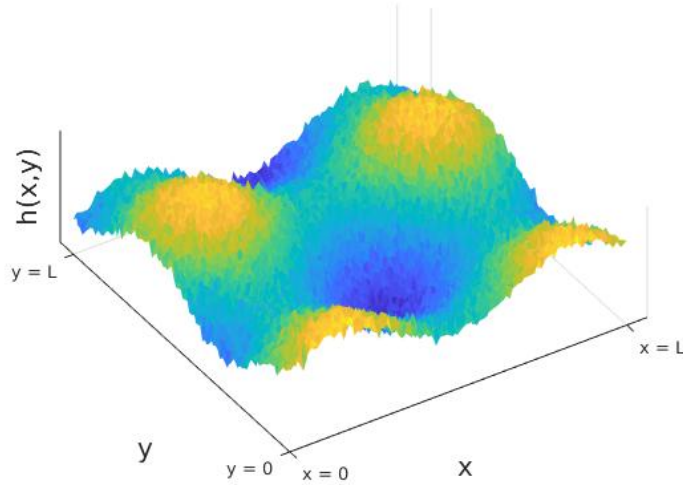
Figure 1.1: Graphical representation of a random surface $h(x, y, t)$ where the spatial domain is a $[0, L] \times [0, L]$ substrate.

tems at very small scales, where the physical interactions between the fluid and the substrate and the fluctuations due to thermal effects, both of them being negligible at larger scales, become relevant and will play a conspicuous role in the different self-organization processes assessed.

In this Chapter, the main tools used for the characterization of the level or order and disorder of thin fluid film surfaces are presented. A detailed study of the magnitude, scaling behavior in space and time, and correlations of the fluctuations will be necessary in the full assessment of disordered systems, which we will classify into different *universality classes*. On the other hand, the behavior of the surface field in Fourier space will characterize the level of order achieved in the formation of patterns. Finally, a general view of the different self-organization processes that we will study in the different chapters of the thesis will be also presented.

1.1   Basic surface characterization

Henceforth $\langle \cdot \rangle$ will denote an average either over initial conditions (for deterministic processes) or over noise realizations (for stochastic processes). The main observables which are going to be used in the characterization of surface morphologies from fluid

films, $h(x, y)$ as depicted in Fig. 1.1 in this thesis are [8]:

- The surface roughness: the standard deviation of the height values of a fluctuating surface will be used as a basic measure of the level of disorder,

$$W(L, t) = \left\langle \sqrt{\frac{1}{L^d} \int_\Omega (h(\vec{x}, t) - \bar{h}(t))^2 d\vec{x}} \right\rangle, \tag{1.1}$$

where $\bar{h}$ is the mean value of h in the d-dimensional domain $\Omega = [0, L]^d$ with lateral size L. In the example of Fig. 1.1, $d = 2$. For discrete systems, it takes the form

$$W(L, t) = \left\langle \sqrt{\frac{1}{N^d} \sum_{i=1}^{N} (h(x_i, t) - \bar{h}(t))^2} \right\rangle, \tag{1.2}$$

where $N = L/\delta x$, with δx being the lattice spacing.

- The height structure factor, also known as Power Spectral Density (PSD), allows one to measure the level of (dis)order of the system by determining the dominant spatial scales in the Fourier decomposition of the topography. It is defined as

$$S(\vec{k}, t) = \langle \hat{h}(\vec{k}, t) \hat{h}(-\vec{k}, t) \rangle = \langle |\hat{h}(\vec{k}, t)|^2 \rangle, \tag{1.3}$$

where $\hat{h}(\vec{k}, t)$ is the Foufier transform of $h(\vec{x}, t)$, defined as

$$\hat{h}(\vec{k}, t) = \int_{\mathbb{R}^n} h(\vec{x}, t) e^{i\vec{k} \cdot \vec{x}} dx_1 ... dx_n. \tag{1.4}$$

For finite systems, $S(\vec{k}, t)$ is analytically related to the roughness as [9]

$$W^2(L, t) = \frac{1}{L^d} \sum_{\vec{k} \neq 0} S(\vec{k}, t). \tag{1.5}$$

- The height-height correlation function is an alternative characterization of the field correlations in real space,

$$G(\vec{l}, t) = \langle \overline{[h(\vec{x} + \vec{l}, t) - h(\vec{x}, t)]^2} \rangle. \tag{1.6}$$

It is analytically related to the structure factor as [8]

$$G(\vec{l}, t) = \frac{1}{L^d} \sum_{\vec{k}} S(\vec{k}, t)[1 - \cos(\vec{k} \cdot \vec{l})]. \tag{1.7}$$
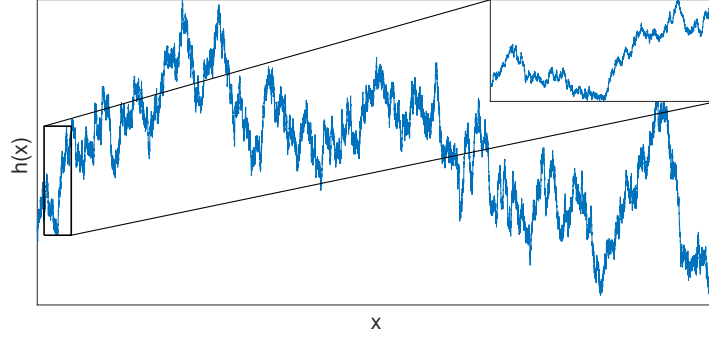
Figure 1.2: Random walk process seen for two different window sizes. The statistical indistinguishability of the surface shape in both cases illustrates the scale invariance.

1.2   Disordered surfaces: Kinetic roughening

In this section we discuss the limit case in which the formation of totally disordered surface morphologies occurs. In such a case, the hydrodynamic (large-scale) behavior of the surface is free from spatial and temporal typical scales (scale invariance). A visual example of a surface in which there is such scale invariance is depicted in Figure 1.2, where a morphology corresponding to a random walk is plotted. We can appreciate how the different scales are not distinguishable, i.e. there is no characteristic length. The concept of scale invariance emerges from the theory of phase transitions in statistical physics. The lack of a characteristic length scale at the critical temperature T_c in the Ising model, where the local imanation behaves as h described here, implies that one cannot find a typical size for the spin clusters [10].

Kinetic roughening [8, 11] is that form of surface growth in which the surface roughness envolves in the absence of spatial and temporal scales. In kinetic roughening processes, the surface roughness increases with time up to a saturation value, limited by the system size, according to the following laws:

- The surface roughness grows as a power of time with the growth exponent β,

$$W \sim t^{\beta}, \qquad W < W_{sat}. \tag{1.8}$$

- For finite systems, the surface roughness saturates to a value W_{sat} which grows as a power of system lateral size L, characterized by the roughness exponent α,

$$W_{sat} \sim L^{\alpha}. \tag{1.9}$$
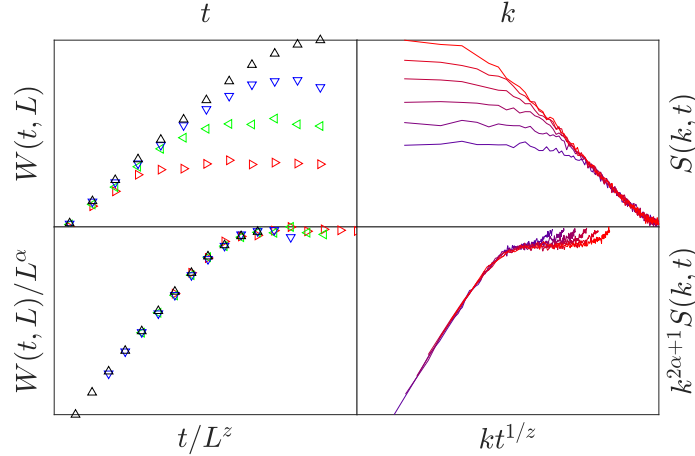
Figure 1.3: Time evolution of the field roughness (left column) and the structure factor (right column) in a kinetic roughening process (Edwards-Wilkinson equation (1.28), integrated by means of the pseudospectral method described in Chapter 3). Both raw data (top row) and collapsed data (bottom row) are shown for each case, using $\alpha = 1/2$ and $z = 2$ as scaling exponents.

The roughness exponent is related to the fractal dimension D_f of the surface as $\alpha = d + 1 - D_f$ [12]. From this point of view, the interface is a self-affine fractal (i.e. the whole interface has the same shape as one of its parts, as illustrated in Fig. 1.2).

- The time needed to achieve saturation increases as a power of the system lateral size L, characterized by the kinetic exponent z:

$$t_{sat} \sim L^z. \tag{1.10}$$

As the saturation will be reached at a time related with the saturation roughness W_{sat},

$$W_{sat} \sim L^\alpha, \qquad W_{sat} \sim t_{sat}^\beta \sim (L^z)^\beta, \tag{1.11}$$

then $\alpha = \beta z$ holds for any kinetic roughening process [8]. As a consequence, at most two of the three scaling exponents are independent. Additionally, scaling relations can hold for certain cases and will be described in detail in Chapter 3.

It is possible to define a scaling function f_W that summarizes the laws (1.8)-(1.10)

into the single expression

$$W(L,t) \sim L^\alpha f_W\left(\frac{t}{L^z}\right),$$ (1.12)

namely,

$$f_W(u) \sim \begin{cases} u^\beta & \text{if } u \ll 1, \\ \text{Constant} & \text{if } u \gg 1 \end{cases}.$$ (1.13)

This type of scaling behavior is called Family-Vicsek [8]. The evolution of the surface roughness according to this scaling behavior is shown in Figure 1.3 for a kinetic roughening process (Edwards Wilkinson equation (1.28) below). In Fourier space, the behavior of the structure factor is

$$S(k,t) \sim \begin{cases} t^{(2\alpha+d)/z} & \text{if } k^{-1} \ll t^{1/z} \\ k^{-(2\alpha+d)} & \text{if } k^{-1} \gg t^{1/z}. \end{cases}$$ (1.14)

There is also a scaling function f_s for the evolution of the structure factor in kinetic roughening processes, i.e.

$$S(k,t) \sim \frac{f_S(|k|^z t)}{|k|^{2\alpha+d}},$$ (1.15)

with the following behavior [11]

$$f_S(u) \sim \begin{cases} u^{(2\alpha+d)/z} & \text{if } u \ll 1 \\ \text{Cnst.} & \text{if } u \gg 1. \end{cases}$$ (1.16)

An example of this behavior is also shown in Figure 1.3, where both the roughness and the structure factor are depicted for several times and collapsed onto the f_W and g_S functions from Equations (1.12) and (1.15).

We can find examples of kinetic roughening behavior in the evolution of the surfaces of many experimental thin films. In Figure 1.4 we show a surface map in which kinetic roughening occurs in a thin silica film displaying frozen capillary waves. In this case the kinetic roughening behavior correspond to the same scaling as exhibited by the linear Edwards-Wilkinson model Eq. (1.28) for a two-dimensional substrate [13]. In the next section we show how the scaling exponents can be analytically determined for simple linear models like this one.

1.2.1   Anomalous scaling

There are different scenarios in which kinetic roughening occurs beyond that of Family-Vicksek, which are termed anomaluos scaling and are described below. Specifically, we consider the possibility that the roughness exponent α_s measured in Fourier
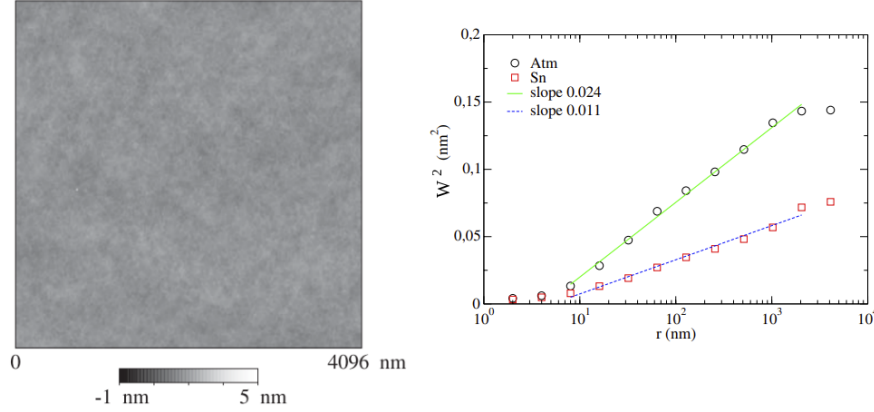
Figure 1.4: Atomic Force Microscopy (AFM) top view of an annealed silica surface morphology acquired in open air (left). The roughness scaling with the window size $G^2 \sim r^{2\alpha}$ (named W^2 in the plot) is also depicted for two different types of AFM contact modes (right), where the small values for the slopes fit well $\alpha_{EW} = 0$, i.e. $G \sim \log r$. Adapted from [13].

space from $S(k,t) \sim k^{-(2\alpha_s+d)}$ differs from the exponent α for which the roughness W diverges with the total size of the system (*intrinsic anomalous scaling*) and that in which α_s differs from the roughness exponent α_{loc} measured in real space from $G(l,t)$ (*super-roughness*). Additionally, a scenario for some facetted surfaces occurs when both intrinsic anomalous scaling and super-roughness take place at the same time.

Intrinsic anomalous scaling

In this case, the local scaling ($\alpha_s = \alpha_{loc} < 1$) differs from the global scaling (α). The structure factor scales in an anomalous way as [14]

$$S(k,t) \sim |k|^{-(2\alpha+d)} f_{S'}(|k|^z t), \qquad (1.17)$$

where $f_{S'}$ behaves as

$$f_{S'}(u) \sim \begin{cases} u^{2\alpha+d} & \text{if} \quad u \ll 1 \\ u^{2(\alpha-\alpha_s)} & \text{if} \quad u \gg 1, \end{cases} \qquad (1.18)$$

7

Super-roughness

In cases for which $\alpha_s > 1$, a distinction between α_s and the *local* roughness exponent α_{loc}, which governs the local behavior of the height-height correlation function in real space, becomes necessary. This happens as the local exponent is bounded $\alpha_{loc} \leq 1$ [14], hence $\alpha_{loc} = 1$ when $\alpha_s > 1$. In this case it is only the height-height correlation function which scales in an anomalous way, as [14]

$$G(l,t) = t^\beta f_A \left(\frac{l}{\xi^z} \right), \tag{1.19}$$

where $\xi \sim t^{1/z}$ is the correlation length. The scaling function f_A scales as

$$f_A(u) \sim \begin{cases} u^{2\alpha_{loc}} = u^2 & \text{if} \quad u \ll 1 \\ \text{Cnst.} & \text{if} \quad u \gg 1, \end{cases} \tag{1.20}$$

For instance, the linear LMBE equation described in the next subsection exhibits super-rough behavior for $d = 1$, as $\alpha_{LMBE} = 3/2 > 1$ governs the local behavior in Fourier space, see Eq. (1.2.4).

Facetted systems

Both effects ($\alpha_s \neq \alpha_{loc}$ due to $\alpha_s > 1$ as in super-roughness and $\alpha \neq \alpha_s$ as in intrinsic anomalous scaling) do occur in this type of scaling. The behavior of the structure factor for a system belonging to this class of kinetic roughening is shown in Fig. 1.5, in which the behavior of $S(k,t)$ is depicted for the so-called Sneppen model A of self-organized depinning. Data collapse is achieved using Eq. 1.17.

1.2.2   Anisotropic scaling in two-dimensional surfaces

In kinetic roughening processes for two-dimensional surfaces, the scaling behavior can be *anisotropic* when there is no $x \leftrightarrow y$ symmetry, hence different exponent values are exhibited along the x and y substrate directions. While the growth exponent β must be the same in both directions [15], different values for α and z can be observed in the x and y directions, hence the relation

$$\beta = \frac{\alpha_x}{z_x} = \frac{\alpha_y}{z_y} \tag{1.21}$$

holds. The α_x and α_y exponents can be obtained from different observables as the structure factor S_x and S_y defined as

$$S(k_x, 0, t \gg 1) \sim k_x^{-(2\alpha_x + 1 + \zeta)}, \qquad S(0, k_y, t \gg 1) \sim k_y^{-(2\alpha_y + 1 + 1/\zeta)}, \tag{1.22}$$
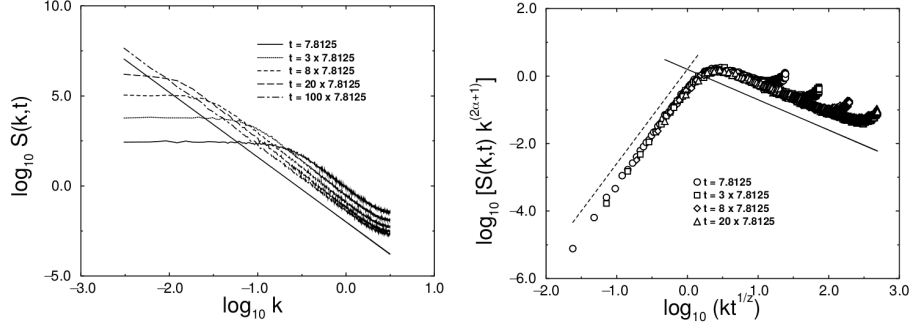
Figure 1.5: *Bare (left) and collapsed (right) structure factor $S(k,t)$ for an interface dep-pining process [14]. Notice the presence of the two different slopes in the collapsed data ($2\alpha + d$ and $2(\alpha - \alpha_s)$) and the systemic vertical displacement of $S(k,t)$ for large values of k which did not occur in the Family-Vicsek scaling (see e.g. Fig. 1.3). Here $\alpha = z = 1$, $\alpha_s = 1.35$, hence $\alpha_{loc} = 1$.*

where $\zeta = \alpha_x/\alpha_y$, and the local roughness (height-height correlation) functions

$$G_x(l,t) = \langle \overline{[h(x + l, y, t) - h(x, y, t)]^2} \rangle \sim l^{2\alpha_x}, \tag{1.23}$$

$$G_y(l,t) = \langle \overline{[h(x, y + l, t) - h(x, y, t)]^2} \rangle \sim l^{2\alpha_y}. \tag{1.24}$$

An example of this behavior will be assessed in Chapter 4 in the study of the universality class of the Burgers equation in higher spatial dimension (e.g. for the anisotropic Hwa-Kardar equation).

1.2.3   Multiscaling

Another aspect of some kinetic roughening processes is that higher moments of the height-height correlation function, namely

$$G_q(x,t) = \langle [h(x + l, t) - h(x, t)]^q \rangle^{1/q} \tag{1.25}$$

for different values of q, may not scale with the same roughness exponent α. In that cases, the morphologies are said to exhibit multi-affinity [8]. This definition generalizes Eq. 1.6 so that $G(x,t) = G_2^2(x,t)$. An illustrative example of multi-affine surface is shown in Fig. 1.6, where the correlation function $G_q(x)$ is seen to scale as x^{α_q}, where α_q take different values for different values of q.
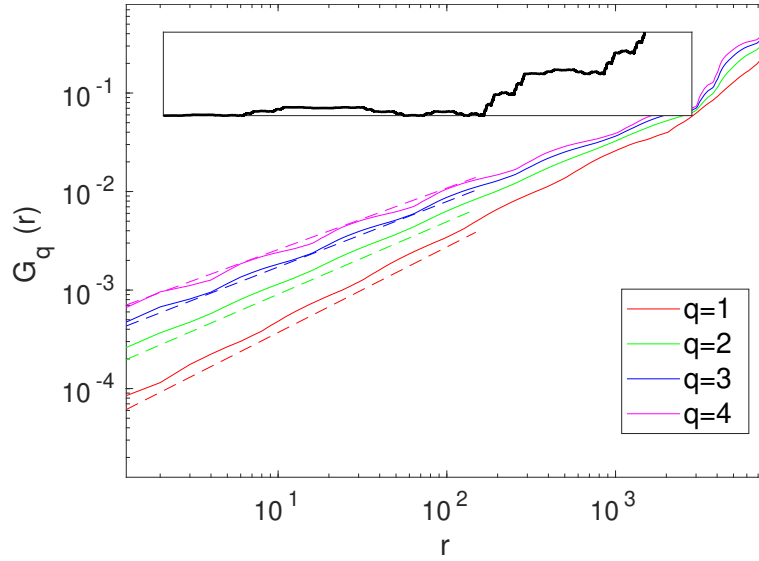
Figure 1.6: Multiscaling behavior of a deterministic multi-affine profile (inset) generated as a deterministic fractal from a seed $[0, b, 0, 0.5, 1]$ which is rescaled for each subinterval on each iteration (here 8 iterations have been computed using $b = 0.1$), see [8]. Dashed straight lines are guides to the eye that represent the exact value of the slope $\alpha_q = \frac{\log((b^q + 0.5^q)/2)}{q \log(1/4)}$.

1.2.4   Linear models

In this section, we illustrate the kinetic roughening behavior of some linear models that will play an important role throughout this thesis. For these models [11, 8], exact analytical results can be easily obtained. The most simple model,

$$\partial_t h = \eta(x, t), \tag{1.26}$$

describes a random deposition process (e.g. random deposition of atoms). Here, η is a white noise term with correlations as

$$\langle \eta(\vec{x}, t) \rangle = 0, \qquad \langle \eta(\vec{x}_1, t_1)\eta(\vec{x}_2, t_2) \rangle = 2D\delta^d(\vec{x}_1 - \vec{x}_2)\delta(t_1 - t_2), \tag{1.27}$$

For a surface described by Eq. 1.26, the roughness increases as $W \sim t^{1/2}$, hence $\beta = 1/2$. Moreover, the height values are uncorrelated and the surface does not achieve a saturation value, hence the exponents α and z are not well-defined in this case.

Beyond this simple model, we have also some conspicuous models as the Edwards-Wilkinson (EW) equation,

$$\partial_t h = \nabla^2 h + \eta(x, t), \tag{1.28}$$

the Linear Molecular Beam Epitaxy (LMBE) equation,

$$\partial_t h = -\nabla^4 h + \eta(\vec{x}, t), \tag{1.29}$$

and, in general, stochastic equations of the form,

$$\partial_t h = -(-\nabla^2)^{z/2} h + \eta(\vec{x}, t). \tag{1.30}$$

The scaling exponents can be determined analytically for any dimension of the substrate. In Fourier space Eq. (1.30) becomes

$$\partial_t \hat{h}(\vec{k}, t) = -|\vec{k}|^z \hat{h}(\vec{k}, t) + \eta(\vec{k}, t), \tag{1.31}$$

which is also well defined for arbitrary values of z. When z takes either odd or fractional values, Eq. (1.31) becomes *nonlocal* in space, involving e.g. Hilbert transforms for odd values of z. One example can be found in the case of $z = 1$, which has been employed in the modeling of diffusion-limited erosion (DLE) [16, 11],

$$\partial_t h = -\partial_x \mathcal{H}[h] + \eta, \tag{1.32}$$

where $\mathcal{H}[\cdot]$ is the so-called Hilbert transformed, defined as

$$\mathcal{H}[f](x) = \frac{1}{\pi} \int_{-\infty}^{\infty} \frac{f(s)}{x-s} ds, \tag{1.33}$$

whose Fourier transform is

$$\mathcal{H}[f](k) = -i \cdot \mathrm{sgn}(k) f(k). \tag{1.34}$$

Equation (1.31) can be expressed in variational form as

$$\partial_t \hat{h}(\vec{k}, t) = -\frac{\delta H}{\delta \hat{h}} + \eta(\vec{k}, t), \qquad H = -\sum_k |k|^z \hat{h}(\vec{k}, t) \hat{h}(-\vec{k}, t). \tag{1.35}$$

If we rescale space and time coordinates by an arbitrary factor $b > 1$,

$$\tilde{x} = bx, \qquad \tilde{t} = b^z t, \qquad \tilde{h} = b^{-\alpha} h(\tilde{x}, \tilde{t}), \tag{1.36}$$

using that $\delta^d(b\vec{x}) = b^{-d}\delta^d(\vec{x})$, the EW ($z = 2$) and LMBE ($z = 4$) equations become, dropping the primes,

$$\partial_t h = -b^{z-2}(-\nabla^2)^{z/2}h + b^{-d/2+z/2-\alpha}\eta, \tag{1.37}$$

and

$$\partial_t h = -b^{z-4}(-\nabla^2)^{z/2}h + b^{-d/2+z/2-\alpha}\eta, \tag{1.38}$$

respectively, with ∇^2 being the Laplacian operator. Exploiting the idea of scale invariance, we request that the rescaled equation of motion remains invariant under the transformation (1.36), which leads to the values of the critical exponents,

$$z_{EW} = 2, \qquad 2\alpha_{EW} + d = z_{EW} \Rightarrow \alpha_{EW} = \frac{2-d}{2}, \tag{1.39}$$

for the EW equation and

$$z_{LMBE} = 4, \qquad \alpha_{LMBE} = \frac{4-d}{2}, \tag{1.40}$$

for the LMBE equation.

The evolution of the structure factor in both cases (and in general, for any value of z) can be obtained analytically as

$$S(\vec{k}, t) = \langle \hat{h}(\vec{k}, t)\hat{h}(-\vec{k}, t) \rangle =$$
$$= \int_0^t \int_0^t e^{-|\vec{k}|^z(t-s_1)} e^{-|\vec{k}|^z(t-s_2)} \langle \eta(\vec{k}, s)\eta(-\vec{k}, s) \rangle ds_1 ds_2 = D\frac{1 - e^{-2|k|^z t}}{|\vec{k}|^z}, \tag{1.41}$$

with the $z = 2$ case being depicted as an example in the top left panel of Fig. 1.3 from numerical simulations.

1.2.5   Nonlinear models

Kardar-Parisi-Zhang equation

The Kardar-Parisi-Zhang (KPZ) equation, which describes the space-time evolution of a scalar field h as

$$\partial_t h = \nu\nabla^2 h + \frac{\lambda}{2}(\nabla h)^2 + \eta, \tag{1.42}$$

where $\nu, D > 0$ and λ are parameters and η is *non-conserved*, zero-mean, uncorrelated Gaussian noise, is a conspicuous example of a nonlinear kinetic roughening system as well as a paradigmatic representative of a universality class. It has been proposed [17] for the modeling of many non-equilibrium phenomena —randomly stirred fluids, polymer dynamics in disordered media, and surface growth— and has been recently found to describe the universal behavior of a surprisingly wide range of systems [18], like bacterial range expansion [19], diffusion-limited growth [20], turbulent liquid crystals [21], classical non-linear oscillators [22], stochastic hydrodynamics [23], reaction-limited growth [24], random geometry [25], superfluid exciton polaritons [26], or incompressible polar active fluids [27].

Nonlinear MBE equation

Another conspicuous example of nonlinear equation with kinetic roughening behavior is a conserved-dynamics generalization of the KPZ equation,

$$\partial_t h = -\nabla^2 \left[\nu\nabla^2 h + \frac{\lambda}{2}(\nabla h)^2 \right] + \eta. \tag{1.43}$$

This equation is known as the nonlinear molecular-beam epitaxy (NMBE) equation as it has been found to describe the kinetic roughening behavior in the growth of epitaxial thin films [28].

1.2.6   Universality classes in kinetic roughening

Different systems in which kinetic roughening occurs with the same scaling exponent values for the various dimension have been traditionally considered to be in the same universality class. More recently, not only the scaling exponents but also the statistical distribution of the surface fluctuations are being considered for the characterization of universality classes. For instance, the Gaussian distribution holds for any linear model like the EW and the LMBE equations (see Table 1.1), as the Hamiltonian (see Eq. (1.35)) H is quadratic in h and the probability density function

of the fluctuations behaves as $P(h) \propto e^{-H[h]}$ [29]. However, this is not in general the case for nonlinear models. Some relevant universality classes, as well as their representative equations for 1-D spatially extended systems, the value of the scaling exponents, and the fluctuation statistics probability distribution function (PDF) are presented in Table 1.1.

Class	Reference equation	α	β	z	α_{loc}	α_s	Fluctuations
EW	$\partial_t h = \nu \partial_x^2 h + \eta$	1/2	1/4	2	1/2	1/2	Gaussian
LMBE	$\partial_t h = -\kappa \partial_x^4 h + \eta$	3/2	3/8	4	1	1	Gaussian
KPZ	$\partial_t h = \nu \partial_x^2 h + \frac{\lambda}{2}(\partial_x h)^2 + \eta$	1/2	1/3	3/2	1/2	1/2	Tracy-Widom
NMBE	$\partial_t h = -\nu \partial_x^4 h + \frac{\lambda}{2}\partial_x^2(\partial_x h)^2 + \eta$	1.0	0.3	3.0	1.0	1.0	Non-symmetric

Table 1.1: *Characterization in terms of scaling exponents and fluctuation statistics of some of the main universality classes for kinetic roughening processes in 1D substrates [8, 11, 29, 30]. Notice that the exponent values for the NLMBE equation are not exact.*

KPZ universality class

In spite of its nonlinear behavior, the scaling exponents of the KPZ equation are known analytically for $d = 1$ [18]. For a periodic KPZ system, the fluctuations within the nonlinear growth regime follow distributions of the celebrated Tracy-Widom (TW) family [31, 32, 18, 33, 34], which reflect the lack of up-down symmetry of the equation under $h \leftrightarrow -h$, see the non symmetric TW PDF in Figure 1.7 and notice how the TW-distributed morphologies are not symmetric while Gaussian-distributed ones are.

Beyond the one point statistics, the covariance function

$$C(x,t) = \langle h(x_0,t)h(x_0+x,t)\rangle - \langle \bar{h}(t)\rangle^2, \qquad (1.44)$$

is also known to display universal behavior scaling as $C \sim t^{2\beta}A(x/t^z)$, with $A(y) \sim$ cst. $- y^{2\alpha}$ for $y \ll 1$ and 0 for $y \gg 1$ (see Fig. 1.8). The scaling function $A(s)$ is the covariance of the so-called Airy$_1$ process [35, 18, 33].

The scaling exponents and the fluctuation statistics have been also numerically determined for two-dimensional substrates. For higher dimensions, universal exponents and fluctuation PDF are expected up to the critical dimension, which still remains unknown [8].
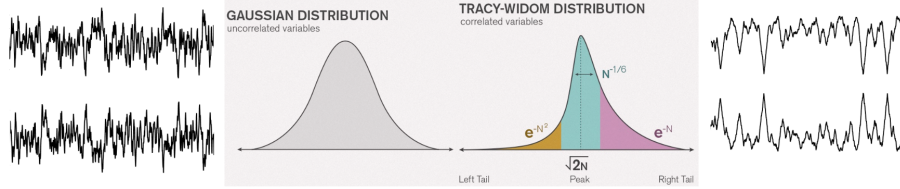
Figure 1.7: *Gaussian vs Tracy-Widom distribution PDF shapes taken from [36] (middle panel). Gaussian and TW-distributed morphologies [taken from numerical simulations of the EW (left panel) and KPZ (right panel) equations in the growth regime] and their up-down mirror reflections are also depicted on the left and right panels, respectively, in order to illustrate the presence and lack of up-down symmetry.*
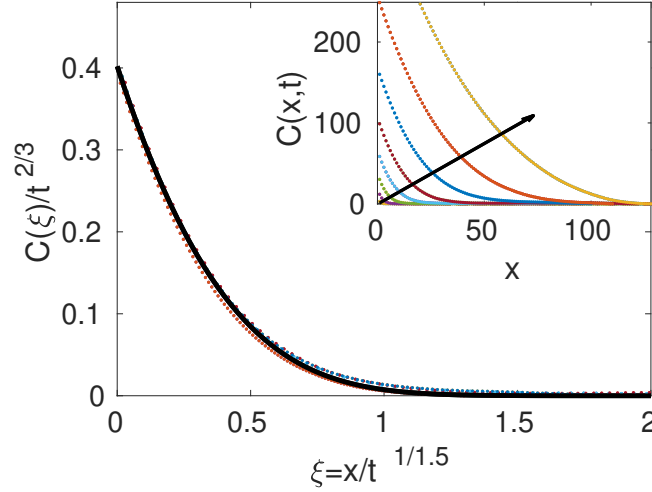
Figure 1.8: *Collapse of the two-point correlation function $C(x,t)$ at different times described by the KPZ Eq. (1.42) for $L = 256$, $\delta t = 10^{-2}$, $\nu = D = 1$, $\lambda = 10$. Inset shows the uncollapsed data. The solid line shows the exact covariance of the $Airy_1$ process [35]. Arrows show time increase, with t doubling for each line, from $t_0 = 1$.*
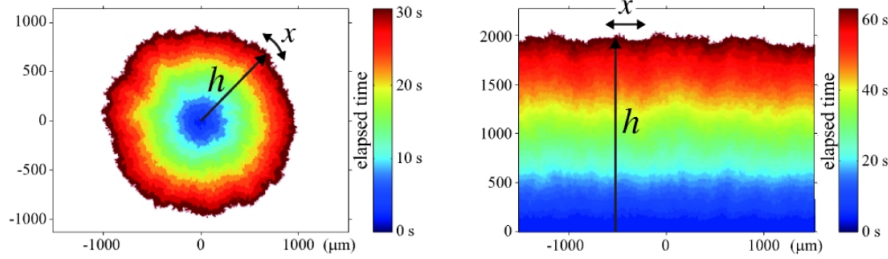
Figure 1.9: *Interfaces between the different phases of turbulent liquid crystals for experiments carried out by Takeuchi et al. [39]. The kinetic roughening behavior is in the KPZ universality class. Left and right panels show circular and flat geometrical conditions respectively, corresponding to two different subclasses of the KPZ universality class.*

Independence between scaling exponents and fluctuation statistics

We could wonder if kinetic roughening systems with the same values for the scaling exponents always display the same fluctuation statistics, or vice versa. The answer is negative both ways. Systems with the same fluctuation statistics can present different values for the scaling exponents: one trivial example can be found in linear models — which always exhibit Gaussian fluctuations — with different values of the scaling exponents, like the EW and the LMBE equations. Other nontrivial examples can also be found in the literature, e.g. the same fluctuation PDF occurs under different values of the scaling exponents in the KPZ equation and in some generalizations of the Kuramoto-Sivashinsky equation in 2D described in [37]. On the other hand, systems with the same values of the scaling exponents and different values of the fluctuation statistics can also be found; this is the case of the KPZ equation and a linear approximation (*proxy*) based on the linear model proposed in [38],

$$\partial_t \hat{h} = -|k|^{3/2}\hat{h} + \eta, \qquad \langle \eta(k,t)\eta(k',t') \rangle \propto \delta_{k+k'}|t - t'|^{2/3}, \qquad (1.45)$$

which exhibits the same scaling exponents as the 1D KPZ equation but different fluctuation PDF (which is Gaussian, as Eq. (1.45) is linear).

Universality subclasses

Different geometries for the spatial domain can result into different fluctuation behavior for the same system. This occurs in the KPZ case, where fluctuations in the nonlinear growth regime follow different distributions within the TW family, while

16
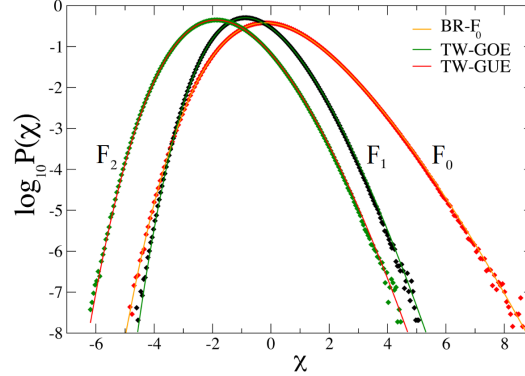
Figure 1.10: Tracy-Widom (GOE and GUE) as well as Baik-Reins F_0 distribution PDFs (solid lines) compared with numerical values from simulations of the KPZ equation, taken from [18].

the scaling exponents are the same for different domain geometries. Not-enlarging and enlarging spatial domains (e.g. in flat and circular geometries, respectively, see Figure 1.9) result into TW-GOE and TW-GUE distributions (see Fig. 1.10), which are the distributions for the largest eigenvalue of random matrices in the Gaussian Orthogonal Ensemble (GOE) and the Gaussian Unitary Ensemble (GUE), respectively. These systems with different fluctuation PDF but same scaling exponents can be considered as members of different *universality subclasses* [21, 18].

Fluctuations after saturation to steady state

In the case of the KPZ equation in 1D spatial domains, we can define different fluctuation fields as

$$X(x, \Delta t, t_0) = \frac{\Delta h - \overline{\Delta h}}{(\Gamma \Delta t)^\beta}, \tag{1.46}$$

where $\Delta h(x, \Delta t, t_0) = h(x, t_0 + \Delta t) - h(x, t_0)$, bar denotes space average, β is the growth scaling exponent, Γ is a normalization constant [32], and $\Delta t \gg 1$. In this way, we can distinguish the fluctuation behavior in different time regimes. This distinction in KPZ leads to different statistical distributions of $X(x, \Delta t, t_0)$ before $(t_0 = 0, \Delta t \ll t_{sat})$ and after $(t_0 > t_{sat})$ saturation. While they are characterized by the TW-GOE PDF before saturation, they follow the Baik-Reins (BR) PDF after saturation [31, 32, 18, 33] (see Fig. 1.10). It is unclear if this special behavior after saturation does also occur in other systems. The *bare* fluctuations at steady
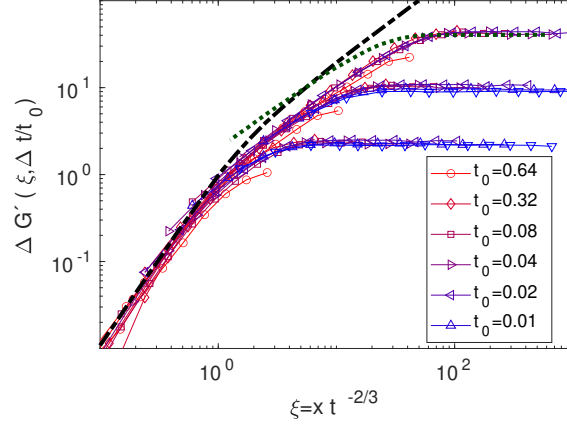
Figure 1.11: Two-point correlation function $\Delta G' = G'(\xi, \Delta t, t_0) - G'(0, \Delta t, t_0)$ from numerical simulations of KPZ Eq. (1.42) for $L = 2^{10}$, $\delta t = 5 \cdot 10^{-3}$, $\delta x = 1$, $\nu = D = 1$, $\lambda = 6$. Different sets of data, increasing from top to bottom, correspond to different values of $\Delta t/t_0$ (0.001, 0.008, and 0.06). The black dash-dotted line is the stationary KPZ correlation $g(\xi) - g(0)$, and the green dotted line is the Airy$_1$ correlation, as in [32]. Color evolves from blue to red for increasing t_0. The number of realizations is 10^2.

state (for $t > t_{sat}$, $\Delta t = 0$) happen to be Gaussian in this case as a result of the fluctuation-dissipation relation by which the nonlinear term does not influence the corresponding stationary solution of the Fokker-Planck equation governing the field PDF, which becomes a Gaussian, equilibrium-like distribution, determined by the linear and the noise terms [40, 11].

Not only the correlations of the fluctuations at steady state but also the two-time two-point correlations for h after saturation exhibit a characteristic behavior in the KPZ equation. The correlations defined as

$$\mathcal{G}(l, \Delta t, t_0) = \langle (\delta h(x + l, t_0 + \Delta t) - \delta h(x, t_0))^2 \rangle, \qquad \delta h = h - \langle h \rangle \qquad (1.47)$$

behave, for large t_0 and Δt, as

$$\mathcal{G}'(\xi, \Delta t, t_0) \equiv t^{-1/z} \mathcal{G}(\xi, \Delta t, t_0) \simeq g(\xi), \qquad (1.48)$$

with $\xi = l/t^{1/z}$ and $g(\xi)$ the exact solution for the rescaled stationary KPZ correlation [41, 42, 32]. This is indeed the behavior found in Fig. 1.11. This behavior has been previously assessed in [32] both for a discrete model and for liquid crystal experiments in the 1D KPZ universality class. In Fig. 1.11 we provide the same results for direct simulations of the continuous equation.
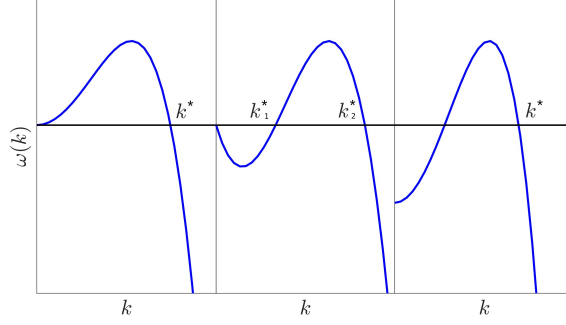
Figure 1.12: *Dispersion relation dependence on wavenumber k for type II (left panel) and type I (center and right panels) instabilities.*

The role of symmetries in the universality classes

In the case of the KPZ equation, the universal non-zero skewness of its PDF is interpreted [11] as reflecting a privileged direction for fluctuations in h (e.g., a specific growth direction for the surface of a thin film [8, 29]), as could be guessed by the lack of up-down symmetry of the KPZ equation under the transformation $h \leftrightarrow -h$ [11]. This conjecture is reinforced by the fact that the sign of the fluctuation skewness is determined by the sign of the nonlinear term, hence the KPZ profiles in the long time limit (but prior to saturation to steady state) can be expressed as

$$h(t) \simeq v_\infty t + \text{sign}(\lambda)(\Gamma t)^\beta \chi, \tag{1.49}$$

where v_∞ is a constant and χ is a TW-distributed random variable.

The NMBE equation also lacks the up-down symmetry [8, 11, 29] and similarly displays non-zero skewness fluctuations, even if its PDF does not belong to the TW family [30].

1.3   Ordered systems: pattern formation

Under suitable conditions, the surfaces of thin fluid films can present spatial patterns. Here we will see how the degree of order of these patterns can be easily described in Fourier space. If a surface profile h has some degree of spatial order with a predominant length scale λ, the structure factor will present a prominent peak at the mode with wavenumber $k = 2\pi/\lambda$. The formation of this pattern in linear partial differential equations of the form $\partial_t \hat{h} = F(k)\hat{h}$ in Fourier space, for which the solutions take

the form $\hat{h}(k,t) = \hat{h}(k,0)e^{F(k)t}$, can be described in terms of the linear dispersion relation $\omega(k)$, which equals the real part of $F(k)$. Since in this case the amplitude of the Fourier modes envolves as $S(k,t) \sim e^{2\omega(k)t}$, the functional dependence of ω with k (which usually takes a polynomial form within a large lengthscale approximation) leads to the following scenarios [43]:

1. $\omega(k) < 0 \quad \forall k$: stable flat solution. The amplitude of all Fourier modes of the solution will decrease with time, leading to a flat surface at $t \to \infty$.

2. $\omega(k) > 0 \quad \forall k < k^*$ and $\omega(k) < 0 \quad \forall k > k^*$ (see the left panel in Figure 1.12): disordered pattern formation (type-II instability [44]). The growth of Fourier modes $h(k)$, $k \in [0, k^*]$ leads to the growth of large wavelength perturbations $\lambda \in [2\pi/k^*, \infty)$, resulting into the formation of disordered patterns for sufficiently large systems.

3. $\omega(k) > 0 \quad \forall k \in [k_1^*, k_2^*]$ and $\omega(k) < 0 \quad k \notin [k_1^*, k_2^*]$ (see the center and right panels in Figure 1.12): ordered pattern formation (type I instability in [44]). The growth of a narrow band of Fourier modes is equivalent to the growth of a narrow band of wavelengths $\lambda \in [2\pi/k_1^*, 2\pi/k_2^*]$, leading to an ordered pattern (the narrower the band, the more ordered the pattern).

This behavior is analogous to Landau's theory of phase transitions, with type I and type II instabilities being analogous to first and second order phase transitions, respectively [45].

As a paradigmatic example, both of type I and type II instabilities, can be found in the stationary solutions of the damped Kuramoto-Sivashinsky (KS) equation

$$\partial_t h = -\delta h - \nabla^2 h - \nabla^4 h + (\partial_x h)^2, \tag{1.50}$$

where δ is the damping factor. Here the dispersion relation takes the form

$$\omega(k) = -\delta + k^2 - k^4, \tag{1.51}$$

hence both type (I) and type (II) instabilities can be found for $\delta = 0$ and $0 < \delta < 1/4$, respectively. A representative pattern for each case is shown in Figure 1.13, where the presence of order and disorder is easily appreciated for suitable values of δ.

Experimental examples of ordered and disordered patterns in thin fluid films can be found for instance in drop formation. In Figure 1.14 two experimental patterns of drops are depicted. Drop formation by so-called spinodal dewetting (see Chapter 2) usually leads to the formation of a disordered pattern [46], while drop formation
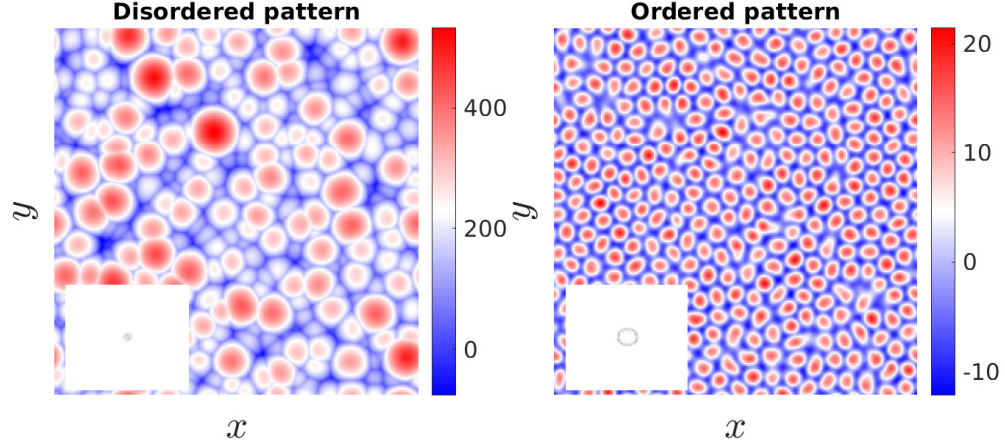
Figure 1.13: *Stationary surface morphologies for the damped Kuramoto-Sivashinsky Eq. (1.50) (top view) for $\delta = 0$ (left) and $\delta = 0.24$ (right), leading to a disordered and ordered patterns respectively. Insets represent a color map for the structure factor in each case. Simulations have been performed using the pseudospectral method described in Chapter 3, using $\delta x = 1$ with $\delta t = 2 \cdot 10^{-4}$ (left) and $\delta t = 2 \cdot 10^{-2}$ (right).*
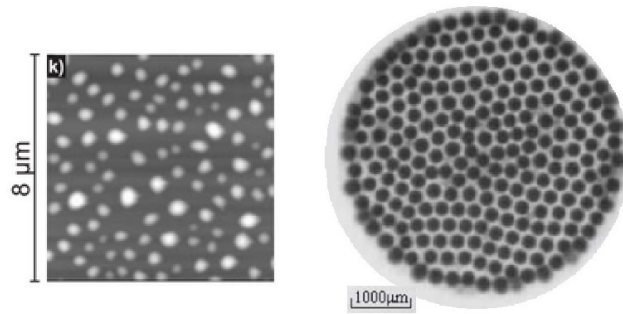
Figure 1.14: *Experimental examples (top views) of a disordered drop pattern obtained by dewetting experiments on a thin polystyrene film (left) taken from [46] and of an ordered pattern of ferrofluid drops taken from [47].*

in ferrofluids under the action of an external magnetic field is a paradigmatic case of high spatial order pattern formation at macroscopic and microscopic scales [48, 47]. In Chapters 2 and 8 these drop formation processes are described and mathematically modelled. Moreover, the conditions under which a high spatially ordered pattern of drops can be achieved in an ultrathin (nanoscale) ferrofluid film is studied in Chapter 8.

1.4   Self-organization processes in this thesis

Several aspects about surface self-organization processes described in this Chapter are going to be addressed in Chapters 4-8 in the context of thin fluid films. Our investigations will deepen into the following issues:

- The role of the equation symmetries in the fluctuation statistics is addressed in chapters 4 and 5, where Burgers equation (which does lack up-down symmetry, as the KPZ equation) is shown by numerical and analytical results to exhibit symmetric, Gaussian fluctuations induced by the combined loss of up-down and left-right $x \leftrightarrow -x$ symmetries.

- In analogy to the previous example for the KPZ universality subclasses, in Chapter 6 we provide a novel example of an universality subclass induced not by the system geometry but by the competition between stochastic and chaotic nature of the fluctuations, in a system in which both sources of noise are present. That is the case of the Kuramoto-Sivashinsky equation with *conserved* noise, which is also derived in Chapter 6 as a model for the surface evolution of an ultrathin fluid film falling down a slope subject to thermal stress. In this system, the competition of chaotic and stochastic (thermal) fluctuations can be tuned by adjusting the system temperature, hence the different universality subclasses occur at low and high temperatures (below and under a threshold temperature $T^* > 0$), respectively.

- In Chapter 7 we find *(i)* intrinsic anomalous scaling in the stochastic version of the Korteweg-de Vries equation and the inviscid limit of the KPZ equation, which had not been previously found in a continuous model with additive white noise up to our knowledge and *(ii)* a novel class of anomalous scaling that does not fit into the different classes described here in the conserved version of the Korteweg-de Vries equation and the inviscid limit of the stochastic Burgers

equation. Furthermore, we study a physical model based on an Ising-like system which reproduces the intrinsic anomalous scaling of the inviscid 1D KPZ equation, reinforcing the universal character of this scaling.

- Pattern formation in the context of dewetting in ultrathin (ferro)fluid films is addressed in Chapter 8. We will assess the level of order in the formation of stationary drop patterns under conditions for which a type-I vs type-II instability occur, depending on the type of fluid-substrate interaction.

Chapter 2

Mathematical modeling of thin fluid films

In this chapter we present the physical derivation of the different equations for which several self-organization processes (kinetic roughening behavior or pattern formation) are studied in the subsequent chapters. All of them are derivations in which different approximations are made starting from a common basic situation of a thin fluid film falling down an inclined plane, which provides a paradigmatic example of the dynamics of this fluid films [49]. The classic thin film equation for this system, both in strongly and weakly nonlinear approximations, are presented as a base scenario. Then, we make further approximations in which large scales, *ultra*thin film depths, or magnetic properties of the fluid are considered, respectively.

2.1 Thin film equation

In this section, a general model is presented of a thin fluid film falling down an inclined plane, as represented in Figure 2.1. Here partial derivatives are indicated as subindexes in order to lighten the notation. We obtain the evolution equation for the film thickness $h(x, t)$ out from conservation laws for mass and linear momentum.

Assuming fluid incompressibility, the evolution equation for the film thickness, $h(x, t)$, can be obtained from the balance of mass [4]. If we take an infinitesimal portion of fluid film of width Δx and assume constant density ρ, mass conservation implies

$$\rho(h\Delta x)_t = \rho \left(\int_0^h u(x, y) \; dy - \int_0^h u(x + \Delta x, y) \; dy \right). \tag{2.1}$$
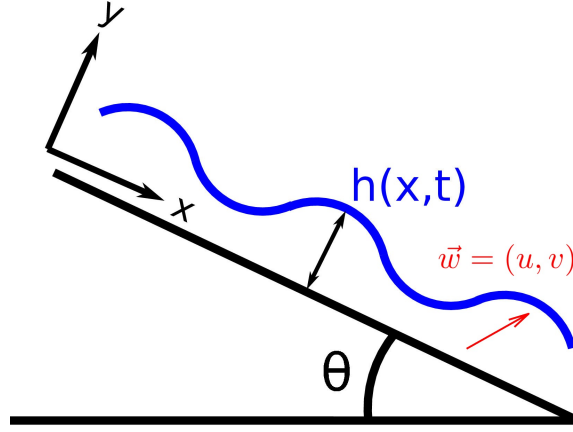
Figure 2.1: *Sketch of a thin liquid film falling down a rigid plane inclined at angle θ.*

where $u(x,t)$ is the streamwise component of the fluid velocity field along the x axis, see Fig. 2.1 for coordinate conventions. In the limit of $\Delta x \to 0$,

$$h_t + \left(\int_0^h u\,dy \right)_x = 0. \tag{2.2}$$

The full velocity field (u,v) can be obtained from the balance of linear momentum [49], namely,

$$\rho(u_t + u\,u_x + v\,u_y) = \mu(u_{xx} + u_{yy}) - p_x + \rho\,g\,\sin\theta, \tag{2.3}$$

$$\rho(v_t + u\,v_x + v\,v_y) = \mu(v_{xx} + v_{yy}) - p_y - \rho\,g\,\cos\theta, \tag{2.4}$$

where μ is the liquid viscosity (assumed constant), p denotes hydrostatic pressure, and g is the acceleration of gravity.

We consider non-slip, no-penetration boundary conditions $u = v = 0$ at the planar rigid substrate $(y = 0)$ and a simple stress balance at the free surface of the film $[y = h(x,t)]$,

$$||\vec{n}\,\mathcal{T}\,\vec{n}|| = \gamma\mathcal{C}, \qquad ||\vec{n}\,\mathcal{T}\,\vec{t}|| = 0. \tag{2.5}$$

Here, $\mathcal{C}$ is the curvature of the free surface and γ is the surface tension, assumed isotropic [49], $\vec{n}$ and $\vec{t}$ are the unit normal and tangential vectors, namely

$$\vec{n} = \frac{1}{\sqrt{1 + h_x^2}} \begin{pmatrix} -h_x \\ 1 \end{pmatrix}, \qquad \vec{t} = \frac{1}{\sqrt{1 + h_x^2}} \begin{pmatrix} 1 \\ h_x \end{pmatrix}, \tag{2.6}$$

and $\mathcal{T}$ is the stress tensor for a Newtonian fluid, which reads

$$\mathcal{T} = -p\mathbb{I} + \mu \begin{pmatrix} 2u_x & u_y + v_x \\ u_y + v_x & +2v_y \end{pmatrix} = \begin{pmatrix} -p + 2\mu u_x & \mu(u_y + v_x) \\ \mu(u_y + v_x) & -p + 2\mu v_y \end{pmatrix}, \quad (2.7)$$

where $\mathbb{I}$ is the 2×2 identity matrix. Now, we consider the average thickness, h_0, of the liquid layer as a typical length scale, $w_0 = \rho g h_0^2 / 2\mu$ as a velocity scale, w_0/h_0 as a time scale, and $\mu w_0/h_0$ as a representative scale for pressure and stress, and use all these to rewrite the previous equations in dimensionless units. The resulting momentum balance equations become

$$\text{Re}\,(u_t + u\,u_x + v\,u_y) = u_{xx} + u_{yy} - p_x + 2\sin\theta, \quad (2.8)$$
$$\text{Re}\,(v_t + u\,v_x + v\,v_y) = v_{xx} + v_{yy} - p_y - 2\cos\theta, \quad (2.9)$$

where $\text{Re} = \rho w_0 h_0 / \mu$ is the Reynolds number, which represents the ratio between inertial and viscous forces.

The stress balance at the free surface $(y = h)$ yields

$$p = \frac{h_x^2 2u_x - h_x[2(u_y + v_x)] + 2v_y}{1 + h_x^2} - \frac{\gamma}{\mu w_0}h_{xx}, \quad (2.10)$$

$$0 = -h_x^2(u_y + v_x) + h_x[2(v_y - u_x)] + u_y + v_x. \quad (2.11)$$

Now, we introduce a small parameter $\epsilon = h_0/L$ and the new variables $x' = \epsilon x$, $t' = \epsilon t$, and $v' = v/\epsilon$, adapted to a lubrication approximation [49] within which the cross-stream dimension of the film will be considered much smaller than its streamwise extent. We consider the capillary number, $\text{Ca} = \mu w_0/\gamma$, to be order ϵ^2 and define $\text{Ca}' = \text{Ca}/\epsilon^2$.

In the rescaled variables (omitting primes), the momentum balance equations and the surface boundary conditions become, respectively,

$$\text{Re}\,\epsilon(u_t + u\,u_x + v\,u_y) = \epsilon^2 u_{xx} + u_{yy} - \epsilon p_x + 2\sin\theta, \quad (2.12)$$
$$\text{Re}\,\epsilon^2(v_t + u\,v_x + v\,v_y) = \epsilon^3 v_{xx} + \epsilon v_{yy} - p_y - 2\cos\theta, \quad (2.13)$$
$$p = \frac{\epsilon^2 h_x^2(2\epsilon u_x) - \epsilon h_x[2(u_y + \epsilon^2 v_x)] + 2\epsilon v_y}{1 + \epsilon^2 h_x^2} - \epsilon^2 \frac{\gamma}{\mu w_0}h_{xx}, \quad (2.14)$$
$$0 = -\epsilon^2 h_x^2(u_y + \epsilon^2 v_x) + \epsilon^2 h_x[2(v_y - u_x)] + u_y + \epsilon^2 v_x. \quad (2.15)$$

Now we expand $u = u_0 + \epsilon u_1 + \mathcal{O}(\epsilon^2)$, $v = v_0 + \epsilon v_1 + \mathcal{O}(\epsilon^2)$, and $p = p_0 + \epsilon p_1 + \mathcal{O}(\epsilon^2)$. We need to compute the perturbative components of the velocity profile $u = u_0 + \epsilon u_1 + \mathcal{O}(\epsilon^2)$ in order to obtain the evolution equation from mass conservation.

At $\mathcal{O}(1)$, Eq. (2.12) becomes $u_{0yy} = -2\sin\theta$. As $u_{0y} = 0$ at the fluid surface $y = h$ [leading order of Eq. (2.15)] and $u_0 = 0$ at the substrate $y = 0$ (no-slip condition), we obtain

$$u_0 = 2\sin\theta\left(hy - \frac{y^2}{2}\right),\tag{2.16}$$

which is the celebrated parabolic Pouseuille velocity profile typical from laminar flows [4]. We can also compute v_0 from the non compressibility condition $u_x + v_z = 0$ at $\mathcal{O}(\epsilon)$, i.e. $u_{0x} + v_y = 0$ in rescaled variables. Here, no-slip $v_0 = 0$ at $y = 0$ provides a boundary condition leading to

$$v_0 = -\sin\theta\; y^2 h_x.\tag{2.17}$$

Considering Eq. (2.13) at $\mathcal{O}(\epsilon)$, we have $u_{1yy} = p_{0x} + \mathrm{Re}(u_{0t} + u_0\, u_{0x} + v_0\, u_{0y})$. Here we have $u_{1y} = 0$ [Eq. (2.15) at $\mathcal{O}(\epsilon)$] and $u_1 = 0$ as boundary conditions at the fluid surface and the substrate, respectively, which allow us to obtain

$$u_1 = \mathrm{Re}\sin^2\theta\; h_x\left(-\frac{4}{3}h^4 y + \frac{2}{3}h^2 y^3 - \frac{1}{6}hy^4\right) - p_{0x}\left(hy - \frac{y^2}{2}\right).\tag{2.18}$$

The p_0 contribution can be obtained from Eq. (2.13) at $\mathcal{O}(1)$, $p_{0y} = -2\cos\theta$, with $p_0 = -h_{xx}/\mathrm{Ca}'$ as a boundary condition at the fluid surface, obtaining $p_0 = 2\cos\theta\;(h - y) - h_{xx}/\mathrm{Ca}'$.

Finally, using that

$$\int_0^h u_0\; dy = \frac{2}{3}\sin\theta\; h^3,\tag{2.19}$$

and

$$\int_0^h u_1\; dy = \frac{h^3}{3}\left(\frac{8\mathrm{Re}\;\sin^2\theta}{15}h^3 h_x - 2\cos\theta\; h_x + \frac{1}{\mathrm{Ca}'}h_{xxx}\right),\tag{2.20}$$

in the mass conservation Eq. (2.2), the evolution equation reads

$$h_t + \left(\frac{2}{3}\sin\theta h^3 + \epsilon\frac{h^3}{3}\left(\frac{8\mathrm{Re}\;\sin^2\theta}{15}h^3 h_x - 2\cos\theta\; h_x + \frac{1}{\mathrm{Ca}'}h_{xxx}\right)\right)_x = 0.\tag{2.21}$$

This equation is known as Benney equation as it was derived for first time in [50], and is considered to be a classical equation in the context of thin fluid films. It is a so-called *strongly nonlinear* model as all the terms in Eq. (2.21), except the time derivative, are nonlinear. In the next section we derive a *weakly nonlinear* approximation of Eq. (2.21) for small perturbations in the surface h, in which both linear and nonlinear terms appear.

2.2   Weakly nonlinear approximations

2.2.1   The Kuramoto-Sivashinsky equation

A weakly-nonlinear expansion allows us to derive the KS equation from Eq. (2.21). Considering very small fluctuations around the flat film solution, $h = 1 + \epsilon \tilde{h}$, Eq. (2.21) becomes

$$\epsilon \tilde{h}_t + \left([1 + 3\epsilon\tilde{h} + 3\epsilon^2\tilde{h}^2 + \mathcal{O}(\epsilon^3)] \left(\frac{2}{3}\sin\theta + \frac{\epsilon}{3}P_x \right) \right)_x = 0, \qquad (2.22)$$

where

$$P_x = \epsilon \left[\frac{8\mathrm{Re}\,\sin^2\theta}{15}[1 + \mathcal{O}(\epsilon)]\tilde{h}_x - 2\cos\theta\,\tilde{h}_x + \frac{1}{\mathrm{Ca}'}\tilde{h}_{xxx} \right]. \qquad (2.23)$$

If we expand $(\tilde{h}^2)_x = 2\tilde{h}\tilde{h}_x$, and consider the change of variable $z = x - 2t$ and $\tau = \epsilon t$ (thus, $\partial_t = -3\partial_z + \epsilon\partial_\tau$ and $\partial_x = \partial_z$) Eq. (2.22) becomes

$$\tilde{h}_\tau + 4\sin\theta\tilde{h}\tilde{h}_z + \left(\frac{8\mathrm{Re}\,\sin^2\theta}{15} - \frac{2}{3}\cos\theta \right)\tilde{h}_{zz} + \frac{1}{3\mathrm{Ca}'}\tilde{h}_{zzzz} = 0. \qquad (2.24)$$

By defining $\kappa_0 = 1/(3\mathrm{Ca}')$, $\nu_0 = 8\mathrm{Re}\sin^2\theta/15 - 2\cos\theta/3$, and $\lambda_0 = 4\sin\theta$,

$$\tilde{h}_\tau + \nu_0\tilde{h}_{zz} + \kappa_0\tilde{h}_{zzzz} + \lambda_0\tilde{h}\tilde{h}_z = 0, \qquad (2.25)$$

which is a particular case of the KS equation in its conserved version (which is equivalent to Eq. (1.50) for $\delta = 0$ under the change of variable $u = \partial_x h$), after coordinates and fields are renamed as $(z, \tau, \tilde{h}) \to (x, t, u)$.

Linear stability analysis

The linear stability of Eq. (2.25) is studied by considering sinusoidal perturbations of different wavenumbers k around a flat solution, namely,

$$\tilde{h} = \tilde{h}_0 + \epsilon(k, t)e^{ikz}, \qquad \epsilon(k, t) \ll 1. \qquad (2.26)$$

The equation becomes $\epsilon_\tau - \nu_0 k^2 \epsilon + \kappa_0 k^4 \epsilon + \lambda_0\tilde{h}_0 \mathrm{i}k\epsilon = 0$ whose solution reads

$$\epsilon(k, \tau) = \epsilon(k, 0)\exp\left[(\nu_0 k^2 - \kappa_0 k^4 + \mathrm{i}\lambda_0\tilde{h}_0 k)\tau \right]. \qquad (2.27)$$

The amplitude of these small perturbations grows as $|\epsilon(k, \tau)| \sim e^{\omega(k)\tau}$, with $\omega(k) = \nu_0 k^2 - \kappa_0 k^4$ being the so-called linear dispersion relation for this equation. This function presents a broad band of unstable Fourier modes (type II instability), hence disordered patterns are expected to form on the fluid surface.

2.2.2   Thin film equations related to the KS equation

The Burgers equation

As argued by Yakhot in [51], the Kuramoto-Sivashinsky equation, Eq. (2.25), is expected to renormalize at large scales into an effective stochastic Burgers equation with conserved noise,

$$\partial_t h = \nu \partial_x^2 h + \lambda h \partial_x h + \partial_x \eta, \tag{2.28}$$

where notably $\nu > 0$, rendering asymptotically irrelevant the biharmonic term in Eq. (2.25). The stochastic Burgers equation is a paradigm for non-equilibrium physics [52, 53], appearing in many different contexts like traffic models, cosmology, or turbulence, with different meanings for the field h like vehicle density, mass density, or fluid velocity, respectively [54]. In this thesis we address the study of the stochastic Burgers equation, both with non-conserved (Chapter 4) and conserved (Chapter 5) noise, in terms of universality classes of kinetic roughening.

Burgers generalization in 2D: Hwa-Kardar equation

Moreover, the scalar Eq. (2.28) can be generalized to $d = 2$ as, e.g. [55]

$$\partial_t h = \nu_x \ \partial_x^2 h + \nu_y \ \partial_y^2 h + \lambda_x h \partial_x h + \lambda_y h \partial_y h + \eta, \tag{2.29}$$

where we have allowed for a non-conserved noise η. The particular $\lambda_y = 0$ case was originally introduced by Hwa and Kardar (HK) as a continuum model of avalanches in running sandpiles [56]. In Chapter 4 we will also consider these equations in our study of the universality class of the stochastic Burgers equation with non-conserved noise.

The Korteweg-de Vries (KdV) equation

If we take one more order in ϵ in the weakly nonlinear approximation of the Benney equation, Eq. (2.21), we obtain the *generalized* Kuramoto-Sivashinsky (gKS) equation which takes the form [57, 149]

$$\partial_t h + \partial_x^2 h + c\partial_x^3 h + \partial_x^4 h + h\partial_x h = 0. \tag{2.30}$$

Here, a dispersive term $c\partial_x^3 h$ appears. In the limit of large c, when this term becomes dominant, the equation acquires soliton-like solutions [57], as it does in the celebrated Korteweg-de Vries (KdV) equation,

$$\partial_t h + \mu\partial_x^3 h + \lambda h \partial_x h = 0. \tag{2.31}$$

This equation has been used as a paradigmatic model in the description of travelling waves [57]. In Chapter 7 we study some interesting properties of the stochastic version of this equation in terms of its kinetic roughening behavior.

2.3   Ultrathin fluid films

We are going to consider ultrathin fluid films throughout this thesis, for which the thickness is nanometric. Hence, we will assume that *(i)* the Reynolds number is extremely low (Re $\simeq$ 0), *(ii)* the fluid surface and the substrate are so close to each other that their interaction becomes relevant [58], and *(iii)* thermal fluctuations could be relevant in the dynamics [59]. These assumptions require us to take into account the disjoining pressure and stochastic thermal stress in the momentum balance equations.

2.3.1   Disjoining pressure

When the thickness h of a fluid film is very small, the interaction between the fluid surface and the substrate contributes an extra term to the hydrostatic pressure in the Navier-Stokes equations, the so-called disjoining pressure Π, which can be described in terms of an effective interface potential $\phi(h)$ [58] as

$$\Pi = -\partial_h \phi. \tag{2.32}$$

The curvature of this potential as a function of h determines the stability of the film: if it is negative, the film surface will be unstable (perturbations to a flat surface will grow with time); in case the curvature is positive, the film surface will be stable (perturbations to a flat surface will decrease with time). Depending on the physicochemical nature of both fluid and substrate, different types of effective interface potentials can be found [60], which are sketched in Figure 2.2:

1. Stable, also known as complete wetting scenario. The positive curvature of the potential makes the film unconditionally stable to perturbations (flat film).

2. Unstable. The negative curvature of the film makes it break into droplets under perturbations, as seen in Figure 2.2. As this process does not have to overcome an energy barrier in order for the film to break into drops, it is known as spinodal dewetting scenario by analogy to spinodal decomposition in e.g. ferromagnets.
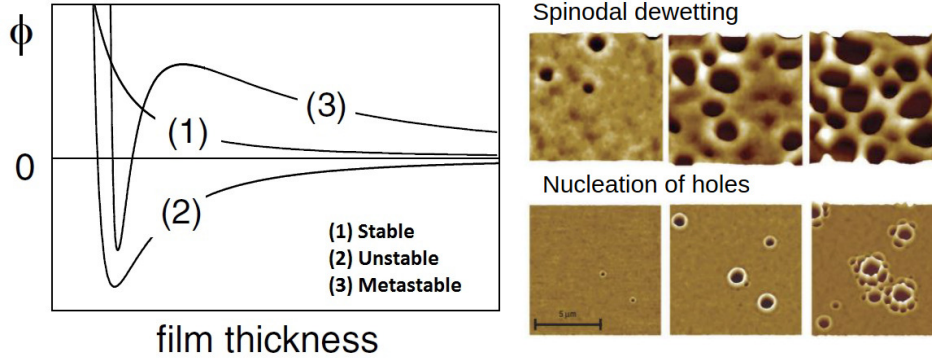
Figure 2.2: *Dependence with film thickness h of the different types of effective interface potentials, taken from [61] (left). Experimental drop formation in thin films under spinodal [(2) unstable] and nucleation [(3) metastable] scenarios for dewetting (right), taken from [62].*

3. Metastable. For large values of h, the film is stable. However, if any perturbation reduces film thickness below a value in which the sign of the potential curvature changes, the film will also break up into drops, as seen in Figure 2.2. This is known as the nucleation scenario for dewetting.

2.3.2   Stochastic thermal stress

The occurrence of relevant thermal fluctuations at very small scales makes the pressure not a deterministic function, but a fluctuating one. This effect is modelled by adding a fluctuating term S to the stress tensor $\mathcal{T}$ [59], which is symmetric, and whose entries take random values which have zero mean and an intensity which is proportional to the system temperature, namely,

$$\langle S_{i,j}(x,y,t)S_{m,n}(x',y',t')\rangle = 2\mu k_B T \delta(x-x')\delta(y-y')\delta(t-t')(\delta_{im}\delta_{jn}+\delta_{in}\delta_{jm}). \quad (2.33)$$

Here, k_B is the Boltzmann constant and T is temperature. The symmetric character of S gives rise to the $(\delta_{im}\delta_{jn} + \delta_{in}\delta_{jm})$ factor.

In the derivation of the thin film equation, some entries of the stress tensor are integrated over the vertical direction, first in the generic $[0,y]$ interval and then in the $[0,h]$ interval. This leads to the occurrence of stochastic terms in the effective

interface equation, of the form (see the derivation of the stochastic KS equation in Chapter 6 and [59])

$$\int_0^h \int_0^y S(x, y', t) \, dy'dy. \tag{2.34}$$

Due to the correlations of S, the variance of the term in Eq. (2.34) can be easily evaluated as

$$\int_0^h \int_0^h \int_0^{y_1} \int_0^{y_2} \langle S(x_1, y_1', t_1) S(x_2, y_2', t_2) \rangle \, dy_1'dy_1 dy_2'dy_2 =$$

$$= \mu k_B T \frac{h^3}{3} \delta(x_1 - x_2)\delta(t_1 - t_2). \tag{2.35}$$

Hence, the stochastic term in Eq. (2.34) can be modelled as

$$\sqrt{\mu k_B T \frac{h^3}{3}} \; \eta(x, t), \tag{2.36}$$

with η being a white noise term with zero mean and unit variance. More rigorously, this equivalence holds because the Fokker–Planck equation can be shown to be the same (i.e., the same time evolution of the height distribution) for both the thin film equation with additive noise contributions as in Eq. (2.34) or in Eq. (2.36) [59].

2.3.3   Ultrathin fluid film falling down a slope

In Chapter 6 we derive the weakly nonlinear approximation for the thin fluid film equation of a fluid falling down a slope, taking into account the three particular conditions mentioned at the beginning of this section for *ultra*thin films. Notice that, when the Reynolds number is set to zero in Eq. (2.24), the resulting linear dispersion relation,

$$\omega(k) = \left(-\frac{2}{3}\cos\theta\right) k^2 - \frac{1}{3\text{Ca}'}k^4 \tag{2.37}$$

loses all its unstable modes! However, unstable modes can be restored with the addition of an *unstable* $[\partial_h \Pi(1) > 0]$ disjoining pressure, which contributes to the dispersion relation with a positive k^2 term, in which case the linear instability of the KS equation becomes

$$\omega(k) = \left(\frac{1}{3}\partial_h \Pi(1) - \frac{2}{3}\cos\theta\right) k^2 - \frac{1}{3\text{Ca}'}k^4, \tag{2.38}$$
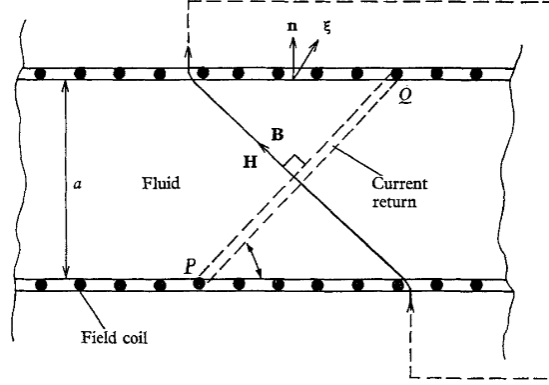
Figure 2.3: Stress over a magnetic fluid layer; scheme adapted from [48].

which now exhibits a broad band of unstable modes when $\partial_h \Pi(1) > 2\cos\theta$. In Chapter 6 a weakly nonlinear approximation of the evolution equation for an ultra-thin fluid film is derived. The thermal fluctuations induce a conserved noise term, hence the stochastic KS equation with additive *conserved* noise is obtained. To our knowledge, the KS equation with this type of noise had not been derived previously in the literature from a physical system. It exhibits an interesting transition between two different universality classes for a finite value of temperature, as also assessed in Chapter 6.

2.4   Magnetic effects in fluid films

2.4.1   Stress tensor in magnetizable fluids

Magnetic interactions also contribute to the stress tensor for magnetizable fluids, as discussed in this section. We can derive such contribution by evaluating the change in the free energy per unit volume, F, under an isothermal deformation, which is equal to the work done by the fluid due to stress. We consider a system as sketched in Fig. 2.3 in which the magnetic flux is adjusted not to change in order to avoid electrical currents, and $\vec{\xi}$ is an infinitesimal displacement in an arbitrary direction.

The change in the free energy of the film due to the magnetic field is computed as $\int_0^{|\vec{B}|} |\vec{H}| \, dB$, hence

$$F = F_0 + |\vec{H}||\vec{B}| - \int_0^{|\vec{H}|} |\vec{B}| \, dH, \qquad (2.39)$$

where F_0 is the free energy in absence of magnetic field, $\vec{H}$ is the magnetic field and $\vec{B}$ is the magnetic induction of the fluid. The mechanical work per unit area, which can be computed as the scalar product of the contraction of the stress tensor $\mathcal{T}$ over the displacement direction $\vec{\xi}$ and the normal direction $\vec{n}$, equals the variation in the free energy per unit area $\delta(Fa)$,

$$\mathcal{T}_{i,j}\xi_j n_i = \delta(Fa). \tag{2.40}$$

We use that $\frac{\delta a}{a} = \frac{\delta v}{v}$, with $v = \rho^{-1}$ being the specific volume of the fluid (notice that F does depend on v). Hence,

$$\delta(Fa) = F\delta a + a\frac{\partial F}{\partial v}\delta v = \delta a\left(F + v\frac{\partial F}{\partial v}\right) =$$

$$= \delta a\left(F_0 + v\frac{\partial F_0}{\partial v} - \int_0^{|\vec{H}|}\left(|\vec{B}| + v\frac{\partial|\vec{B}|}{\partial v}\right)\,dH + |\vec{H}||\vec{B}| + |\vec{H}|v\frac{\partial|\vec{B}|}{\partial v}\right) =$$

$$= \delta a\left(\frac{\partial(vF_0)}{\partial v} - \int_0^{|\vec{H}|}\frac{\partial(v|\vec{B}|)}{\partial v}\,dH + |\vec{H}||\vec{B}|\right) + a|\vec{H}|\delta|\vec{B}|. \tag{2.41}$$

The hydrodynamic pressure can be computed from the variation in the free energy, $p = -\frac{\partial(vF_0)}{\partial v}$, and we can also define a magnetic pressure Ω as

$$\Omega = \int_0^{|\vec{H}|}\frac{\partial(v|\vec{M}|)}{\partial v}\,dH; \tag{2.42}$$

hence, using that $|\vec{B}| = \mu_0|\vec{H}| + |\vec{M}|$,

$$\delta(Fa) = -\delta a\left(p + \Omega + \frac{1}{2}\mu_0|\vec{H}|^2 - |\vec{H}||\vec{B}|\right) + a|\vec{H}|\delta|\vec{B}|. \tag{2.43}$$

The magnetic induction strength $|\vec{B}|$ decreases proportional to the increase in the distance between the wires. As the direction of the PQ line in Fig. 2.3 is parallel to $(\vec{B}\times\vec{n})\times\vec{B}$,

$$\frac{\delta|\vec{B}|}{|\vec{B}|} = -\frac{1}{a}\left(\frac{1}{B^2}(\vec{B}\times\vec{n})\times\vec{B}\right)\cdot\vec{\xi}. \tag{2.44}$$

Using the cross product property $(\vec{A}\times\vec{B})\times\vec{C} = (\vec{A}\cdot\vec{C})\vec{B} - (\vec{B}\cdot\vec{C})\vec{A}$,

$$a\delta|\vec{B}| = \frac{(\vec{\xi}\cdot\vec{B})(\vec{B}\cdot\vec{n})}{|\vec{B}|} - |\vec{B}|(\vec{\xi}\cdot\vec{n}). \tag{2.45}$$

Finally, substituting $\delta a = \vec{\xi} \cdot \vec{n}$, we can express

$$\delta(Fa) = -\left(p + \Omega + \frac{1}{2}\mu_0|\vec{H}|^2\right)(\vec{\xi} \cdot \vec{n}) + |\vec{H}|\left(|\vec{B}|(\vec{\xi} \cdot \vec{n}) + a\delta|\vec{B}|\right) =$$

$$= -\left(p + \Omega + \frac{1}{2}\mu_0|\vec{H}|^2\right)(\vec{\xi} \cdot \vec{n}) + (\vec{\xi} \cdot \vec{B})(\vec{H} \cdot \vec{n}). \tag{2.46}$$

As the identity $\mathcal{T}_{i,j}\xi_j n_i = \delta(Fa)$ must hold for any choice of the small displacement $\vec{\xi}$, then the stress tensor $\mathcal{T}$ must take the form $\mathcal{T} = \mathcal{T}^f + \mathcal{T}^m$, where

$$\mathcal{T}^m = \begin{pmatrix} H_x B_x & H_x B_y \\ H_y B_x & H_y B_y \end{pmatrix} + \left[\frac{1}{2}\mu_0|\vec{H}|^2 - \Omega\right]\mathbb{I} \tag{2.47}$$

and $\mathcal{T}^f$ is the hydrostatic contribution. Here, we have written $\vec{B} = (B_x, B_y)$ and $\vec{H} = (H_x, H_y)$ for the magnetic field and induction components in the x, y directions. The magnetic tensor Eq. (2.47) will be considered in the derivation of the ferrofluid thin film equation in Chapter 8.

2.4.2   Thin ferrofluid film equations

The behavior of ferrofluid films under a magnetic field was studied by Cowley and Rosensweig in [48]. They modeled the so-called *normal field instability*, in which a flat ferrofluid film surface under an external magnetic field, perpendicularly oriented to the flat surface, evolves to form an ordered structure of drops. In their approximation the film is considered to be thick and Re is considered to be large. This well-ordered structure appears as a consequence of the fact that the dispersion relation of the instability takes the form [48, 5]

$$\rho\omega^2 = \rho g k - \frac{\mu_0|\vec{M}|^2}{1 + \mu_0/\mu}k^2 + \gamma k^3, \tag{2.48}$$

where μ is the effective magnetic permeability of the ferrofluid. Indeed, Eq. (2.48) presents a narrow band of unstable modes. Here the perturbations of the fluid surface are considered to be of the form $h = h_0 + \epsilon e^{i(\omega t - kx)}$, hence the imaginary values for ω are those which induce the unstable behavior.

The formation of these ordered patterns is well known to occur in experiments, both at macroscopic [63] and microscopic [47] scales (film depth $h_0 \simeq 10^{-5} - 10^{-6}$m). A dispersion relation with a narrow band of unstable modes has also been derived for a thin film in the viscous (Re$\ll$1) approximation in [64] as $\omega \sim (-k^2 + \Phi k^3 - k^4)$,
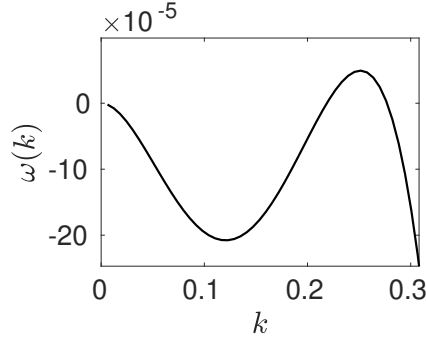
Figure 2.4: Dispersion relation Eq. (2.49) for parameter values as in the simulations in Chapter 8.

with Φ being a physical parameter proportional to the external magnetic field. In this thesis, we will address the question of what could be expected regarding the formation of these well-ordered patterns at even smaller scales (*nano*scales, i.e. film thickness $h_0 \simeq 10^{-8} - 10^{-9}$m), when the film is not just thin but *ultra*thin, so that not only are the inertial effects negligible but also the disjoining pressure must be taken into account. Different models for thin ferrofluid films under an external magnetic field H_{ext} which appear in the literature are discussed in Chapter 8. None of them presents a dispersion relation which could preserve the narrow band of unstable modes that has been demonstrated in the macroscopic model derived by Rosensweig. In contrast, we derive a strongly nonlinear effective equation for an ultrathin ferrofluid film under a magnetic field whose dispersion relation takes the form

$$\omega(k) = \frac{h_0^3}{3}\left(\partial_h\Pi(h_0)k^2 - \frac{1}{\text{Ca}''}k^4 + 2QH_{ext}\left(1 - \frac{H_{ext}}{2 + \beta\xi h_0|k|/3}\right)|k|^3\right), \quad (2.49)$$

where h_0 is the initial film height and Ca'', Q, β and ξ are constants (see Chapter 8 for the full details about the derivation of this equation). The interaction of the fluid with the magnetic field leads to the $\sim |k|^3$ contribution to the dispersion relation, while the $\sim k^2$ and $\sim k^4$ contributions are generated by the disjoining pressure and surface tension terms, respectively, allowing for the presence of a narrow band of unstable modes when the disjoining pressure potential is stable or metastable [hence, $\partial_h\Pi(h_0) < 0$] as shown e.g. in Fig. 2.4.

Chapter 3

Analytical and numerical tools

In this Chapter, we introduce the main numerical methods used in the integration of the thin film equations assessed throughout this thesis, as well as some relevant numerical tools used for numerical integration and numerical characterization of time series. Moreover, the analytical tools used in the asypmtotically approach to the scaling exponents and fluctuating statistics (cumulants) are also discussed in the context of Burgers equation, Eq. (2.28).

3.1 Numerical method for weakly nonlinear models

The stochastic weakly nonlinear models studied in this thesis have the following structure,

$$\partial_t h = \mathcal{L}[h] + \mathcal{N}[h] + \eta_1 + \partial_x \eta_2, \tag{3.1}$$

where $\mathcal{L}$ and $\mathcal{N}$ denote, respectively, a linear and a nonlinear operator, and η_1, η_2 are noise terms with zero mean and no correlations in space nor time,

$$\langle \eta_i(x,t)\eta_i(x',t') \rangle = 2D_i \delta(x-x')\delta(t-t'), \qquad i = 1,2. \tag{3.2}$$

In Fourier space for the spatial domain, Eq. (3.1) reads

$$\partial_t \hat{h} = \omega \hat{h} + \widehat{\mathcal{N}[h]} + \hat{\eta}_1 + \mathrm{i}k\hat{\eta}_2, \tag{3.3}$$

where ω is the dispersion relation induced by the linear operator $\mathcal{L}$. In this section, we discuss the different numerical methods used throughout this thesis for the integration of this type of equations (Burgers equation equation in Chapters 4 and

5, Kardar-Parisi-Zhang equation in Chapter 5, Kuramoto-Sivashinsky equation in Chapter 6, and Korteweg–De Vries equation in Chapter 7).

3.1.1   Pseudospectral methods

For equations like Eq. (3.1), pseudospectral simulation methods have demonstrated a high reliability [65, 66, 67, 68, 69, 70]. Different pseudospectral schemes can be chosen. The most simple choice is to use an explicit Euler method, i.e.

$$\hat{h}(k, t + \Delta t) = \hat{h}(k, t) + \Delta t \left(\omega(k)\hat{h}(k, t) + \widehat{\mathcal{N}[h]}(k, t) \right) + \sqrt{\frac{\Delta t}{\Delta x}} \hat{\nu}(k, t), \qquad (3.4)$$

where $\nu(x, t)$ is a random vector whose entries have zero mean and unit variance. However, both the accuracy and the stability of this method are poor and they can be improved using an integrating factor and/or considering multistep schemes for the integration in time.

Integrating factor

Here we sketch the main idea of this method [67], in which the linear part is solved exactly and just the nonlinear part is solved numerically. Multiplying both sides of Eq. (3.3) by the integrating factor $e^{-\omega t}$, we get

$$e^{-\omega t}\partial_t \hat{h} - e^{-\omega t}\omega\hat{h} = e^{-\omega t}\widehat{\mathcal{N}[h]} + e^{-\omega t}\hat{\eta}. \qquad (3.5)$$

Notice that the left hand side of Eq. (3.5) equals $\partial_t(e^{-\omega t}\hat{h})$, hence the integral of Eq. (3.5) over $[t, t + \delta t]$ becomes

$$e^{-\omega(t+\delta t)}\hat{h}(t + \delta t) - e^{-\omega t}\hat{h}(t) = \int_0^{\delta t} e^{-\omega(t+\tau)} \left(\widehat{\mathcal{N}[h]}(t + \tau) + \hat{\eta}(t + \tau) \right) \, d\tau. \qquad (3.6)$$

We isolate $\hat{h}(t + \delta t)$ as

$$\hat{h}(t + \delta t) = e^{\omega\delta t} \left[\hat{h}(t) + \int_0^{\delta t} e^{-\omega(t+\tau)} \left(\widehat{\mathcal{N}[h]}(t + \tau) + \hat{\eta}(t + \tau) \right) \, d\tau \right]. \qquad (3.7)$$

For small values of δt, we can approximate $\int_0^{\delta t} e^{-\omega\tau}\widehat{\mathcal{N}[h]}(t + \tau) \, d\tau \simeq \widehat{\mathcal{N}[h]}(t)\delta t$. The amplitude of the noise term $\hat{g}(t) = e^{\omega\delta t} \int_0^{\delta t} e^{-\omega\tau}\hat{\eta}(t + \tau) \, d\tau$ can be computed as

$$\langle \hat{g}(t)\hat{g}(t') \rangle = e^{2\omega\delta t} \int_0^{\delta t} \int_0^{\delta t} e^{-\omega(\tau+\tau')}\langle \hat{\eta}(t + \tau)\hat{\eta}(t' + \tau') \rangle \, d\tau \, d\tau'. \qquad (3.8)$$

As the intervals $[t, t + \delta t]$ and $[t', t' + \delta t]$ just overlap when $t = t'$ and the noise η is uncorrelated in time $\langle \hat{\eta}(t) \hat{\eta}(t') \rangle = 2Df(k)\delta(t - t')$, where $f(k) = 1$ for non conserved noise and $f(k) = -k^2$ for conserved noise,

$$\langle \hat{g}(t) \hat{g}(t') \rangle = 2Df(k)e^{2\omega\delta t} \int_0^{\delta t} e^{-2\omega s} \, ds = Df(k)\frac{e^{2\omega\delta t} - 1}{\omega}. \tag{3.9}$$

The integration step is finally obtained as

$$\hat{h}(t + \delta t) = e^{\omega\delta t} \left(\hat{h}(t) + \widehat{\mathcal{N}[h]}(t)\delta t \right) + \hat{g}(t), \tag{3.10}$$

with the random $\hat{g}(k, t)$ vectors being computed as

$$\hat{g}(k, t) = \sqrt{D|f(k)|\frac{e^{2\omega(k)\delta t} - 1}{\omega(k)}} \hat{\nu}(k), \tag{3.11}$$

where $\nu(x, t)$ is a random vector whose entries have zero mean and unit variance. The evaluation of the $\frac{e^{2\omega(k)\delta t} - 1}{\omega(k)}$ term is numerically unstable, as it involves the quotient between two very small numbers; instead it is computed for each value of the wavenumber k at the beginning of the simulation using a residue integral in the complex plane as

$$\frac{e^{2\omega(k)\delta t} - 1}{\omega(k)} = 2\delta t \oint_\gamma \frac{e^z - 1}{z} \frac{1}{(z - z_0)} dz, \tag{3.12}$$

where $z_0 = 2\omega(k)\delta t$ and $\gamma = \{z \in \mathbb{C}, |z - z_0| = 1\}$.

Multistep predictor-corrector integration scheme

We combine the integrating factor with the four-step Adams-Bashforth and three-step Adams-Moulton methods as predictor and corrector methods respectively, as proposed in [69]. These schemes provide solutions to the differential equation $\partial_t y = f(t, y)$ as, respectively,

$$y_{i+1} = y_i + \frac{\delta t}{24}(55f_i - 59f_{i-1} + 37f_{i-2} - 9f_{i-3}), \tag{3.13}$$

or

$$y_{i+1} = y_i + \frac{\delta t}{24}(9f_{i+1} + 19f_i - 5f_{i-1} + f_{i-2}), \tag{3.14}$$

The resulting algorithms for the predictor and corrector steps are, correspondingly,

$$\hat{h}(k, t + \delta t) = e^{\omega(k)\delta t}[\hat{h}(k, t) + \frac{\delta t}{24}(55\hat{\mathcal{N}}(k, t) - 59\hat{\mathcal{N}}(k, t - \delta t)e^{\omega(k)\delta t}+$$
$$+37\hat{\mathcal{N}}(k, t - 2\delta t)e^{2\omega(k)\delta t} - 9\hat{\mathcal{N}}(k, t - 3\delta t)e^{3\omega(k)\delta t})] + \hat{g}(k, t), \qquad (3.15)$$

or

$$\hat{h}(k, t + \delta t) = \hat{h_k}(k, t)e^{\omega(k)\delta t} + \frac{\delta t}{24}(9\hat{\mathcal{N}}(k, t + \delta t) + 19\hat{\mathcal{N}}(k, t)e^{\omega(k)\delta t}-$$
$$-5\hat{\mathcal{N}}(k, t - \delta t)e^{2\omega(k)\delta t} + \hat{\mathcal{N}}(k, t - \delta t)e^{3\omega(k)\delta t}) + \hat{g}(k, t), \qquad (3.16)$$

where the stochastic term $\hat{g}(k, t)$ contained in Eqs. (3.15) and (3.16) is computed as in Eq. (3.11). Due to the multistep nature of the method, the value of h in the first three temporal steps is required prior to the integration, hence the second and third steps need to be computed by means of a single step method.

3.1.2   Burgers equation with conserved noise

The pseudospectral method described above does not work properly in the specific case of the Burgers equation with conserved noise,

$$\partial_t u = \nu\partial_x^2 u + \lambda u \partial_x u + \partial_x \eta, \qquad (3.17)$$

as the latter is conspicuously prone to numerical inaccuracies and instabilities [71]. For this equation, we use the numerical scheme proposed in [72]. It is a finite-differences method in real space which reads

$$\partial_t u_j = \nu\frac{u_{j+1} - 2u_j + u_{j-1}}{\delta x^2}+$$
$$+\lambda\frac{u_{j+1}^2 + u_j u_{j+1} - u_{j-1}u_j - u_{j-1}^2}{3\delta x} + \sqrt{\frac{2D}{\delta t}}(u_j - u_{j-1}). \qquad (3.18)$$

3.2   Numerical method for strongly nonlinear thin film equations

The numerical integration of strongly nonlinear thin film equations which read

$$\partial_t h = -\partial_x \left[\frac{h^3}{3}\partial_x \left(C_1\partial_x^2 h + C_2 F(h)\right)\right], \qquad (3.19)$$

has been carried out by means of a Crank-Nicholson-like scheme, based in the algorithm reported in [73]. For each time step δt, the system of nonlinear equations

$$\frac{h(x_i, t + \delta t) + h(x_i, t)}{\delta t} = -(C_1 \mathcal{I}_i + C_2 \mathcal{E}_i), \tag{3.20}$$

is solved for the unknowns $h(x_i, t + \delta t)$, where $i = 1, ..., N$. Here, $\mathcal{I}$ and $\mathcal{E}$ are the discretizations of the surface tension, $\partial_x \left[\frac{h^3}{3} \partial_x^3 h \right]$, and the $\partial_x \left[\frac{h^3}{3} \partial_x F(h) \right]$ contributions to the thin film Eq. (3.19), for which we use implicit (averaging for times t and $t + \delta t$) and explicit finite-differences schemes respectively, namely,

$$\mathcal{I}_i = \frac{D^+(t)\mathcal{D}_3(x_i^+, t) - D^-(t)\mathcal{D}_3(x_i^-, t)\mathcal{D}_3}{2\delta x^4} +$$
$$\frac{D^+(t)\mathcal{D}_3(x_i^+, t + \delta t) - D^-(t)\mathcal{D}_3(x_i^-, t + \delta t)\mathcal{D}_3}{2\delta x^4} \tag{3.21}$$

and

$$\mathcal{E}_i = \frac{D^+(t)(F(h(x_{i+1}, t)) - F(h(x_i, t)) - D^-(t)(F(h(x_i, t)) - F(h(x_{i-1}, t)))}{\delta x^2}, \tag{3.22}$$

where

$$D^+(\tau) = \frac{h^3(x_{i+1}, \tau) + h^3(x_i, \tau)}{6}, \qquad D^-(\tau) = \frac{h^3(x_{i-1}, \tau) + h^3(x_i, \tau)}{6}, \tag{3.23}$$

$$\mathcal{D}_3(x_i^+, \tau) = h(x_{i+2}, \tau) - 3h(x_{i+1}, \tau) + 3h(x_i, \tau) - h(x_{i-1}, \tau), \tag{3.24}$$

and

$$\mathcal{D}_3(x_i^-, \tau) = h(x_{i+1}, \tau) - 3h(x_i, \tau) + 3h(x_{i-1}, \tau) - h(x_{i-2}, \tau). \tag{3.25}$$

Periodic boundary conditions are implemented in the equations for $i = 1, 2, N - 1, N$. The height vector $\mathbf{h}$ at time t is used as initial condition in order to solve equation (3.20) for the unknowns $h(x_i, t + \delta t)$, $i = 1, ..., N$. From this initial guess, Newton-Raphson iterations are applied in order to solve the nonlinear system of equations. As a result of applying Newton-Raphson, a sequence of iterative pentadiagonal linear systems is obtained, which is solved iteratively until convergence condition

$$\left| \frac{||\mathbf{h}_{\text{iteration } i}|| - ||\mathbf{h}_{\text{iteration } i+1}||}{||\mathbf{h}_{\text{iteration } i}||} \right| < 10^{-8} \tag{3.26}$$

is achieved.

3.3 Monte Carlo integration

In this section we discuss the numerical Monte Carlo method used in order to approximately compute the value of integrals which present difficulties in the analytical or numerical evaluation with standard quadrature schemes [74]. This can be specially useful for large multidimensional integration domains where the integral is not analytically solvable and the number of evaluations for quadrature numerical methods scale too fast with the domain dimension. In this thesis, this tool becomes needed for the estimation of some cumulants via dynamic renormalization gruop (DRG) analysis in Chapters 4 and 5.

If we need to compute the approximate value of $I = \int g(x) \ dx$, we can take advantage of the formula for the expected value of the evaluation of a random variable χ over a function $g(\cdot)$, which reads

$$\langle g(\chi) \rangle = \int g(x) f_\chi(x) \ dx, \tag{3.27}$$

with $f_\chi(x)$ being the probability density function (PDF) of χ. If we multiply and divide the integrand by $f_\chi(x)$, the value of I can be expressed as the expected value of $g/f_\chi(\chi)$, i.e.

$$I = \int \frac{g(x)}{f_\chi(x)} f_\chi(x) \ dx = \left\langle \frac{g(\chi)}{f_\chi(\chi)} \right\rangle. \tag{3.28}$$

Hence we obtain a convenient way to estimate the value of I as

$$I \simeq S_n = \frac{1}{N} \sum_{i=1}^{N} \frac{g(x_i)}{f_\chi(x_i)}, \tag{3.29}$$

with $\{x_i\}_{i=1}^{N}$ being a sequence of independent random f_χ-distributed numbers. The variance of the estimator S_n takes the form

$$Var(S_n) = \frac{1}{N} \sum_{i=1}^{N} \left(\frac{g(x_i)}{f_\chi(x_i)} \right)^2 - S_n^2. \tag{3.30}$$

It vanishes as $N \to \infty$ and decreases as the shape of the function g is more similar to the shape of f_χ. The limit case ($g = c f_\chi$) would nullify the estimator variance, but it is not feasible as we would need to know the exact value for $\int g$ prior to constructing f_χ. This fact allows us to enhance the precision of this method if we choose f_χ as similar as possible to the integrand g.

In the case of the integration of a multivariate function $g(x_1, x_2, ..., x_m)$, the estimator takes the form

$$S_n = \frac{1}{N} \sum_{i=1}^{N} \frac{g(x_{1,i}, x_{2,i}, ..., x_{m,i})}{f_\chi(x_{1,i}) f_\chi(x_{2,i}) ... f_\chi(x_{m,i})}. \tag{3.31}$$

Notice that the variance,

$$Var(S_n) = \frac{1}{N} \sum_{i=1}^{N} \left(\frac{g(x_{1,i}, x_{2,i}, ..., x_{m,i})}{f_\chi(x_{1,i}) f_\chi(x_{2,i}) ... f_\chi(x_{m,i})} \right)^2 - S_n^2, \tag{3.32}$$

also scales as $1/N$, hence the problem scales computationally as the number of random numbers that are need to be generated and evaluated. This fact makes this method much more suitable for integration over high-dimensional domains [74].

3.4 Numerical characterization of time series: Scale-Dependent Lyapunov Exponent

The distinction between stochastic and chaotic random fluctuations in time series plays an important role in Chapter 6, where the competition of both chaotic and stochastic fluctuations is studied in the context of the noisy Kuramoto-Sivashinsky equation. In order to discriminate the character of random fluctuations in time series, we use the so-called Scale-Dependent Lyapunov Exponent $\Lambda(\epsilon)$, a numerical characterization of the effective Lyapunov exponent which was presented in [75, 76]. It is based on the study of how the distance ϵ between different close-by trajectories in the time series diverges over time. The assessment of these trajectories is an efficient tool to reconstruct the attractor of the dynamics as a consequence of Taken's theorem [77].

For each time t we consider that the distance between trajectories is effectively evolving as

$$\epsilon_{t+\Delta t} = \epsilon_t e^{\Lambda(\epsilon_t)t}, \tag{3.33}$$

where $\Lambda(\epsilon_t)$ is the effective Lyapunov exponent

$$\Lambda(\epsilon_t) = \frac{\log \epsilon_{t+\Delta t}/\epsilon_t}{\Delta t}. \tag{3.34}$$

The dependence of is effective Lyapunov exponent with the distance ϵ exhibits different behaviors for different sources of fluctuation in time series. Some relevant possibilities are as follows:
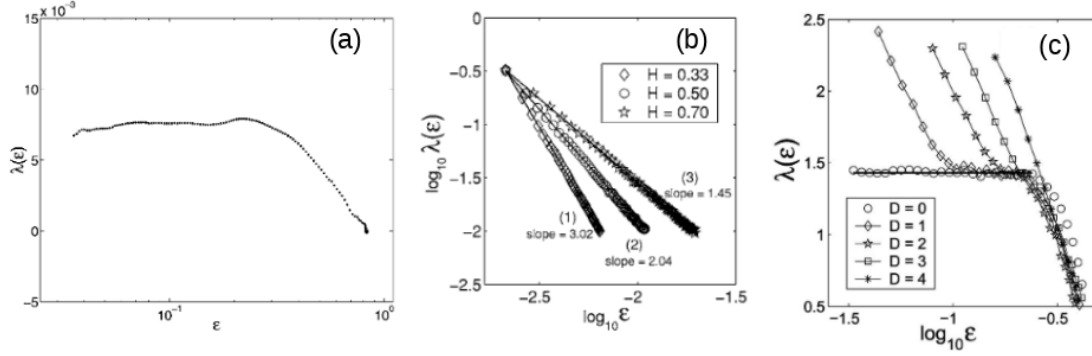
Figure 3.1: *Dependence of the Scale Dependent Lyapunov Exponent (SDLE) Λ (λ in the figure) with the trajectory distance ϵ for (a) a purely chaotic time series (Mackey-Glass delay-differential system), (b) purely stochastic time series (fractional Brownian motion with different values of the Hurst exponent, H) and (c) a chaotic system with stochastic noise of a varying intensity (Lorenz system with strength noise D). These panels are extracted from [75].*

(a) In purely chaotic systems, Λ becomes persistent with ϵ except for large values of ϵ, for which it must decay, as the distance between trajectories can not grow indefinitely, see panel (a) of Figure 3.1.

(b) For purely stochastic systems, consider e.g. a fractional Brownian motion for which the standard deviation of the fluctuations grows as $\sim t^H$, with H being the so-called Hurst exponent (related to the fractal dimension as $d_F = 2 - H$), equivalent to the exponent α for kinetically rough surfaces. In this case, we can easily conclude that Λ decays with ϵ as a power law, see panel (b) of Figure 3.1; indeed,

$$\epsilon_t = \epsilon_0 t^H \quad \Rightarrow \quad \Lambda(\epsilon_t) = \frac{\log\left(\frac{t+\Delta t}{t}\right)^H}{\Delta t} \sim H \, t^{-1} \quad \Rightarrow \quad \Lambda(\epsilon_t) \sim \epsilon_t^{-1/H}. \quad (3.35)$$

(c) In a fluctuating time series subject to both, stochastic and chaotic sources of fluctuations, there is a competition between $\epsilon \sim t^H$ (due to stochastic noise) and $\epsilon \sim e^t$ (due to chaos). Hence, Λ decays as a power-law for low values of ϵ while it remains non-decreasing for larger values of ϵ, see panel (c) of Figure 3.1.
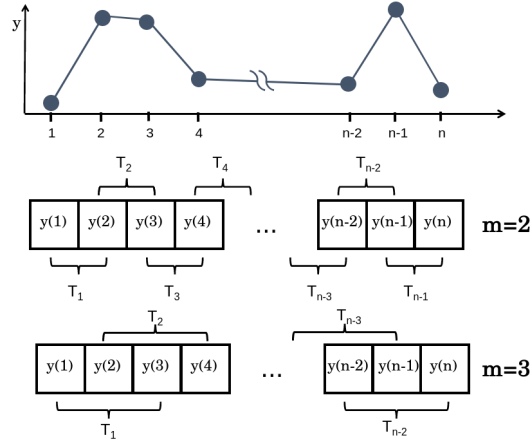
Figure 3.2: Illustration of the trajectory definition in time series, for $m = 2$ and 3.

3.4.1 Numerical implementation of the SDLE

We define trajectories T_i of dimension m from a time series $y(1), ..., y(n)$ as $T_i = (y(i), y(i+1), ..., y(i+m-1))^T$ (see Figure 3.2). We select all pairs of close-by trajectories (i, j) for a certain $\epsilon_0 \ll 1$ such that

$$0 < \frac{||T_i - T_j||}{\max_{k,l} ||T_k - T_l||} < \epsilon_0 \ll 1. \tag{3.36}$$

For each selected pair (i, j) and for several times $t = N\Delta t$, we compute the distances

$$\epsilon_t = ||T_{i+N} - T_{j+N}||, \qquad \epsilon_{t+\Delta t} = ||T_{i+N+1} - T_{j+N+1}||, \tag{3.37}$$

which allows us to compute the effective Lyapunov exponent via Eq. (3.34). We finally define a vector $\vec{\epsilon}$ where ϵ_i are logarithmically equispaced values between the minimun one and the maximum one for all computed ϵ_t, and we bin together the numerical values of $\Lambda(\epsilon_t)$ in order to construct the corresponding Λ.

3.5 Dynamic Renormalization Group

Dynamic renormalization group (DRG) analysis has been successfully employed in order to determine the large-scale behavior of kinetic roughening processes [52, 78]. It is based on an iterative solution of the evolution equation in Fourier space which

consists on a coarse-graining (in which small scales are eliminated) and a later rescaling processes.

We illustrate here the main steps of this procedure for the Burgers equation,

$$\partial_t \phi = \nu \partial_x^2 \phi + \lambda \partial_x (\phi^2) + \eta. \tag{3.38}$$

In Fourier space, the equation can be rewritten as

$$G_0^{-1}(k,\omega)\hat{\phi}(k,\omega) = \hat{\eta}(k,\omega) - \lambda \mathrm{i}k \int_{-\infty}^{\infty} \frac{d\Omega}{2\pi} \int_{-\Lambda_0}^{\Lambda_0} \frac{dq}{2\pi}\ \hat{\phi}(q,\Omega)\hat{\phi}(k-q,\omega-\Omega), \tag{3.39}$$

with

$$G_0(k,\omega) = \frac{1}{-\mathrm{i}\omega + \nu k^2}. \tag{3.40}$$

Here hat is space-time Fourier transform, k is wave-number, ω is time frequency, and i is the imaginary unit.

Coarse-graining

We now take an arbitrary positive parameter ℓ and separate slow ($|k| < \Lambda_0 e^{-\ell}$, denoted by superindex $<$) from fast ($\Lambda_0 e^{-\ell} < |k| < \Lambda_0$, denoted by superindex $>$) Fourier modes, i.e.

$$\hat{\phi} = \hat{\phi}^> + \hat{\phi}^<, \qquad \hat{\eta} = \hat{\eta}^> + \hat{\eta}^<, \tag{3.41}$$

where

$$\hat{\phi}^> = \hat{\eta}^> = 0, \qquad \text{if} \qquad |k| < \Lambda_0 e^{-\ell}, \tag{3.42}$$

$$\hat{\phi}^< = \hat{\eta}^< = 0, \qquad \text{if} \qquad |k| > \Lambda_0 e^{-\ell}. \tag{3.43}$$

Equation (3.39) for slow and fast modes become, respectively,

$$G_0^{-1}(k,\omega)\hat{\phi}^<(k,\omega) = \hat{\eta}^<(k,\omega) - \lambda \mathrm{i}k \int_{-\infty}^{\infty} \frac{d\Omega}{2\pi} \int_{-\Lambda_0}^{\Lambda_0} \frac{dq}{2\pi} \times$$
$$\times [\hat{\phi}^<(q,\Omega)\hat{\phi}^<(k-q,\omega-\Omega) + \hat{\phi}^>(q,\Omega)\hat{\phi}^>(k-q,\omega-\Omega) +$$
$$+ \hat{\phi}^>(q,\Omega)\hat{\phi}^<(k-q,\omega-\Omega) + \hat{\phi}^<(q,\Omega)\hat{\phi}^>(k-q,\omega-\Omega)], \tag{3.44}$$

and

$$G_0^{-1}(k,\omega)\hat{\phi}^>(k,\omega) = \hat{\eta}^>(k,\omega) - \lambda \mathrm{i}k \int_{-\infty}^{\infty} \frac{d\Omega}{2\pi} \int_{-\Lambda_0}^{\Lambda_0} \frac{dq}{2\pi} \times$$
$$\times [\hat{\phi}^<(q,\Omega)\hat{\phi}^<(k-q,\omega-\Omega) + \hat{\phi}^>(q,\Omega)\hat{\phi}^>(k-q,\omega-\Omega) +$$
$$+ \hat{\phi}^>(q,\Omega)\hat{\phi}^<(k-q,\omega-\Omega) + \hat{\phi}^<(q,\Omega)\hat{\phi}^>(k-q,\omega-\Omega)]. \tag{3.45}$$

We expand the fast modes $\hat{\phi}^>$ into a perturbative series in λ as

$$\hat{\phi}^> = \hat{\phi}_0^> + \lambda\hat{\phi}_1^> + \lambda^2\hat{\phi}_2^> + \mathcal{O}(\lambda^3). \tag{3.46}$$

Using this expansion, we can compute $\hat{\phi}_i^>$ solving Eq. (3.45) at order λ^i for each i. That allows us to rewrite Eq. (3.44) as

$$G^{-1}(k,\omega)\hat{\phi}^<(k,\omega) = \hat{\eta}^<(k,\omega) - \lambda ik \int_{-\infty}^{\infty} \frac{d\Omega}{2\pi} \int_{-\Lambda_0}^{\Lambda_0} \frac{dq}{2\pi} \hat{\phi}^<(q,\Omega)\hat{\phi}^<(k-q,\omega-\Omega), \tag{3.47}$$

where

$$G(k,\omega) = \frac{1}{-\mathrm{i}\omega + \nu k^2 + \Sigma(k,\omega)}. \tag{3.48}$$

Working within the one-loop approximation (up to order λ^2), $\Sigma(k,\omega)$ is computed as [52, 8]

$$\begin{aligned}
\Sigma(k,\omega) &= 4\lambda^2 \int^> \frac{dq}{2\pi} \mathrm{i}k\, \mathrm{i}(k-q) \int_{-\infty}^{\infty} \frac{d\Omega}{2\pi} \\
&\times |G_0(q,\Omega)|^2 G_0(k-q,\omega-\Omega), \tag{3.49}
\end{aligned}$$

where the integration domain in $\int^>$ is the fast modes region $\{q \in \mathbb{R}|\, \Lambda(\ell) = \Lambda_0 e^{-\ell} < |q| < \Lambda_0\}$. The Feynman representation of this equation is depicted in Fig. 3.3(a). After integration in the time frequency Ω, taking the long-time limit $\omega \to 0$,

$$\begin{aligned}
\Sigma(k,\omega) &= -4\lambda^2 \int^> \frac{dq}{2\pi} \frac{Dk(k-q)}{\nu^2 q^2(k^2 - 2kq + 2q^2)} \\
&= -4\lambda^2 \int^> \frac{dq}{2\pi} \left[\frac{3Dk^2}{4\nu^2 q^4}\right] + \mathcal{O}(k^3) \\
&= \frac{6D\lambda^2 k^2}{\nu^2\pi\Lambda^3(\ell)}(e^{-3\ell} - 1) + \mathcal{O}(k^3). \tag{3.50}
\end{aligned}$$

As we are interested in the large-scale behavior, only the lowest order in k will be considered. For convenience, we identify $k = \Lambda_0 e^{-\ell}$ in order to be able to discriminate different values of k. We define a coarse-grained $\nu^<(\ell)$ in the long-time limit such that $G(k,0) = [\nu_<(\ell)k^2]^{-1}$ [78],

$$\frac{1}{\nu_<(\ell)k^2} = \frac{1}{\nu k^2} + \frac{1}{\nu^2 k^4}\frac{6D\lambda^2 k^2}{\nu^2\pi\Lambda^3(\ell)}(e^{-3\ell} - 1) \tag{3.51}$$

$$\Rightarrow \frac{1}{\nu_<(\ell)} = \frac{1}{\nu}\left[1 + \frac{6D\lambda^2}{\nu^3\pi\Lambda^3(\ell)}(e^{-3\ell} - 1)\right]$$

$$\Rightarrow \nu_<(\ell) = \nu\left[1 - \frac{6D\lambda^2}{\nu^3\pi\Lambda^3(\ell)}(e^{-3\ell} - 1)\right]. \tag{3.52}$$

Rescaling

After coarse-graining, we proceed to rescale the DRG flow. We rescale space and time as $\tilde{x} = bx$, $\tilde{t} = b^z t$, and $\tilde{\phi} = b^{-\alpha}\phi(\tilde{x}, \tilde{t})$. Burgers equation under rescaled parameters (dropping tildes) reads

$$\partial_t \phi = \nu b^{z-2} \partial_x^2 \phi + \lambda b^{\alpha+z-1} \partial_x \phi^2 + D b^{z-2\alpha-1} \eta. \tag{3.53}$$

Now we take $b = e^\ell$. In the limit of vanishing $\ell = \delta\ell \to 0$, the DRG flow equations for the renormalized (coarse-grained and rescaled) parameters $\tilde{\nu} = \nu_< b^{z-2}$ (using $\nu_<$ as in Eq. (3.51)), $\tilde{\lambda} = \lambda b^{\alpha+z-1}$, and $\tilde{D} = D b^{z-2\alpha-1}$ read

$$\frac{d\lambda}{d\ell} = \lim_{\delta\ell \to 0} \frac{\tilde{\lambda} - \lambda}{\delta\ell} = \lambda(\alpha + z - 1), \tag{3.54}$$

$$\frac{dD}{d\ell} = \lim_{\delta\ell \to 0} \frac{\tilde{D} - D}{\delta\ell} = D(z - 2\alpha - 1), \tag{3.55}$$

$$\frac{d\nu}{d\ell} = \lim_{\delta\ell \to 0} \frac{\tilde{\nu} - \nu}{\delta\ell} = \nu\left(z - 2 + \frac{18D\lambda^2}{\nu^3 \pi \Lambda_0^3}\right). \tag{3.56}$$

The fixed points of this flow must fulfill

$$\frac{d\lambda}{d\ell} = \frac{dD}{d\ell} = \frac{d\nu}{d\ell} = 0. \tag{3.57}$$

- Requesting scale invariance at a non-linear ($\lambda \neq 0$) critical point, leads to $\alpha + z = 1$, a scaling relation associated with the *Galilean invariance* of Burgers equation [8].

- Non-trivial fluctuations ($D \neq 0$) at the fixed point lead to *hyperscaling* [52, 8], $2\alpha + d = z$ (with $d = 1$), here due to the fact that dynamics are conserved, but the noise is not [79].

For the noisy Burgers equation, these two scaling relations are believed to hold at any order in the loop expansion [52, 56].

Large-scale behavior without rescaling

We can alternatively study the large scale behavior of Burgers equation without the rescaling of the parameters. This allows us to make explicit the scale-dependence of the equation parameters, as proposed in [78]. For that purpose, Eq. (3.51) is conveniently rewritten as a differential flow. We must take ν as $\nu_<(\ell)$ and consider $\Lambda(\ell) \ll 1$, as we are interested in the large-scale behavior. Thus, the differential flow for $\nu_<(\ell)$ reads

$$\frac{d\nu_<(\ell)}{d\ell} = \frac{18D\lambda^2}{\nu_<^2(\ell)\pi\Lambda^3(\ell)}, \tag{3.58}$$

whose solution for the initial condition $\nu_<(0) = \nu$ is

$$\nu_<(\ell) = \left[\frac{\nu^3}{3} + \frac{6D\lambda^2}{\nu^3\pi\Lambda_0^3}(e^{3\ell} - 1)\right]^{1/3}. \tag{3.59}$$

In the large-scale limit when $\ell \gg 1$, the renormalized coefficient $\nu_<$ scales with wavenumber k as [52]

$$\nu_<(k) \sim \left(\frac{6D\lambda^2}{\nu^3\pi}\right)^{1/3} |k|^{-1}. \tag{3.60}$$

Hence, the coarse-grained propagator takes the form

$$G(k,\omega) = \frac{1}{-\mathrm{i}\omega + \nu_<(k)k^2} = \frac{1}{-\mathrm{i}\omega + \left(\frac{6D\lambda^2}{\nu^3\pi}\right)^{1/3}|k|}, \tag{3.61}$$

and we obtain the value of the dynamic exponent $z = 1$, as $G(k,0) \sim 1/|k|^z$ in analogy with linear models. The value of the roughness exponent α can be determined by means of the study of the scale dependence of the second cumulant (variance) of the fluctuations, which is presented in the next section.

3.5.1   DRG determination of cumulants

We are able to exploit the dependence with the scale of the coarse-grained propagator to estimate by DRG the cumulants of the statistical distribution of ϕ, following the methodology successfully employed for the KPZ [80, 81, 82] and NLMBE [83] equations. The n-th cumulant in Fourier space reads

$$\langle\phi^n\rangle_c = \int_{\mathbb{R}^{2n}} \prod_{j=1}^n \frac{dk_j d\omega_j}{(2\pi)^2} e^{\mathrm{i}(k_j x - \omega_j t)} \left\langle \prod_{j=1}^n \hat{\phi}_j \right\rangle. \tag{3.62}$$

(a)

(b)
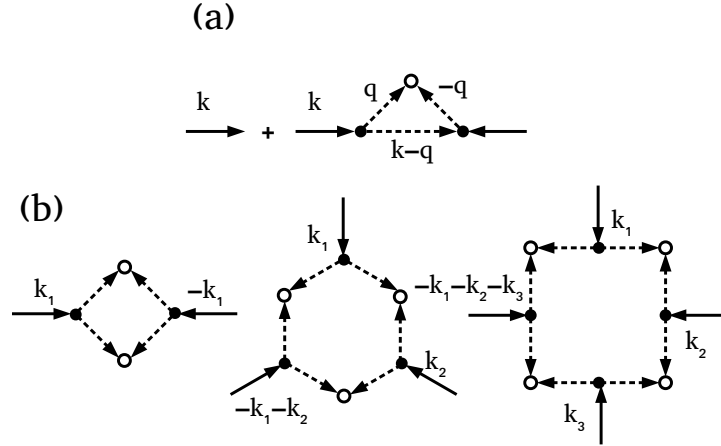
Figure 3.3: *Feynman diagrams representing (a) Eq. (3.49) and (b) the lowest-order correc-
tions to the cumulants, $L_{n,1}$, for $n = 2, 3, 4$, left to right. Bare propagator factors $G_0(q)$
evaluated for low $[|q| < \Lambda(\ell)]$ and high $[\Lambda(\ell) < |q| < \Lambda_0]$ wave vectors correspond to solid
and dashed lines, respectively. Noise contractions (convolution products) are represented
by open (filled) disks.*

In terms of renormalized quantities, it takes the form

$$\langle \phi^n \rangle_c = \int_{\mathbb{R}^{2(n-1)}} G(k_n, \omega_n) L_n \prod_{j=1}^{n-1} \frac{dk_j d\omega_j}{(2\pi)^2} G(k_j, \omega_j), \tag{3.63}$$

where $k_n = -\sum_{j=1}^{n-1} k_j$, $\omega_n = -\sum_{j=1}^{n-1} \omega_j$, and the function L_n is perturbatively
computed to one loop order [80, 81, 82, 83] as

$$L_n = (2D)\delta_{n,2} + L_{n,1}, \tag{3.64}$$

where $L_{n,1} = K(2D)^n \lambda^n i^n k_n \prod_{j=1}^{n-1} k_j l_{n,1}$ is the lowest-order correction in the Feyn-
man expansion of the cumulants and $K = (2n-2)!!$ is a combinatorial factor (number
of different fully-connected diagrams). Diagrammatic representations for $L_{2,1}$, $L_{3,1}$,
and $L_{4,1}$ correspond to the amputated parts of the diagrams shown in Fig. 3.3(b).

As we are interested in the hydrodynamic $(k_i, \omega_i) \to (0, 0)$ limit (large spatiotem-
poral scales),

$$l_{n,1} = \int_{-\infty}^{\infty} \frac{d\Omega}{2\pi} \int^{>} \frac{dq}{2\pi} |G_0(q, \Omega)|^{2n}. \tag{3.65}$$

After integration, and substituting $\nu \to \nu_<(\Lambda)$,

$$l_{n,1} = \frac{\sqrt{\pi}\Gamma(n-\frac{1}{2})}{n!\left(\frac{6D\lambda^2}{\pi}\right)^{2n-1}}\frac{2\left(1 - e^{-(4n-3)\ell}\right)}{(4n-3)\Lambda^{2n-2}(\ell)}. \tag{3.66}$$

We rewrite this equation in differential form as

$$\frac{dl_{n,1}}{d\ell} = \frac{\sqrt{\pi}\Gamma(n-\frac{1}{2})}{n!\left(\frac{6D\lambda^2}{\pi}\right)^{2n-1}}\frac{2}{\Lambda^{2n-2}(\ell)}, \tag{3.67}$$

whose solutions for large ℓ become

$$l_{n,1}(\ell) \simeq \frac{\sqrt{\pi}\Gamma(n-\frac{1}{2})}{n!\left(\frac{6D\lambda^2}{\pi}\right)^{2n-1}(n-1)}\frac{1}{\Lambda^{2(n-1)}(\ell)}. \tag{3.68}$$

Due to the symmetry among $k_1, \ldots, k_{n-1}$, we take [80, 81, 82, 83]

$$l_{n,1}(k) = \frac{\sqrt{\pi}\Gamma(n-\frac{1}{2})}{n!\left(\frac{6D\lambda^2}{\pi}\right)^{2n-1}(n-1)}\prod_{i=1}^{n-1}\frac{1}{k_i^2}. \tag{3.69}$$

For $n > 2$, as $|G(k,\omega)| = |k|^{-z}f(\omega/|k|^z)$ and $z = 1$, where f is a scaling function $[f(u) \to 1$ for $u \to 0]$, $k_i^{-2} \simeq |G(k_i, \omega_i)|^2$. Finally,

$$\begin{aligned}
\langle\phi^n\rangle_c &= \frac{A}{D^{n-1}\lambda^{3n-2}}\int_{\mathbb{R}^{2(n-1)}}G(k_n,\omega_n)k_n \\
&\times \prod_{i=1}^{n-1}\frac{dk_i d\omega_i}{(2\pi)^2}k_i G(k_i,\omega_i)|G(k_i,\omega_i)|^2,
\end{aligned} \tag{3.70}$$

where $A = \pi^{2n-\frac{1}{2}}i^n\Gamma(n-\frac{1}{2})K/[n!(n-1)3^n 2^{2n-1}]$.

Variance

Integration of Eq. (3.70) for $n = 2$ yields the variance (square of roughness) of ϕ,

$$\langle\phi^2\rangle_c = \frac{1}{(3072\pi^2)^{1/3}}\left(\frac{D}{\lambda}\right)^{2/3}\int_{\mathbb{R}}\frac{dk}{|k|}, \tag{3.71}$$

whose logarithmic divergence ($\sim \log L$) agrees with the expected value of the roughness exponent, $\alpha = 0$ [16, 11]. Higher-order cumulants estimated by this approach are further discussed in Chapters 4 and 5.

Chapter 4

Gaussian statistics as an emergent symmetry of the stochastic scalar Burgers equation

4.1 Introduction

4.1.1 The stochastic Burgers equation (non-conserved noise)

In Chapter 2 we derived the Kuramoto-Sivashinsky equation as an effective interface equation for a thin fluid film falling down a slope. A stochastic generalization of this equation can be derived as an interface model when the substrate height is disordered and subject to small random vibrations, as done in [49]; such a model reads

$$\partial_t h + \nu_0 \partial_x^2 h + \kappa_0 \partial_x^4 h + \lambda_0 h \partial_x h + \eta = 0, \tag{4.1}$$

where η is *non-conserved*, zero-mean, uncorrelated Gaussian noise, such that

$$\langle \eta(x,t)\eta(x',t') \rangle = 2D\delta(x-x')\delta(t-t'). \tag{4.2}$$

As $\kappa_0 = 1/(3\text{Ca}')$ (where $\text{Ca}' \propto \gamma^{-1}$ is the capillarity number) and $\nu_0 = 8\text{Re}\sin^2\theta/15 - 2\cos\theta/3$ (where Re is the Reynolds number and θ is the angle of the slope), Burgers equation,

$$\partial_t \phi = \nu\partial_x^2\phi + \lambda\phi\partial_x\phi + \eta = 0, \tag{4.3}$$

is obtained in the viscous $\text{Re} = 0$ and ultra-low surface tension ($\gamma = 0$) limit of Eq. (4.1), taking $\phi = h$, $\nu = 2\cos\theta/3$, and $\lambda = \lambda_0 = 4\sin\theta$. As mentioned in Chapter

1, Burgers equation, Eq. (4.3), is a paradigm for non-equilibrium physics, appearing not only as a thin film model but also in many other different contexts, like traffic models, cosmology, or turbulence, with different meanings for the field ϕ, like vehicle density, mass density, or fluid velocity, respectively [54].

Moreover, the scalar Eq. (4.3) can be generalized to $d = 2$ as, e.g. [55]

$$\partial_t \phi = \nu_x \ \partial_x^2 \phi + \nu_y \ \partial_y^2 \phi + \lambda_x \ \phi \partial_x \phi + \lambda_y \ \phi \partial_y \phi + \eta. \tag{4.4}$$

The particular $\lambda_y = 0$ case was originally introduced by Hwa and Kardar (HK) as a continuum model of avalanches in running sandpiles [56] in the context of self-organized criticality. We refer to the full Eq. (4.4) as the generalized Hwa-Kardar (gHK) equation [15].

4.1.2   Symmetry emergence: KPZ vs Burgers

Spontaneous symmetry *breaking* is a basic notion in Physics underlying collective behavior in classical and quantum systems [84]. Among other important phenomena, it provides the mechanism for continuous phase transitions in equilibrium Statistical Mechanics, wherein the macroscopic state of a system shows a reduced symmetry compared with the microscopic interactions when temperature T is below a certain threshold T_c. As is well known, the corresponding (critical) system is remarkably characterized by scale-invariant behavior right at $T = T_c$ [85]. The converse situation of *emergent symmetries* occurs when the system symmetries *increase* for a decreasing T [86]. This can occur even for non-equilibrium systems, whose large-scale behavior can display symmetries which are not explicit in the microscopic description. Recent examples include driven exciton-polariton condensates [87], which give rise to novel dynamic universality classes beyond the standard classification of dynamical phase transitions [88].

Actually, the generalization of the criticality concept to non-equilibrium conditions is proving itself a truly fruitful avenue to enlarge the domain of applicability of Statistical Physics, to e.g. socio-technological [89] or living [90] systems. In this process, an important conceptual role is being played by the elucidation of conditions for the generic occurrence of critical behavior without the need (in contrast with equilibrium systems) for parameter tuning, both in the presence or absence of a time-scale separation between external driving and system relaxation, termed respectively self-organized criticality (SOC) [91] or generic scale invariance (GSI) [79, 88], in which kinetic roughening, one of the paradigmatic surface self-organization processes presented in Chapter 1, is the particular case of GSI in the specific context of surface growth.

In the absence of noise, Burgers equation Eq. (4.3) is obtained as the space-derivative of the deterministic KPZ equation, with $\phi = \partial_x h$ [17]. The full stochastic Eq. (4.3) can still be interpreted as the space derivative of a generalization of the full Eq. (1.42) for a specific type of space-correlated noise, see e.g. [92]. We presently view Eq. (4.3) as an instance of conserved dynamics with non-conserved noise (hence, displaying kinetic roughening [88, 79]) which shares with the KPZ equation, Eq. (1.42), the celebrated Galilean invariance [52] (i.e., it remains invariant under a Galilean change of coordinates) and the lack of symmetry under reflection in the field, $\phi \leftrightarrow -\phi$. Equation (4.3) also shares the type of dynamics and noise, and the lack of up-down symmetry, with the NLMBE equation. However, as shown in this Chapter, and in contrast with the cases of the latter and of the KPZ equation, the field statistics for Eq. (4.3) are Gaussian at large scales, an effective up-down symmetry emerging in its asymptotic nonlinear behavior which differs from expectations based on straightforward analysis of the symmetries of its "microscopic" description. We reach this conclusion through a combined numerical and renormalization-group (RG) study which addresses the statistics of the physical field through its cumulants (analytically), and the full PDF (numerically). We show how this symmetry emergence does also occur at higher dimension [Eq. (4.4)] and for some other model equations with the same bare symmetries as Eq. (4.3).

4.2 Universality class of the stochastic Burgers equation

4.2.1 Scaling exponents

The scaling exponents which characterize the kinetic roughening of Eqs. (4.3) and (4.4) have been investigated analytically [52, 56, 92, 55] and numerically [15, 55, 93], and are collected in Table 4.1. Note, HK scaling is anisotropic, hence the different exponent values along the x and y directions, while $\alpha_x/z_x = \alpha_y/z_y = \beta$ [15]. As an illustration, Fig. 4.1(a) shows the time evolution of the structure factor for Eq. (4.3), $S(\vec{k}, t) = \langle |\tilde{\phi}(\vec{k}, t)|^2 \rangle$, where tilde is space Fourier transform, $\vec{k}$ is wave vector, and brackets are noise averages. Here and below, numerical simulations employ the pseudospectral method developed in [69] and described in Chapter 3 for periodic systems. As expected, for $|\vec{k}|$ larger than the inverse correlation length, power-law behavior ensues as $S(|\vec{k}|) \sim |\vec{k}|^{-(2\alpha+d)}$ [8, 11, 29] (see Family-Vicsek scaling in Chapter 1). For Eq. (4.3), the system crosses over from linear behavior at short
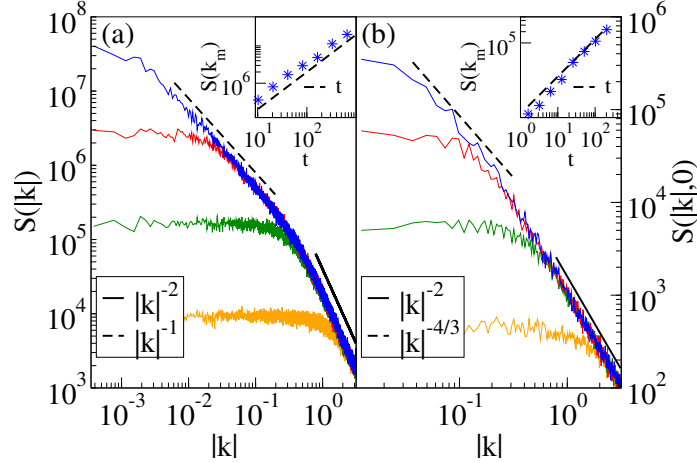
Figure 4.1: $S(\vec{k}, t)$ vs k for increasing times [bottom to top, (a) $t = 0.32, 5.1, 82, 1300$; (b) $t = 0.8, 6.4, 51, 410$] for (a) Eq. (4.3), $L = 2^{14}$, and (b) Eq. (4.4) [cuts of $S(k_x, k_y)$ for $k_y = 0$, $L = 2^9$], for $\nu = \lambda = \nu_x = \lambda_x = \nu_y = \lambda_y = D = 1$. Insets show $S(k_m, t)$ vs t. Straight lines have the behavior indicated in the corresponding legends, with dashed lines using the exponent values given in Table 4.1. All units are arbitrary.

Equation	α_x	α_y	z_x	z_y	β
1D Burgers	0	not defined	1	not defined	0
Hwa-Kardar	$-1/5$	$-1/3$	$6/5$	2	$-1/6$
g Hwa-Kardar	$-1/3$	$-1/3$	$4/3$	$4/3$	$-1/4$

Table 4.1: Scaling exponents for Eqs. (4.3), (4.4) [52, 56, 15, 92, 55, 93].

times and large $|\vec{k}|$ [the $|\vec{k}|$-dependent behavior of $S(|\vec{k}|) \sim |\vec{k}|^{-2}$ being induced by the linear term in the equation] to nonlinear behavior at long times and small $|\vec{k}|$, where $S(|\vec{k}|) \sim |\vec{k}|^{-1}$, inducing $\alpha = 0$. In turn, $z = 1$ is implied [inset of Fig. 4.1(a)] by the $S(k_m, t) \sim t^{(2\alpha+d)/z}$ scaling at the smallest wave vector in the system, $k_m = 2\pi/L$ [8, 11, 29] (see Family-Vicsek scaling in Chapter 1). The numerical data in Fig. 4.1(b) can be similarly discussed to justify the corresponding entries in Table 4.1 for the asymptotic behavior of the gHK equation in $d = 2$, see likewise [15] for HK.

While $\alpha \leq 0$ as in Table 4.1 usually indicates that d is at or above the upper-critical dimension d_c [84, 85], for Eqs. (4.3) and (4.4) $d_c = 4$ has been demonstrated

[52, 56]. Specifically, for Eq. (4.3) $\alpha = 0$ suggests the validity of the Gaussian approximation, while asymptotics are nonlinear. Hence, it is interesting to study the scaling behavior of this equation in detail. We resort to a dynamic renormalization group (DRG) analysis, which has been successfully employed in this context [52, 78], being based on an iterative solution of Eq. (4.3) in Fourier space. Actually, the DRG analysis of Eq. (4.3) has been discussed in detail as an illustrative example of this analytical tool in Chapter 3. After coarse-graining and rescaling, the one-loop DRG flow for parameters ν, λ, and D reads as in Equations (3.54)-(3.56). Requesting scale invariance at a non-linear ($\lambda \neq 0$) critical point leads to $\alpha + z = 1$, associated with the Galilean invariance of Eq. (4.3). Non-trivial fluctuations ($D \neq 0$) require non-renormalization of the noise, leading to hyperscaling [52, 8], $2\alpha + d = z$ (with $d = 1$), due to the fact that dynamics are conserved but the noise is not [79]. These two scaling relations are believed to hold at any order in the loop expansion [52, 56]. They provide an equation set for α and z whose unique solution in $d = 1$ (2) is the one given for the Burgers equation (gHK) in the corresponding row of Table 4.1. The case of the gHK equation is discussed in [55].

4.2.2   Fluctuation statistics

Having determined the scaling exponents, we henceforth perform a partial RG transformation only, which omits the rescaling step. This allows us to make explicit the scale-dependence of the equation parameters, as proposed in [78]. While λ and D do not renormalize and are thus scale-independent, the coarse-grained linear coefficient $\nu_<(k)$ depends on wave vector as $\nu_<(k) \sim |k|^{-1}$ (see DRG section in Chapter 3). We exploit this fact to estimate by DRG the cumulants of the statistical distribution of ϕ, following the methodology successfully employed for the KPZ [80, 81, 83] and NLMBE [82] equations. We obtained in Chapter 3 that the cumulants $\langle \phi^n \rangle_c$ are given by the expression

$$
\begin{aligned}
\langle \phi^n \rangle_c &= \frac{A}{D^{n-1}\lambda^{3n-2}} \int_{\mathbb{R}^{2(n-1)}} G(k_n, \omega_n) k_n \\
&\times \prod_{i=1}^{n-1} \frac{dk_i d\omega_i}{(2\pi)^2} k_i G(k_i, \omega_i) |G(k_i, \omega_i)|^2,
\end{aligned}
\tag{4.5}
$$

where $k_n = -\sum_{j=1}^{n-1} k_j$, $\omega_n = -\sum_{j=1}^{n-1} \omega_j$, and A is a numerical constant. The estimation for the second cumulant yields the variance of ϕ,

$$
\langle \phi^2 \rangle_c \sim \int_{\mathbb{R}} \frac{dk}{|k|},
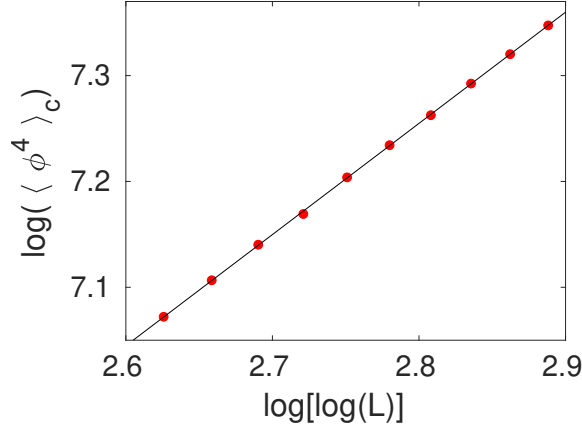\tag{4.6}
$$

Figure 4.2: *Numerical computation of the fourth cumulant in $[k_1, k_2, k_3] \in [1/L, L]^3$, for different values of L (symbols). The solid line shows a linear fit of the numerical data, and corresponds to the straight line $y = 1.05x + 4.314$, hence $\langle \phi^4 \rangle_c \sim (\log L)^{1.05}$.*

whose logarithmic divergence ($\sim \log L$) agrees with the expected value of the roughness exponent, $\alpha = 0$ [16, 11]. Continuing with even-order cumulants, the fourth cumulant is estimated by means of analytical integration in time frequencies ω_i and numerical integration in wavenumbers k_j. Specifically, using a lower cut-off for the latter, $\mu \propto 1/L$, in the $10^{-3} - 10^{-8}$ range, the integral (to simplify the notation, we drop ω-dependencies in G and L_4)

$$\langle \phi^4 \rangle_c = \int_{\mathbb{R}^3} \prod_{i=1}^{3} \frac{d\omega_i}{2\pi} \iiint_{\mu \leq |k_j| \leq \Lambda_0} \prod_{j=1}^{3} \frac{dk_j}{2\pi} \times$$

$$\times G(k_1)G(k_2)G(k_3)G(-k_1 - k_2 - k_3)L_4(k_1, k_2, k_3) \qquad (4.7)$$

has been estimated for different values of the system size L by means of analytical integration in $\omega_1, \omega_2, \omega_3$, and numerical integration in k_1, k_2, k_3. Parameters have been chosen so as to make $A = 1$ and $6D\lambda^2/\pi = 1$, see Eq. (4.5). Integration limits in k_1, k_2, k_3 of the form $[1/L, L]$ have been used for different values of L in order to characterize the divergence of the integral with L. The conclusion is that $\langle \phi^4 \rangle_c \sim (\log L)^{1.05}$, see Fig. 4.2. Thus, the excess kurtosis of the distribution, $\mathcal{K}_e = \langle \phi^4 \rangle_c / \langle \phi^2 \rangle_c^2$, vanishes for increasing system size ($L \to \infty$).

For odd cumulants (odd n), after integration in $\omega_1, ..., \omega_{n-1}$, the integrand of Eq. (4.5) can be represented as $k_n g(k_1, ..., k_n) \prod_{i=1}^{n-1} k_i$, where all k_i in $g(\cdot)$ are to

be taken in absolute value and $g(\cdot)$ is a function. Now, this expression is anti-symmetric under the transformation $k_i \mapsto -k_i$, which maps the semispace $S_+ = \{(k_1, ..., k_{n-1}) \in \mathbb{R}^{n-1} | \sum_{i=1}^{n-1} k_i > 0\}$ into $S_- = \{(k_1, ..., k_{n-1}) \in \mathbb{R}^{n-1} | \sum_{i=1}^{n-1} k_i < 0\}$. Hence, the integral over the full $\mathbb{R}^{n-1}$ cancels exactly. Thus, all the odd cumulants of the ϕ distribution are zero. Indeed, denoting the PDF of a stochastic variable X by $P(X) = \mathcal{F}^{-1}\{\exp[\sum_{n=1}^{\infty}(\mathrm{i}s)^n C_n(X)/n!]\}$, where $C_n(X)$ are the cumulants, $\mathcal{F}$ is Fourier transform and s is conjugate to X, as $\mathcal{F}$ preserves the parity of a function, all the odd-order cumulants being zero lead to a symmetric PDF [94]. In conclusion, with null odd cumulants and an excess kurtosis which decreases for increasing L, these analytical results indeed suggest Gaussian statistics for the field fluctuations in the stochastic Burgers equation (4.3). The exact cancellation of the odd cumulants is particularly remarkable, in view of the lack of up-down symmetry in the equation.

Given the approximations made in our one-loop DRG analysis, we have carried out direct numerical simulations of the Burgers, the HK, and the gHK equations, in order to explicitly compute the full PDF in each case. Histograms have been constructed for times both in the nonlinear growth regime ($t_0 = 0, \Delta t \ll t_{sat}$) and after saturation to steady state ($t_0 > t_{sat}$), using $L = 2^{20}$ for Burgers and $L = 2^{10}$ for the HK and gHK equations; other parameters are as in Fig. 4.1. In all cases the PDF is Gaussian to a high precision, compare the symbols in Fig. 4.3 with the exact Gaussian form (solid line). More quantitatively, Fig. 4.3 also shows the time evolution of the skewness $\mathcal{S} = \langle X^3 \rangle_c / \langle X^2 \rangle_c^{3/2}$ and excess kurtosis $\mathcal{K}_e = \langle X^4 \rangle_c / \langle X^2 \rangle_c^2$, where X is defined as in Eq. (1.46). While $\mathcal{S}(\Delta t)$ remains essentially null in all cases for Eqs. (4.3) and (4.4), convergence of $\mathcal{K}_e$ to zero requires sufficiently large Δt, specially for Eq. (4.3). All this supports our conclusions from the DRG analysis of the stochastic Burgers equation.

4.3   Exact linear approximation

The $\alpha = 0$, $z = 1$ values thus obtained for the asymptotics of Eq. (4.3) happen to equal those of the *linear, non-local* continuum model that describes diffusion-limited erosion (DLE) [16, 11],

$$\partial_t \tilde{\phi} = -|k|\tilde{\phi} + \tilde{\eta}, \tag{4.8}$$

which, in real space, takes the form

$$\partial_t \phi = -\partial_x \mathcal{H}[h] + \eta, \tag{4.9}$$
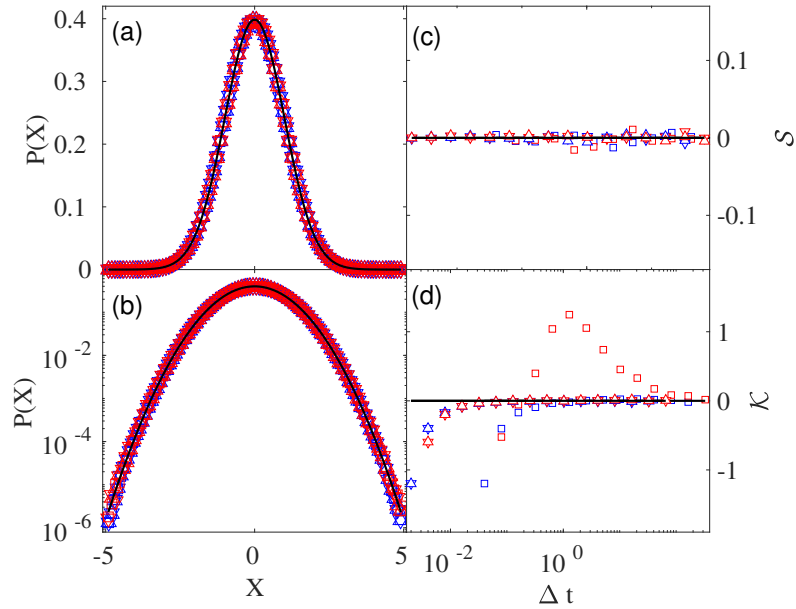
Figure 4.3: *Fluctuation histogram [(a), (b)] from direct simulations of the Burgers ($\square$), HK ($\triangle$), and gHK ($\triangledown$) equations, Eqs. (4.3) and (4.4). Here, X is as in Eq. (1.46), blue (red) denotes $t_0 = 0, \Delta t \ll t_{sat}$ ($t_0 > t_{sat}$), with $\Delta t \gg 1$. Full time evolution of the (c) skewness, $\mathcal{S}$ and (d) excess kurtosis, $\mathcal{K}_e$. Symbols as in (a,b). Convergence to Gaussian (zero) values occurs in all cases.*

as was discussed in Chapter 1. Let us note that, since the scaling exponents of Eqs. (4.3) and (4.4) fulfill hyperscaling, as does any linear model [11], an interesting consequence of our results is that evolution equations can be formulated which share with Eqs. (4.3) and (4.4) both, the exponent values and the Gaussian statistics, but which are linear (thus, up-down symmetric)! Namely, the Gaussian approximation becomes asymptotically exact in these cases. In general, by writing

$$\partial_t \tilde{\phi} = \big(- \sum_{i=1}^{d} |k_i|^{z_d} \big) \tilde{\phi} + \tilde{\eta},$$

(4.10)

the choice $z_1 = 1$ in $d = 1$ [the continuum DLE model, Eq. (4.8) [16, 11]] yields the asymptotic behavior of Eq. (4.3), while in $d = 2$, choosing $z_2 = 4/3$ provides the exponents and Gaussian statistics of the gHK equation, and similarly for the HK model using $z_2 = 6/5$ and dropping the k_y-dependence [15].

4.4   Symmetry discussion

Focusing on the stochastic Burgers equation, it is the nonlinear term $\phi \partial_x \phi$ which is responsible for the up-down asymmetry, and it indeed plays an essential role in the nontrivial behavior described above. We can rationalize the emergence of the up-down symmetry in the asymptotic nonlinear regime by considering the effect of this term when isolated, i.e. for the inviscid ($\nu = 0$) and deterministic ($D = 0$) Burgers equation, whose solutions are known analytically [54, 95]. Note that the nonlinearity also breaks the left-right ($x \leftrightarrow -x$) symmetry in the system and indeed, as is well known, it generically induces sawtooth-like profiles [54, 95, 96], which notably are symmetric around their mean under a *combined* $(x, \phi) \leftrightarrow (-x, -\phi)$ reflection. Analogous behavior also occurs in the full $\nu \neq 0$, $D \neq 0$ stochastic Burgers equation, becoming even apparent to the naked eye in the asymptotic regime. This is illustrated in Fig. 4.4, where typical morphologies are shown in the linear and nonlinear regimes. For the latter, the parallel straight lines allow us to identify portions of the profile which are "noisy sawtooths". Quantitative confirmation is provided by the slope histogram $P(S)$, obtained for the corresponding linear and nonlinear regimes and also given in Fig. 4.4. While the distribution of slopes is symmetric for times dominated by the linear term in Eq. (4.3), the histogram becomes non-symmetric in the nonlinear regime, large positive slopes being much more frequent than before due to the abrupt jumps in the ϕ values that appear, see Fig. 4.4(b), reminiscent of deterministic sawthooths. Thus, we believe that the asymptotic emergence of the
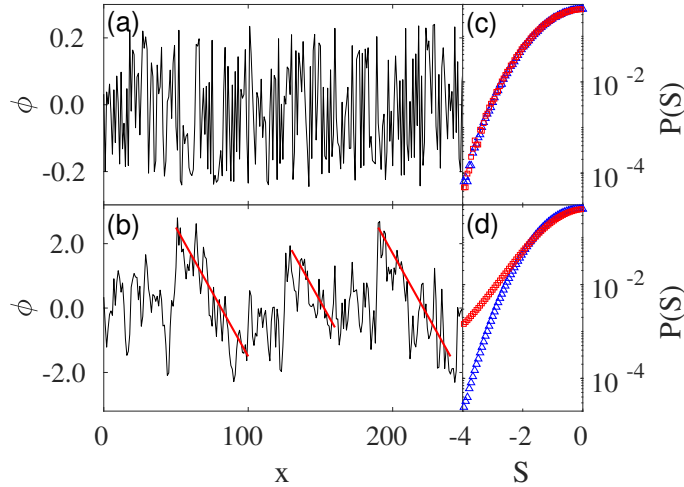
Figure 4.4: *Profiles described by Eq. (4.3) in the linear (a) and nonlinear (b) regimes for parameters as in Fig. 4.1. Parallel straight lines are guides to identify sawtooth-like patches. The slope histogram for time as in (a) [(b)] appears in (c) [(d)], where $S = (\partial_x\phi - \overline{\partial_x\phi})/\mathrm{std}(\partial_x\phi)$ is normalized slope. The $S > 0$ tail (red squares) is reflected to facilitate comparison with the $S < 0$ (blue triangles) data.*

up-down symmetry in Eq. (4.3) can be traced back to the deterministic form of solutions induced by its nonlinearity, this mechanism being also operative in the HK and gHK equations. However, the competition with noise remains far from trivial in these systems, whose solutions, as in the KPZ case [17], differ quite strongly with those of their deterministic counterparts.

4.5   Symmetry emergence in other equations

In order to elucidate the generality of the symmetry emergence in the Burgers equation due to the combined $(x, \phi) \leftrightarrow (-x, -\phi)$ symmetry, we have also studied the kinetic roughening behavior of equations which do also exhibit the combined $(x, \phi) \leftrightarrow (-x, -\phi)$ symmetry while also lacking up-down and left-right symmetries. Specifically, we assess the kinetic roughening of

$$\partial_t\phi = -\nu\partial_x^4\phi + \lambda\partial_x(\phi\partial_x^2\phi) + \eta, \qquad (4.11)$$

where noise correlations are as in Eq. (4.2). We have also integrated numerically additional equations with the same structure as Eq. (4.11) but with nonlinearities
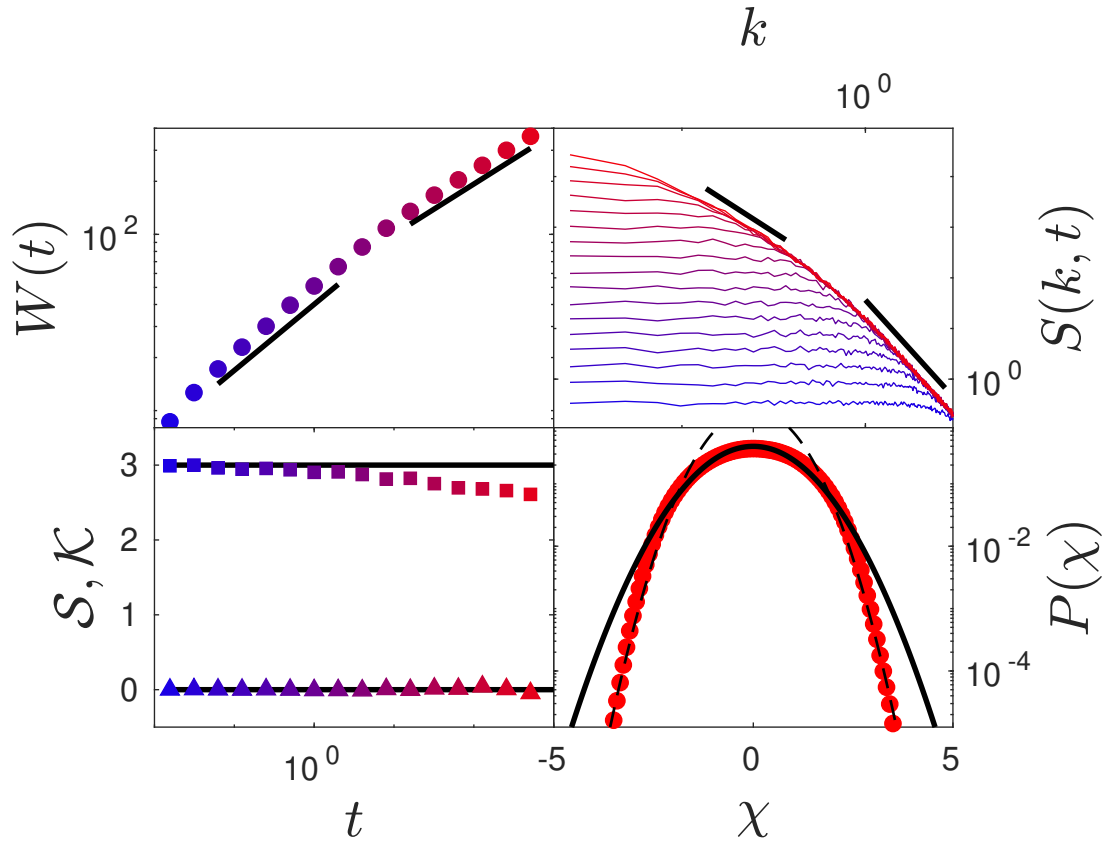
Figure 4.5: *Time evolution of the roughness W (top left panel), structure factor S (top right panel) and skewness and kurtosis of the fluctuations (botton left panel) of numerical solutions of Eq. (4.11). Bottom right panel shows the fluctuation PDF in the nonlinear growth regime. Here $\delta x = 1$, $\delta t = 0.002$, $\lambda = \nu = D = 1$, and $L = 256$. Time increases in all panels from blue to red. Black solid lines are guides to the eye for LMBE $\beta = 3/8$ and expected $\beta = 2/7$ (top left panel), LMBE $-(2\alpha+1) = -4$ and expected $-(2\alpha+1) = -7/3$ (top right panel), Gaussian $\mathcal{S} = 0$ and $\mathcal{K} = 3$ (bottom left panel) and Gaussian PDF (bottom right panel). Dashed line in bottom right panel represents a $\sim e^{-\chi^2}$ decay different from the exact Gaussian that approximately fits the PDF tails.*

of the form $\partial_x(\phi\partial_x\phi)$ and $\partial_x(\phi\partial_x^3\phi)$ leading to unstable solutions. The numerical integration of Eq. (4.11) is done using the same numerical method that was employed for the Burgers equation. We have assessed both the scaling exponents and the fluctuation statistics in order to get a full description of the kinetic roughening behavior for this equation. The scaling exponents fulfill the expected hypescaling $(2\alpha+1 = z$, due to the conserved dynamics and the non-conserved noise) and Galilean $(\alpha+z = 3$, by requesting scale invariance at a non-linear $\lambda \neq 0$ critical point) scaling relations, leading to $\alpha = 2/3$, $z = 7/3$, and $\beta = 2/7$. In Figure 4.5 these values are clearly identified in the evolution of the surface roughness W and structure factor S (see top panels). The linear (LMBE) behavior at short times and small scales, in which the fluctuations are Gaussian, is followed by a nonlinear-dominated regime in which the fluctuations remain symmetric but become non-Gaussian, decaying faster than Gaussian in the tails.

4.6   Conclusions

In summary, we have obtained that, although the asymptotic behavior of the universality class of the Burgers equation with non-conserved noise in $d = 1, 2$ is controlled by nonlinear terms that break the up-down symmetry, the statistics are nonetheless Gaussian. This remains true under strongly-anisotropic perturbations, e.g. by setting $\lambda_y = 0$ in the gHK equation to obtain the HK equation, with different exponents but still Gaussian statistics. This fluctuation behavior allows for exact linear approximations in terms of the kinetic roughening universality class for the asymptotic nonlinear regime of these equations. Our result is in spite of the close relation of Eqs. (4.3) and (4.4) with the KPZ equation, whose statistics are paradigmatically non-symmetric, and contrasts with the non-zero skewness of the NLMBE equation too [30]. We conjecture that the symmetry in the fluctuations, in spite of the up-down lack of symmetry in the equation, is restored by the lack of left-right asymmetry, our argument being reinforced by the behavior of Eq. (4.11), which also exhibits symmetric fluctuations while lacking both up-down and left-right and symmetry. Although in this case the fluctuations are non-Gaussian in spite of being symmetric, we could expect them to converge to Gaussian in the $L \to \infty$ limit if the behavior of the excess kurtosis is analogous of the corresponding one for the Burgers equation $(\mathcal{K}_e \to 0$ when $L \to \infty)$ as derived from our DRG analysis.

Overall, Gaussian statistics can hence emerge for suitable systems whose bare interactions break the symmetries that might be naively associated with the former, at least when they are broken as in the KPZ case. We hope that our results may aid

in the challenge of fully understanding the role of symmetries in the fluctuations of spatially-extended systems far from equilibrium.

Chapter 5

Non-KPZ fluctuations in the derivative of the KPZ equation

5.1 Introduction

5.1.1 The stochastic Burgers equation (conserved noise)

In Chapter 4 we showed how the stochastic Burgers equation with non-conserved noise can be derived as a ultra-low surface tension limit of the stochastic Kuramoto-Sivashinsky (KS) equation in the context of a thin fluid film falling down on an inclined substrate which is disordered and subject to random vibrations. The KS equation with additive *conserved* noise can be also derived when the sources of noise are thermal fluctuations, instead of mechanical vibrations of the wall (see full details about this derivation in Chapter 6). In such a case, the viscous ultra-low surface tension limit leads to the noisy Burgers equation with *conserved* noise,

$$\partial_t u = \nu \partial_x^2 u + \lambda u \partial_x u + \partial_x \eta, \tag{5.1}$$

where η is zero-mean, uncorrelated white noise [see Eq. (4.2)]. Equation (5.1) is frequently known as the noisy Burgers equation [97, 98, 99], and it is a paramount system not only for fluids [100] but also for e.g. plasma turbulence [101], interacting particle systems [102], and driven-diffusive systems [88].

5.1.2 Universality class: KPZ vs Burgers

Under the $u = \partial_x h$ transformation, Eq. (5.1) can be obtained as the derivative of the Kardar-Parisi-Zhang (KPZ) equation for 1D spatial domains. This relation was

69

exploited e.g. in [17] to seminally obtain the exact scaling exponents of Eq. (5.1) by adapting the earlier dynamical renormalization group (DRG) analysis [52] of the equation as a model of a randomly stirred fluid. Both, the noisy Burgers and the KPZ equations share the non-trivial $z = 3/2$ value for the dynamic exponent describing the power-law increase of the correlation length, $\xi(t) \sim t^{1/z}$ [11]. The roughness exponent α quantifying the scaling of the field roughness with system size at saturation [11], differs as expected ($\alpha_{\mathrm{KPZ}} = \alpha_{\mathrm{Burgers}} + 1 = 1/2$), since $h(x) = \int_0^x u(x')\, \mathrm{d}x'$. Thus, the KPZ equation and Eq. (5.1) are frequently considered as two equivalent descriptions of a same underlying process.

A key element determining the universality class of kinetic roughening is the statistics of the field. Both 1D equations, KPZ [40, 11] and Eq. (5.1) [102], share an "accidental" fluctuation-dissipation symmetry by which the nonlinear term does not influence the corresponding stationary solution of the Fokker-Planck equation governing the field PDF, P, which becomes a Gaussian, equilibrium-like distribution, determined by the linear and the noise terms only [40, 102, 11]. However, the KPZ equation shows that Gaussian behavior for the stationary P does *not* imply that the height statistics prior to saturation (for $L < \infty$) are also Gaussian; indeed, as discussed in Chapter 1, they have been proven to be described, depending on global constraints on system size L and/or initial conditions, by some member of the Tracy-Widom (TW) family of probability distribution functions (PDF) for the largest eigenvalue of random matrices [31, 18, 33], demonstrating KPZ behavior as a conspicuous instance among systems with non-Gaussian fluctuations [103].

From the point of view of the specific physical systems described by the noisy Burgers equation [88, 100, 101, 102], it is crucial to clarify whether their field statistics are also non-Gaussian in the growth regime, in order to accurately identify the universality class of their kinetic roughening behavior. In this Chapter we show that this is not the case, i.e., we show that the one-point PDF for $u(x,t)$ as described by Eq. (5.1) is Gaussian for times dominated by the nonlinearity, crucially prior-to and (as expected) after saturation to steady state. We reach this conclusion by direct numerical simulations of the equation, which are analytically supported by a DRG analysis of the field statistics for Eq. (5.1). We also address the dynamics of the space-integral of Eq. (5.1), explicitly illustrating that, in this case, the KPZ sum, $h(x,t)$, of (correlated) Gaussian Burgers variables $u(x,t)$ indeed yields TW statistics [104].
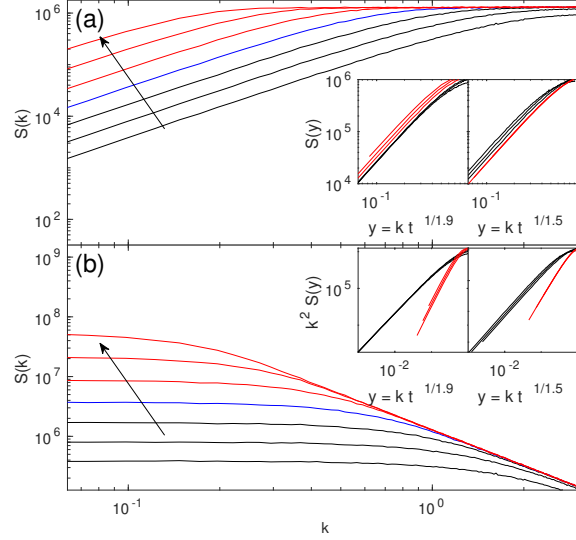
Figure 5.1: Time evolution of the structure factor described by Eq. (5.1) for (a) $u(x,t)$ and (b) $h(x,t) = \int_0^x u(x',t)\, dx'$, using $D = \nu = 1$, $\lambda = 4$, and $L = 256$. Black (red) solid line corresponds to the linear (nonlinear) regime, as implied by the data collapses in the insets. The arrows indicate time increase, with t for each line being twice that of the previous one, starting at $t_0 = 0.64$. All units are arbitrary.

5.2   Universality class of the derivative of the KPZ equation

5.2.1   Scaling exponents

We begin by addressing the full time dynamics described by Eq. (5.1). While the invariant measure of the equation has been shown [102, 97, 98] to be Gaussian, and the asymptotic scaling exponents are analytically known via DRG [52, 105], to our knowledge the time crossover which occurs from linear to nonlinear behavior has not been explicitly addressed yet. In order to assess it, we have performed numerical simulations of Eq. (5.1). Note, this model is known to be conspicuously prone to numerical instabilities [71]. We use the numerical scheme proposed in [72], which provides consistent results. We consider flat initial conditions and periodic boundary conditions.

Figure 5.1 shows the time evolution of the structure factor $S(k,t) = \langle |\tilde{\phi}(k,t)|^2 \rangle$, as described by Eq. (5.1). Panel (a) corresponds to $\phi(x,t) = u(x,t)$, while panel (b)

is for its space integral, $\phi(x,t) = h(x,t) = \int_0^x u(x',t)\,dx'$, which should retrieve the behavior expected for the KPZ equation. At relatively early times, the linear term and the noise in Eq. (5.1) are expected to control the evolution of both the u and h fields, hence $z = 2$ as provided by the exact solution of the linearized equation [11]. This behavior is approximately reproduced by our simulations, as implied by the data collapses shown in the insets for small times. Collapse is achieved for $u(h)$ using $\alpha = -1/2$ $(1/2)$, as also borne out from the exact solution of the linearized equations (5.1) and KPZ, respectively. However, for sufficiently long times, the value of z changes, indicating nonlinear behavior. Indeed, data collapse is now obtained using $z = 3/2$ both, for u and for h, as expected in the asymptotic limit [52, 17]. Note that, also in both cases, α remains fixed to its linear-regime value as a consequence of the mentioned "accidental" fluctuation-dissipation symmetry [102, 11, 40]. Overall, Eq. (5.1) is thus seen to account for the full dynamics of the Burgers field, and for the KPZ behavior of its space integral. Conversely, in Section 5.3 we integrate numerically the KPZ equation showing that the evolution of its slope field $u(x,t) = \partial_x h(x,t)$ coincides with results from Eq. (5.1). All this supports the consistency of our numerical results.

5.2.2   Fluctuation statistics

One-point statistics

Beyond scaling exponents, we have also studied numerically the field statistics described by Eq. (5.1), by considering fluctuations X as defined in Eq. (1.46). We assess in Fig. 5.2 the histogram of $X(x, \Delta t, t_0)$ for the u and h fields, as numerically obtained from Eq. (5.1). Full PDFs are shown in Figs. 5.2(a) and 5.2(b) for times both in the nonlinear growth regime determined above ($t_0 + \Delta t < t_{sat}$, blue empty symbols) and after saturation to steady state ($t_0 > t_{sat}$, red filled symbols). Figures 5.2(c) and 5.2(d) show the time evolution of the field skewness, $\mathcal{S} = \langle X^3 \rangle_c / \langle X^2 \rangle_c^{3/2}$ and excess kurtosis, $\mathcal{K}_e = \langle X^4 \rangle_c / \langle X^2 \rangle_c^2$, respectively. The statistics of $u(x,t)$ are Gaussian to a high precision, both prior to and after saturation, see the PDFs in panels (a,b). Indeed, the skewness and (somewhat more slowly) the excess kurtosis converge rapidly to zero [panels (c,d)] for $u(x,t)$.

In the case of the $h(x,t)$ field, Eq. (5.1) correctly leads $\mathcal{S}(t)$ and $\mathcal{K}_e(t)$ to take on the characteristic universal values of the KPZ equation, either TW-GOE or BR [shown as blue or red solid lines, respectively, in Figs. 5.2(c) and (d)] for intermediate values of Δt within the expected ranges of t_0 and Δt ($t_0 = 0$, $t_{sat} > \Delta t \gg 0$ and $t_0 > t_{sat}$, $t_0 > \Delta t \gg 0$, respectively). Indeed, the PDF of h fluctuations approaches
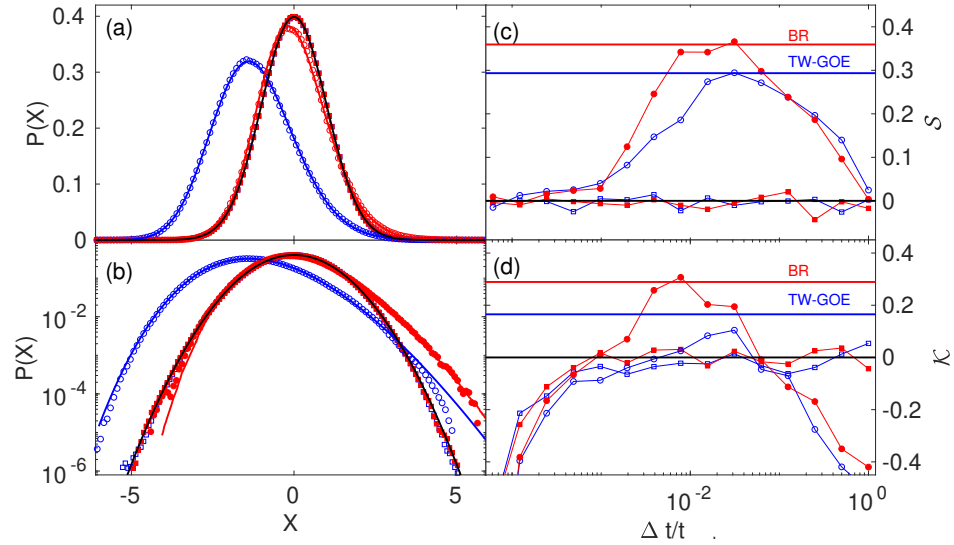
Figure 5.2: Histograms for $X(x, \Delta t, t_0)$ (a,b) from simulations of Eq. (5.1) with $\nu = 1$, $\lambda = 10^3$, $D = 10^{-3}$, and $L = 256$, for $\phi = u$ (squares) and $\phi = h(x, t) = \int_0^x u(x', t)\, \mathrm{d}x'$ (circles). Means and variances have been adjusted to TW-GOE and BR values. Dynamics of skewness (kurtosis) appears in (c) [(d)]. In all panels blue (red) and empty (filled) symbols correspond to the growth (saturation) regime, with black, blue, and red solid lines showing exact Gaussian, TW-GOE, and BR values, respectively; $t_{sat} = 100$, and $\Delta t = 25-50, 1.5-3$, and $0.4-0.8$ are used for Gaussian, TW-GOE, and BR-like histograms, respectively. Thin lines in (c,d) are guides to the eye. All units are arbitrary.

the TW-GOE or BR distributions for $t_0 = 0$ or $t_0 = t_{sat}$, respectively, only for such intermediate values of Δt. This behavior has been also observed for discrete and continuum models in the KPZ universality class [32, 106]. Specifically, the difference between the actual PDF and the ideal TW-GOE or BR distributions reaches a minimum for intermediate values of Δt. It is for such Δt that the numerical h-PDF is plotted in Figs. 5.2(a,b). Means and variances have been adjusted to equal those of the exact TW-GOE or BR distributions. As the pre- or post-saturation h-PDF evolves from Gaussian to TW-GOE or BR, to become Gaussian again for large Δt [see panels 5.2(c,d)], the Gaussian black solid line on panels 5.2(a,b) seems to attract the tails of the h distribution.

The Gaussian behavior numerically obtained for u as described by Eq. (5.1) coincides with analytical expectations derived from a DRG evaluation of the field cumulants. Specifically, we take the same approach taken in Chapter 3 for the scalar Burgers equation with *non*-conserved noise [1], which performs a partial RG transformation only, in which a coarse-graining of the equation is performed, while omitting the standard additional rescaling step [52, 105]. Thus, within a one-loop approximation [80, 81, 82, 83, 1] (see details in Appendix A), $W^2 = \langle u^2 \rangle_c = B \int_{\mathbb{R}} dk_1$, where B is a numerical constant. Considering non-zero lattice spacing, s, and finite L, the variance of u thus scales as $1/L$ for $L \gg s$, which indeed agrees with the expected value of the roughness exponent, $\alpha = -1/2$. Moreover, $W^2 \sim s^{-1}$ for $s \ll 1$ [11, 107]. We have additionally characterized the divergence of the fourth cumulant, $\langle u^4 \rangle_c$, with lattice spacing to determine the asymptotic behavior of the excess kurtosis, $\mathcal{K}_e = \langle u^4 \rangle_c / \langle u^2 \rangle_c^2$. The fourth cumulant of the fluctuation distribution,

$$\langle u^4 \rangle_c = A \int_{\mathbb{R}^{2(n-1)}} G(-k_1 - k_2 - k_3, -\omega_1 - \omega_2 - \omega_3) \times$$
$$(-k_1 - k_2 - k_3) \prod_{i=1}^{3} \frac{dk_i d\omega_i}{(2\pi)^2} k_i G(k_i, \omega_i) k_i^{3/2} \nu^2(k_i) |G(k_i, \omega_i)|^2, \qquad (5.2)$$

where $A = \pi^{n-1/2} i^n \Gamma(n - 1/2) K 2D / [n!(n-1)\lambda^{n-2}]$, has been estimated for different values of the lattice spacing s by using the Monte Carlo integration method described in Chapter 3. Gaussian random variables have been used for $\omega_1, \omega_2, \omega_3$. For the spatial wavenumbers k_1, k_2, k_3, random variables distributed as $\sim k_i^{-1}$ have been chosen in order to enhance the numerical efficiency of the Monte Carlo estimation. Parameters have been chosen so as to make $A = 1$ and $D\lambda^2/2\pi = 1$. Integration limits in k_1, k_2, k_3 of the form $[1, \Lambda]$ have been taken for different values of $\Lambda \propto 1/s$, in order to characterize the divergence of the integral with the lattice spacing s. The conclusion is that $\langle u^4 \rangle_c \sim (\ln \Lambda)^{0.79}$, see Fig. 5.3.

Moreover, as described in Chapter 4 for Burgers equation with *non*-conserved noise, an exact symmetry in reciprocal space induces the exact cancellation of all
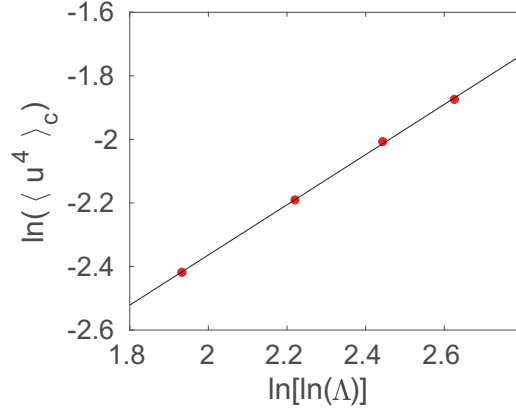
Figure 5.3: Numerical computation of the fourth cumulant in the $[k_1, k_2, k_3] \in [1, \Lambda]^3$ region, for different values of Λ (symbols). The solid line shows a linear fit of the numerical data, and corresponds to the straight line $y = 0.79x - 3.94$, hence $\langle u^4 \rangle_c \sim (\ln \Lambda)^{0.79}$.

odd-order cumulants ($\langle u^n \rangle_c$ for odd n). Hence, the skewness is identically zero and, more generally, the u-PDF is symmetric (as a Gaussian, but unlike the TW distribution [1]). Combined with the vanishing kurtosis, these results fully agree with the Gaussian statistics we have found numerically for the u field.

Covariance

A final difference in the critical behavior of the u (Burgers) and h (KPZ) fields, as described by Eq. (5.1), lies in the behavior of the covariance $C(x, t)$ as defined in Eq. (1.44). The correlations for the h field obtained as the integral of the u field from numerical simulations of Eq. (5.1) have been shown in the description of the KPZ universality class in Chapter 1. Here, the behavior of the u field is depicted in Fig. 5.4. In both cases the expected scaling form holds [8, 11], $C(x, t) = t^{2\beta} c(x/t^{1/z})$ with $c(y) \sim \text{cst.} - y^{2\alpha}$ for $y \ll 1$ and 0 for $y \gg 1$, but the exponents leading to collapse [i.e., those derived from Fig. 5.1] are different, as are the corresponding scaling functions $c(y)$. Hence, *qualitative* differences between Burgers and KPZ behaviors seem larger for the one-point statistics than for $C(x, t)$.

Our simulations of Eq. (5.1) likewise reproduce the expected two-point correlations for h (whose results were also provided in Chapter 1 as illustration for the KPZ fluctuation behavior after saturation) and u *after saturation* to steady state, as shown by studying $G(x, t)$ as in Eq. (1.47) for long times $t_0 > t_{sat}$. For $\phi = u$, one
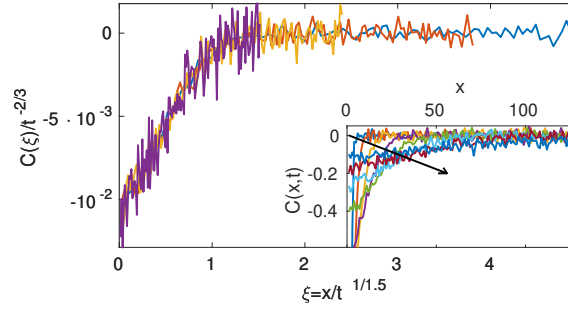
Figure 5.4: Collapse of the covariance function $C(x,t)$ at different times described by Eq. (5.1) for $L = 256$, $\delta t = 10^{-2}$, $\nu = D = 1$, $\lambda = 10$. The inset shows the uncollapsed data. The small range of values for C induces large relative errors. Arrows show time increase, with t doubling for each line, from $t_0 = 1$.
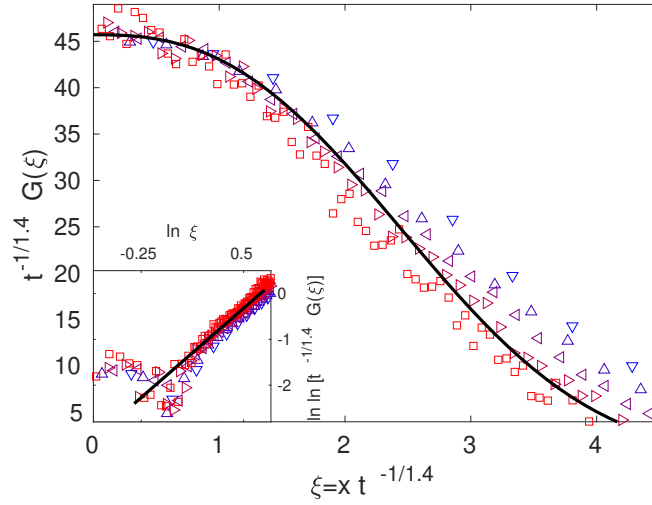
Figure 5.5: Correlation function $G(x,t)$ from numerical simulations of Eq. (5.1) for $L = 2^{10}$, $\delta t = 5 \cdot 10^{-3}$, $\nu = D = 1$, $\lambda = 6$. The black solid line is a fit to $f(\xi) \propto e^{-a_2 \xi^{2.6}}$, and has slope 2.6 in the inset. The exponents required for collapse are close (but not identical) to the theoretical expectations [33, 41, 42]. Color evolves from blue to red for increasing $t > t_{sat}$ between $t = 3$ and $t = 45$. The number of realizations is $2 \cdot 10^4$.

Figure 5.6: *Time evolution of the structure factor of solutions of the Burgers equation with conserved noise (a) and the slopes of the KPZ equation (b), for $D = 1$, $\lambda = 4$, $\nu = 1$, and $L = 256$. Black (red) solid lines correspond to the linear (nonlinear) regime, as implied by the collapse shown in the insets. Time increases following the arrow, t for each line being twice that of the previous one, starting at $t_0 = 0.64$. All units are arbitrary.*

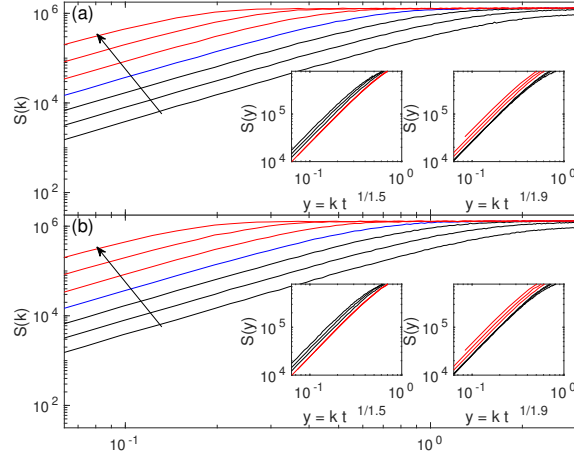expects [41, 42, 33] $C(x,t) \propto t^{1/z} f(a_1 x/t^{1/z})$, for $t_0 > t_{sat}$, where $f(y) \sim e^{-a_2 y^3}$ with $a_{1,2}$ being numerical constants, as approximately obtained in Fig. 5.5.

5.3   Noisy Burgers as the derivative of KPZ

To further assess the relation between Burgers equation with conserved noise Eq. (5.1) and the Kardar-Parisi-Zhang (KPZ) equation, where the former is the space derivative of the latter, here we simulate numerically both, Eq. (5.1) and KPZ, taking the space derivative of the latter for each time and noise realization, compute the structure factor for both numerical fields, and compare the results. Recall that the stochastic nonlinear equations which we are discussing are conspicuously prone to numerical inaccuracies and instabilities [72, 71], which renders nontrivial the present type of check which we are performing. Results are provided in Fig. 5.6, in which panel (a) corresponds to Eq. (5.1) [thus repeating the same data shown in Fig. 5.1 (a) of section 5.2.1 for the reader's convenience] and panel (b) corresponds to the numerical derivative of the KPZ profile described by Eq. (1.42). As expected, results are virtually indistinguishable, hence consistent with the behavior discussed in section 5.2.1 for the Burgers equation with conserved noise, Eq. (5.1), namely,
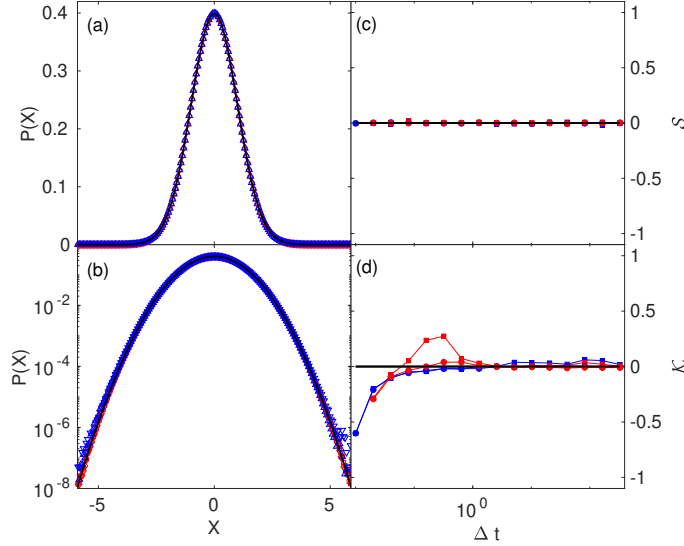
Figure 5.7: *Fluctuation histogram [using X as defined in Eq. (1.46)] for $t_0 = 0$ (blue) and $t_0 = t_{sat} = 300$ (red) and $\Delta t = 150$, from numerical simulations of Burgers equation with conserved noise (squares) and from the derivative (slope field) of numerical simulations of the KPZ equation (circles), using parameters as in Figs. 5.1(a) and (b). The solid lines correspond to a Gaussian distribution. Time evolution of the fluctuations skewness (c) and kurtosis (d) for the same numerical simulations as in panels (a) and (b). All units are arbitrary.*

early-time (linear regime) exponent values $z_{\text{linear}} = 1.9$, $\alpha_{\text{linear}} = -1/2$ and late-time (nonlinear regime) exponent values $z_{\text{nonlinear}} = 3/2$, $\alpha_{\text{nonlinear}} = -1/2$.

We proceed similarly to compute the probability distribution function (PDF) of the field both, for Eq. (5.1) and for the numerical derivative of Eq. (1.42). Results are provided in Fig. 5.7. The histograms have been computed for the same parameter conditions as in Fig. 5.2, both for the same t_0 and Δt values for which Tracy-Widom (TW) and Baik-Rains (BR) distributions are obtained for the h field described by Eq. (5.1) there. The histograms shown in Figs. 5.7(a) and (b) are Gaussian to a high precision, compare the simulation results symbols in the figures with the exact Gaussian forms (solid lines). Also, the skewness and excess kurtosis shown in Figs. 5.2(c) and 5.7(d), respectively, are seen to readily take on their Gaussian (zero) values. All these results support the interpretation of the noisy Burgers equation as the derivative of the KPZ equation, as well as the Gaussian behavior of its fluctuations, both prior and after saturation to steady state, as assessed by our numerical

simulations.

5.4   Exact linear approximation

The Gaussian nature of the field PDF displayed by Eq. (5.1) in its large-scale nonlinear regime allows for an exact Gaussian (asymptotic) approximation of the equation in terms of a *linear* model which is in the same universality class, including scaling exponent values *and* Gaussian statistics. Again, this is akin to the case of the scalar Burgers equation with non-conserved noise (see Chapter 4), also including higher-dimensional and strongly anisotropic generalizations [15, 55], like the celebrated Hwa-Kardar equation for the height of a running sand pile [56]. In contrast with these cases, Eq. (5.1) does *not* support hyperscaling ($2\alpha + d = z$) [11, 8], hence noise correlations are required in order to match the full universal behavior. Specifically, the linear, non-local equation

$$\partial_t \tilde{u}(k,t) = -|k|^{3/2}\tilde{u}(k,t) + \tilde{\eta}(k,t), \tag{5.3}$$

$$\langle \tilde{\eta}(k,t)\tilde{\eta}(k',t') \rangle = |k|^{3/2}\delta(k+k')\delta(t-t'), \tag{5.4}$$

yields the exact same asymptotic behavior of the nonlinear Eq. (5.1). Note that a similar exact Gaussian approximation is not possible for systems with non-Gaussian statistics (like the KPZ equation), not even considering correlations in the noise.

5.5   Symmetry discussion

Our numerical and analytical results indicate that the long-time behavior of Burgers equation with conserved noise, Eq. (5.1), albeit controlled by the nonlinear term, displays Gaussian statistics. This is in spite of the fact that it is precisely such a nonlinear term which breaks the reflection symmetry ($u \leftrightarrow -u$) of the equation. As noted Chapter 1, this lack of symmetry has been correlated in the KPZ [11] and nonlinear-MBE equations [30] with a non-zero skewness due to the existence of a preferred growth direction [8]. Hence, the symmetry of the (Gaussian) PDF is again an emergent property of the large-scale behavior in Eq. (5.1), much as it is for Burgers equation with *non-conserved* noise (see Chapter 4). Akin to the latter, the symmetric field PDF in the nonlinear regime can be related with the behavior of the deterministic (viscous) Burgers equation, which is analytically known [95, 96] to yield sawtooth profiles, symmetric, as Eq. (5.1), under a combined $(x,u) \leftrightarrow (-x,-u)$ transformation. This nonlinear behavior can be specifically assessed in the slopes
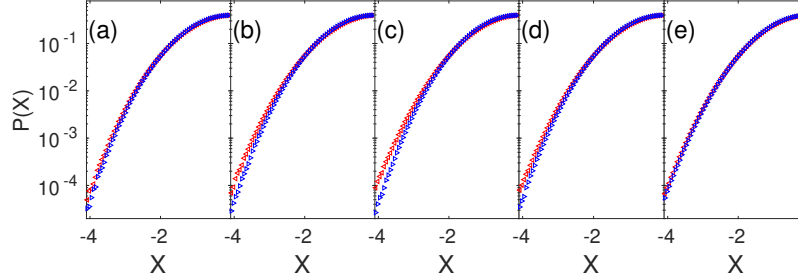
Figure 5.8: Histogram for the slope field $\phi = \partial_x u$ [using $X = (\phi - \bar{\phi})/\text{std}(\phi)$] from numerical simulations of Eq. (5.1) for $\nu = 1$, $\lambda = 10^4$, $D = 10^{-3}$, and $L = 256$, for times in the linear (a), nonlinear (b), (c), (d), and saturation (e) regimes [time for each panel is twice that of the previous one, starting at $t_0 = 40$ (a)]. The $X > 0$ data (red left triangles) have been reflected to facilitate comparison with $X < 0$ data (blue right triangles). All units are arbitrary.

histogram, again as in Burgers equation with non-conserved noise [108] (see Chapter 4), being enhanced for large λ and small ν and D values.

In order to assess this phenomenon and in analogy with the simulations provided in Figs. 5.2 and 5.6, we assess the relevance of sawtooth-like features in the long-time behavior of the noisy Burgers equation, by evaluating the fluctuation histogram for both *(i)* the slopes of the u field from the solutions of the Burgers equation with conserved noise and *(ii)* the second-order space derivative (curvature field) of the h field from the solutions of the KPZ equation. As expected, in both cases the profiles are asymmetric for intermediate times within the nonlinear regime [Figs. 5.8 and 5.9 (b)-(d)], away both from the linear [Figs. 5.8 (a) and 5.9 (a)] and from the saturation [Figs. 5.8 (e) and 5.9 (e)] regimes, in which the surface is $x \leftrightarrow -x$ symmetric on average.

5.6   Behavior in higher dimensions

It is natural to consider if non-KPZ behavior also occurs for the Burgers equation with conserved noise in higher dimensions. E.g. in 2D, note that, if the equation is to be for a scalar field, it can no longer be the derivative of the KPZ equation, as this is a vector field. Nevertheless, a scalar 2D generalization of Eq. (5.1) can still be formulated in close analogy with the case of non-conserved noise (generalized
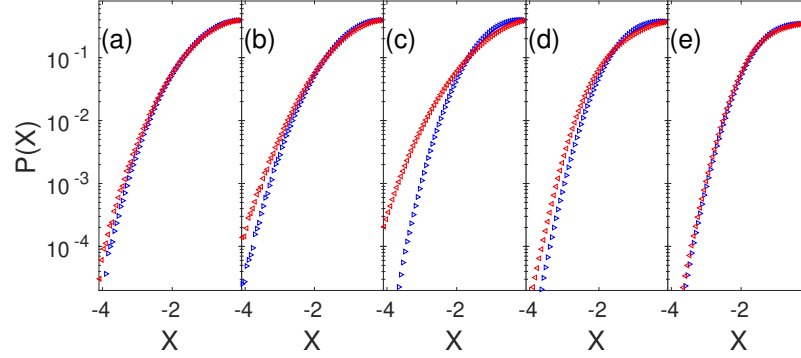
Figure 5.9: *Fluctuation histogram from numerical simulations of the curvature field (second-order space derivative) from numerical simulations of the KPZ equation, for times in the linear (a), nonlinear (b-d), and saturation (e) regimes (time for each panel is twice that of the previous one, starting at $t_0 = 40$). The histogram for $X > 0$ (red left triangles) has been reflected to facilitate comparison with the $X < 0$ (blue right triangles) data. Parameters as in Fig. 5.1, except for $\lambda = 10^4$ and $D = 10^{-3}$. All units are arbitrary.*

Hwa-Kardar Eq. (4.4), see Chapter 4), which reads

$$\partial_t u = \nu \ \nabla^2 u + \lambda u(\partial_x u + \partial_y u) + \partial_x \eta_x + \partial_y \eta_y, \tag{5.5}$$

$$\langle \eta_i(\mathbf{r}_1, t_1)\eta_j(\mathbf{r}_2, t_2) \rangle = 2D\delta_{ij}\delta(\mathbf{r}_1 - \mathbf{r}_2)\delta(t_1 - t_2), \ \ i, j = x, y. \tag{5.6}$$

Numerical simulations have been carried out of Eq. (5.5). Our numerical simulations employ the same pseudospectral numerical scheme which has been employed for Eq. (5.1). The evolution of the structure factor $S(k, t) = S(k_x, 0, t) = S(0, k_y, t)$ [55] is shown in Fig. 5.10. For increasing time and as in 1D, $S(k, t)$ again converges towards k-independent (i.e., white noise) behavior except for the largest values of k, due to the limited accuracy of the numerical scheme at small scales. Note the small range of values that actually occur for $S(k, t)$, leading to large relative numerical errors, which are specially large at such small scales. Data collapse is achieved for $\alpha = -1/2$ and $z = 3/2$, notably the same numerical values as in 1D, i.e., for Eq. (5.1).

The one-point statistics of the u field has been also numerically characterized for Eq. (5.5). The time evolution of the skewness and excess kurtosis, as well as the histograms for X as defined in Eq. (1.46), are plotted in Fig. 5.11, both in the growth regime and after saturation to steady state. The large impact of numerical errors for these data, related with the limited range of values of the structure factor (see
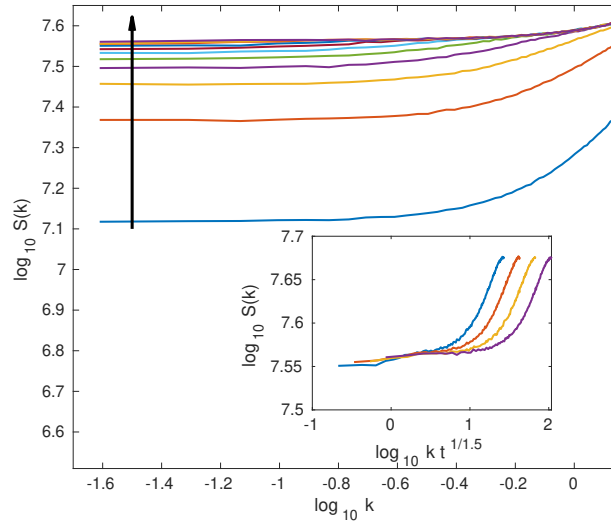
Figure 5.10: *Time evolution of the structure factor $S(k) = S(k_x, 0) = S(0, k_y)$ for the gHK equation with conserved noise, Eq. (5.5). Time increases in the direction of the arrow, doubling for each consecutive live starting at $t_0 = 1$. The inset shows collapsed $k^{2\alpha+1}S(kt^{1/z})$ curves for the longest times within the nonlinear regime, using exponent values $\alpha = -1/2$ and $z = 3/2$. Here, $L_x = L_y = 256$, $\delta x = \delta y = 1$, $\delta t = 0.01$, and $\nu = D = \lambda = 1$.*
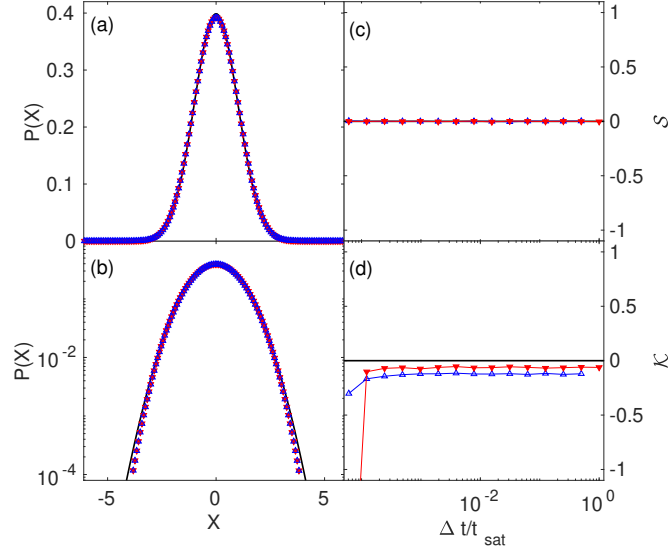
Figure 5.11: Histogram for $X(x, \Delta t, t_0)$ (with $\phi = u$) (a,b) from simulations of Eq. (5.5) with $\nu = D = \lambda = 1$, and $L_x = L_y = 1024$. In all panels blue up (red down) and empty (filled) triangles correspond to the growth (saturation) regime, with black solid lines showing exact Gaussian values; $t_{sat} = 64$, and $\delta t = 0.1$ are used. All units are arbitrary.

also Fig. 5.10), seems to induce a slightly negative excess kurtosis. Nevertheless, the variations in u show a symmetric PDF and behave not far from a Gaussian random variable, thus again a non-KPZ universality class in 2D [18, 33].

5.7   Conclusions

In summary, we have obtained that the field statistics of the Burgers equation with conserved noise are Gaussian, in spite of the facts that its asymptotic behavior is controlled by a nonlinear term which explicitly breaks the up-down symmetry and that the equation is related to KPZ through a mere space derivative. Such non-symmetric statistics indeed occurs both, for the integral and the slope fields related with the u field described by Eq. (5.1). In particular, all this behavior provides a nontrivial example in which the KPZ sum, $h(x,t) = \int_0^x u(x', t)\, dx'$, of (correlated) Gaussian Burgers variables u yields non-Gaussian KPZ variables h. Albeit counterintuitive, this effect is not unknown; there are known cases of sums of (even uncorrelated)

Gaussian variables which turn out not to be Gaussian themselves. For instance [109], if we consider a 2D random vector $X = (X_1, X_2) = (Z_1, \text{sign}(Z_1)|Z_2|)$, where Z_1 and Z_2 are independent Gaussian random variables, by construction both X_1 and X_2 are normally distributed but their realizations are always either both negative or both non-negative, hence the random variable $Y = X_1 + X_2$ is not Gaussian.

We have also provided novel data for the correct identification of the universality class (including scaling exponent values and field PDF) of the stochastic Burgers equation, which plays a relevant role as a physical model in the many contexts of spatially-extended systems, from fluid turbulence to driven diffusive systems.

Chapter 6

Transition between chaotic and stochastic universality subclasses

6.1 Introduction

6.1.1 Universality subclasses in the stochastic KS equation

As described in Chapter 1, while keeping the same values of the scaling exponents, universality *subclasses* exist in the 1D KPZ class, which differ by the flavor of the precise TW PDF which occurs: indeed, finite systems whose size (does not) increase linearly with time display largest-eigenvalue distribution of random matrices in the Gaussian Unitary Ensemble GUE (Gaussian Orthogonal Ensemble GOE) statistics [110, 111, 112]. Transitions between different subclasses have been also assessed for changes in the background topology [113] or in the rate of system-size change [114]. Furthermore, the existence of universality subclasses induced by similar changes in geometrical constraints carries over to the main linear [115] and nonlinear [30] universality classes of kinetic roughening other than KPZ. In all these cases, the universality subclasses sharing scaling exponent values differ by some global geometrical or topological condition on the system size or background metric; hence the existence of alternative mechanisms which may likewise control the field PDF remains uncertain. In this Chapter, we will provide an example of a novel mechanism inducing transitions between universality subclasses in the context of the Kuramoto-Sivashinsky (KS) equation.

Specifically, we begin by showing below that the kinetic roughening behavior of

the stochastic Kuramoto-Sivashinsky equation with conserved noise

$$\partial_t u = -\nu_0 \partial_x^2 u - \kappa_0 \partial_x^4 u + \lambda_0 u \partial_x u + \tilde{D}_0 \partial_x \eta, \tag{6.1}$$

is characterized by critical exponent values which are shared by its deterministic limit $\tilde{D} = 0$. The large-scale behavior of the deterministic KS equation is known to remarkably coincide [51, 116] in terms of scaling exponents with that of the stochastic Burgers equation, whose kinetic roughening exponents and field PDF have been studied in Chapter 5. However, we will show that the field PDF for the KS equation is non-Gaussian (Gaussian) for low (large) noise values, corresponding to dynamics dominated by chaotic (stochastic) fluctuations. This transition in the universality class occurs at a non-zero noise amplitude $\tilde{D}_0$ and might be observable in suitable experimental contexts.

On the other hand, the deterministic ($D_0 = 0$) [117, 118], as well as the stochastic ($D_0 \neq 0$) KS equations for $h = \int_0^x u \, dx'$ [119, 105]

$$\partial_t h = -\nu_0 \partial_x^2 h - \kappa_0 \partial_x^4 h + \frac{\lambda_0}{2}(\partial_x h)^2 + D_0 \eta, \tag{6.2}$$

namely the KS-KPZ equations, are both in the KPZ universality class. However, how and if the nature of the fluctuations, whether deterministic chaos or stochastic noise, reflects into the kinetic roughening behavior, has remained overlooked thus far. We will show for Eq. (6.2) that the field PDF follows the same TW-GOE distribution in both cases, in spite of the fact that a similar chaotic-stochastic dominated fluctuations transition occurs analogous to that in Eq. (6.1).

6.1.2   KS equation with conserved noise as a physical model

While the Kuramoto-Sivashinsy equation, Eq. (6.1), has been derived as a physical model in many different contexts, either in the deterministic case (see the full derivation as an interface equation for a thin fluid film falling down a slope in Chapter 2) or subject to non-conserved noise [49], there does not seem to be an analogous explicit derivation in which the equation comes out perturbed by conserved noise as in Eq. (6.1). In this section we provide one such derivation for a liquid film falling down an inclined plane (see Fig. 2.1 in Chapter 2), which is assumed to be so thin (*ultrathin*) that thermal fluctuations and disjoining pressure can no longer be neglected [61, 59].

We implement thermal fluctuations in the stress tensor as done in Chapter 2 following classical stochastic hydrodynamics [59], namely, we write

$$\mathcal{T} = \mathcal{T}^f + S = \mathcal{T}^f + \begin{pmatrix} S^{xx} & S^{xy} \\ S^{yx} & S^{yy} \end{pmatrix}, \tag{6.3}$$

where $\mathcal{T}^f$ is the fluidic stress tensor as in (2.7) and S^{ij} are the components of a symmetric, zero-mean, delta-correlated fluctuation tensor S as in Chapter 2. The balance of linear momentum takes the form

$$\rho(u_t + u\ u_x + v\ u_y) = \mu(u_{xx} + u_{yy}) - p_x + \rho\ g\ \sin\theta + S_x^{xx} + S_y^{xy}, \qquad (6.4)$$

$$\rho(v_t + u\ v_x + v\ v_y) = \mu(v_{xx} + v_{yy}) - p_y - \rho\ g\ \cos\theta + S_x^{yx} + S_y^{yy}, \qquad (6.5)$$

where subindices denote partial derivatives.

Now, analogously with the procedure described in Chapter 2 in the derivation of the deterministic KS equation, we take the average thickness, h_0, of the liquid layer as a typical length scale, $w_0 = \rho g h_0^2 \sin\theta/2\mu$ as a velocity scale, w_0/h_0 as a time scale, and $\mu w_0/h_0$ as a representative scale for pressure and stress, and introduce a small parameter ϵ and the new variables $x' = \epsilon x$, $t' = \epsilon t$, and $v' = v/\epsilon$, adapted to a lubrication approximation [49] within which the cross-stream dimension of the film will be considered much smaller than its streamwise extent. We consider the capillary number, $\mathrm{Ca} = \mu w_0/\gamma$, to be order ϵ^2 and define $\mathrm{Ca}' = \mathrm{Ca}/\epsilon^2$. We expand $u = u_0 + \epsilon u_1 + \mathcal{O}(\epsilon^2)$, $v' = v_0' + \epsilon v_1' + \mathcal{O}(\epsilon^2)$, and $p = p_0 + \epsilon p_1 + \mathcal{O}(\epsilon^2)$, and consider S^{xx}, S^{yy} to be $\mathcal{O}(\epsilon^{-2})$ and S^{xy}, S^{yx} to be $\mathcal{O}(\epsilon^{-1})$ [59]. Last, by defining $S^{xx\prime} = S^{xx}/\epsilon^2$, $S^{yy\prime} = S^{yy}/\epsilon^2$, $S^{xy\prime} = S^{xy}/\epsilon$, and $S^{yx\prime} = S^{yx}/\epsilon$, the momentum balance equations (6.4) and (6.5) and the surface boundary conditions

$$||\vec{n}\ (\mathcal{T} + \Pi\,\mathbb{I})\ \vec{n}|| = \gamma\mathcal{C}, \qquad ||\vec{n}\ (\mathcal{T} + \Pi\,\mathbb{I})\ \vec{t}|| = 0 \qquad (6.6)$$

become, respectively,

$$\mathrm{Re}\ \epsilon(u_t + u\ u_x + v\ u_y) = \epsilon^2 u_{xx} + u_{yy} - \epsilon p_x + 2 + \epsilon^3 S_x^{xx} + \epsilon S_y^{xy}, \qquad (6.7)$$

$$\mathrm{Re}\ \epsilon^2(v_t + u\ v_x + v\ v_y) = \epsilon^3 v_{xx} + \epsilon v_{yy} - p_y - 2\cot\theta + \epsilon^2 S_x^{yx} + \epsilon^2 S_y^{yy}, \qquad (6.8)$$

$$p + \Pi = \epsilon\frac{\epsilon h_x^2(2\epsilon u_x + \epsilon^2 S^{xx}) - h_x[2(u_y + \epsilon^2 v_x] + 2\epsilon S^{xy}) + 2v_y + \epsilon S^{yy}}{1 + \epsilon^2 h_x^2} - \frac{1}{\mathrm{Ca}'}h_{xx}, \quad (6.9)$$

$$0 = -\epsilon^2 h_x^2(u_y + \epsilon^2 v_x + \epsilon S^{xy}) + \epsilon^2 h_x[\epsilon(S^{yy} - S^{xx}) + 2(v_y - u_x)] + u_y + \epsilon^2 v_x + S^{yx}, \quad (6.10)$$

where primes have been dropped.

We compute the velocity profile $u = u_0 + \epsilon u_1 + \mathcal{O}(\epsilon^2)$. At $\mathcal{O}(1)$, Eq. (6.7) becomes $u_{0yy} = -2$. As $u_{0y} = 0$ at the fluid surface $y = h$ [leading order of Eq. (6.10)] and $u_0 = 0$ at the substrate $y = 0$, we obtain $u_0 = 2\,(hy - y^2/2)$. Considering the fluid film to be ultrathin, $\mathrm{Re} \ll 1$ can be neglected, and Eq. (6.8) at $\mathcal{O}(\epsilon)$ becomes $u_{1yy} = p_{0x} - S_y^{xy}$. Here we have $u_{1y} = -S^{yx}$ [Eq. (6.10) at $\mathcal{O}(\epsilon)$] and $u_1 = 0$ as

boundary conditions at the fluid surface and the substrate, respectively, which allow us to obtain the profile for $u_1 = -p_{0x}(hy - y^2/2) - \int_0^y S^{yx} dy$. The p_0 contribution can be obtained from Eq. (6.7) at $\mathcal{O}(1)$, $p_{0y} = -2 \cot \theta$, with $p_0 = -\Pi - h_{xx}/\mathrm{Ca}'$ as boundary condition at the fluid surface, obtaining $p_0 = 2 \cot \theta (h - y) - \Pi - h_{xx}/\mathrm{Ca}'$.

Finally, mass conservation reads $h_t + \left(\int_0^h u_0 + \epsilon \, u_1 dy \right)_x = 0$. Using that $\int_0^h u_0 \, dy = 2h^3/3$ and

$$\int_0^h u_1 \, dy = -\frac{h^3}{3} p_{0x} =$$

$$= -\frac{h^3}{3} \left(2 \cot \theta \, h_x - \Pi_x - \frac{1}{\mathrm{Ca}'} h_{xxx} \right) + \int_0^y \int_0^{y'} S^{yx} \, dy' \, dy, \qquad (6.11)$$

the evolution equation becomes

$$h_t + \left(\frac{2}{3} h^3 + \epsilon \frac{h^3}{3} \left(-2 \cot \theta \, h_x + \Pi_x + \frac{h_{xxx}}{\mathrm{Ca}'} \right) + \epsilon \int_0^y \int_0^{y'} S^{yx} \, dy' \, dy \right)_{x'} = 0. \quad (6.12)$$

Substituting $\int_0^y \int_0^{y'} S^{yx} \, dy' \, dy$ by $(\mu k_B T h^3/3)^{1/2} \eta$, where k_B is the Boltzman constant, T is the temperature and η is zero average, Gaussian white noise [59] (see Chapter 2 for additional details) and $\Pi = -\phi_y$, where ϕ is the interface potential [58], we finally obtain

$$h_t + \left(\frac{2}{3} h^3 + \epsilon \frac{h^3}{3} \left(-2 \cot \theta \, h_x - \phi_{yx} + \frac{1}{\mathrm{Ca}'} h_{xxx} \right) + \epsilon \sqrt{\frac{\mu k_B T h^3}{3}} \eta \right)_x = 0. \quad (6.13)$$

A weakly-nonlinear expansion allows us to obtain the KS equation with conserved noise from Eq. (6.13). Considering very small fluctuations around the flat film solution, $h = 1 + \epsilon \tilde{h}$, Eq. (6.13) becomes

$$0 = \epsilon \tilde{h}_t + \left([1 + 3\epsilon \tilde{h} + 3\epsilon^2 \tilde{h}^2 + \mathcal{O}(\epsilon^3)] \left(\frac{2}{3} + \frac{\epsilon}{3} P_x \right) + \epsilon \sqrt{\mu k_B T \frac{1 + \mathcal{O}(\epsilon)}{3}} \eta \right)_x, \quad (6.14)$$

where

$$P_x = \epsilon \left[-2 \cot \theta \, \tilde{h}_x + \frac{1}{\mathrm{Ca}'} \tilde{h}_{xxx} - \phi_{yy}(1 + \epsilon \tilde{h}) \right]. \qquad (6.15)$$

If we linearize $\phi'(1 + \epsilon \tilde{h}) \simeq \phi_y(1) + \phi_{yy}(1)\epsilon \tilde{h}$, expand $(\tilde{h}^2)_x = 2\tilde{h}\tilde{h}_x$, and consider the change of variable $z = x - 2t$ and $\tau = \epsilon t$ (thus $\partial_t = -3\partial_z + \epsilon \partial_\tau$ and $\partial_x = \partial_z$), Eq.

(6.14) becomes

$$\tilde{h}_\tau + 4\tilde{h}\tilde{h}_z - \frac{2}{3}\cot\theta\ \tilde{h}_{zz} + \frac{1}{3\mathrm{Ca'}}\tilde{h}_{zzzz} + \phi_{yy}(1)\tilde{h}_{zz} + \frac{1}{\epsilon}\sqrt{\frac{\mu k_B T}{3}}\eta_z = 0. \qquad (6.16)$$

Finally, by defining $\kappa_0 = 1/(3\mathrm{Ca'})$, $\nu_0 = \phi_{yy}(1) - 2\cot\theta/3$, and $\tilde{\eta} = \eta/\epsilon$,

$$\tilde{h}_\tau + \nu_0\tilde{h}_{zz} + \kappa_0\tilde{h}_{zzzz} + 4\tilde{h}\tilde{h}_z + \sqrt{\frac{\mu k_B T}{3}}\tilde{\eta}_z = 0, \qquad (6.17)$$

which is a particular case of the general stochastic KS equation (6.1) after coordinates and fields are renamed as $(z, \tau, \tilde{h}, \tilde{\eta}) \to (x, t, u, \eta)$, with $D_0 = 0$, $\tilde{D}_0 = \sqrt{\frac{\mu k_B T}{3}}$, and $\lambda_0 = -4$.

6.2 Universality class of the KS equation

In this section we investigate in full detail the universality class of Eq. (6.1) for the deterministic case, as well as for the stochastic cases with conserved noise, Eq. (6.1), and also with non-conserved noise, namely,

$$\partial_t u = -\nu_0\partial_x^2 u - \kappa_0\partial_x^4 u + \lambda_0 u\partial_x u + D_0\eta, \qquad (6.18)$$

for which the eventual presence of additional sources of conserved noise, whose strength is $\propto k^2$ in Fourier space, are irrelevant at large scales ($k \ll 1$).

As similar argument to the seminal one by Yakhot [51] leads one to expect Eqs. (6.1) and (6.18) to renormalize at large scales into an effective stochastic Burgers equation,

$$\partial_t u = \nu\partial_x^2 u + \lambda u\partial_x u + (D + \tilde{D}\partial_x)\eta, \qquad (6.19)$$

where notably $\nu > 0$, rendering asymptotically irrelevant the biharmonic term in Eqs. (6.1) and/or (6.18). Moreover, the noise in the effective equation, Eq. (6.19), respects the conservation law expressed by either Eq. (6.1) or Eq. (6.18). I.e., if the bare equation is deterministic or has conserved noise, then $D = 0$, $\tilde{D} \neq 0$, while if the bare noise is non-conserved, so is the effective noise, thus $D \neq 0$, $\tilde{D} = 0$.

6.2.1 Scaling exponents

We have performed numerical simulations of Eq. (6.1) using the implementation of the pseudospectral method described in Chapter 3 and periodic boundary conditions
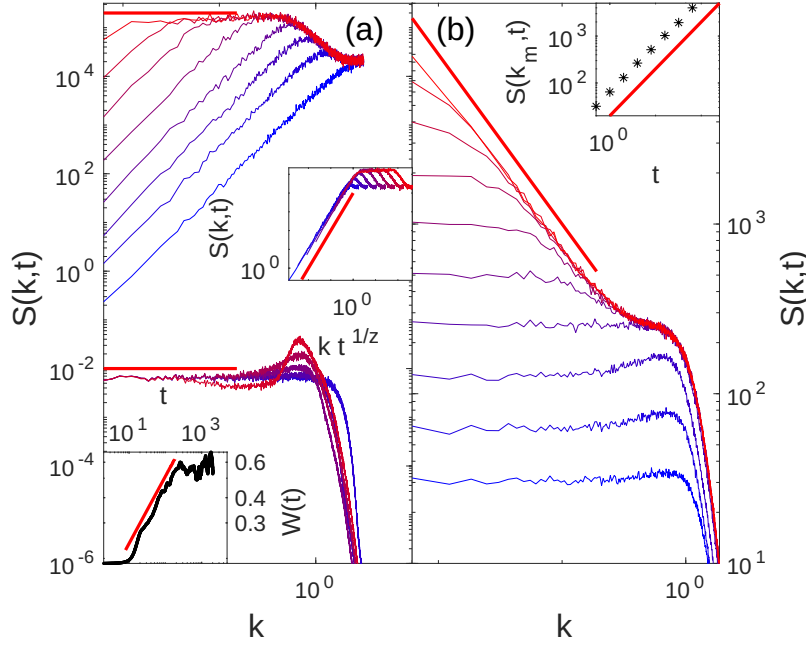
Figure 6.1: *Time evolution of $S(k,t)$ from numerical simulations of Eq. (6.1) for different noise conditions: (a) deterministic case ($D_0 = \tilde{D}_0 = 0$; bottom) and conserved-noise ($D_0 = 0, \tilde{D}_0 = 1$; top). Top inset: data collapse for $\alpha_{cn} = -1/2, z_{cn} = 3/2$. Bottom inset: time evolution of the roughness of $h(x,t) = \int_0^x u(y,t)dy$; the straight line has slope $\beta_{nc} = (\alpha_{cn}+1)/z_{cn} = 1/3$; (b) non-conserved noise ($D_0 = 1, \tilde{D}_0 = 0$). Inset: time evolution of $S(k_m,t)$ for the smallest k-value, k_m; the straight line has slope $2\alpha_{nc} + 1 = z_{nc} = 1$. For all panels, averages are over 100 realizations, time increases from blue to red, and the slope of the red solid line for small k is $-(2\alpha + 1)$ for $\alpha = \alpha_{cn} = -1/2$ [$\alpha_{nc} = 0$] on (a) [(b)].*

for system size $L = 2048$. Initial conditions are random (with 10^{-5} amplitude) for the deterministic case and zero otherwise. Parameters are fixed to $\nu_0 = \kappa_0 = 1$, $\lambda_0 = 10$, and space-time discretization steps are taken as $\delta x = 1$, and $\delta t \in [0.01, 0.05]$.

The scaling exponents characterizing the universality class can be readily identified in the evolution of the field roughness W and the structure factor $S(k, t)$. The numerical time evolution of $S(k, t)$ is shown in Fig. 6.1 for Eq. (6.1) (left panel), both with and without noise ($\tilde{D}_0 \neq 0$ and $\tilde{D}_0 = 0$), and for Eq. (6.18) (right panel). The scaling exponents predicted by Yakhot's argument [51] are indeed obtained:

- On the one hand, Eq. (6.1) renormalizes into Burgers equation, Eq. (6.19), with conserved noise $D = 0, \tilde{D} \neq 0$, for which $\alpha_{cn} = -1/2$ and $z_{cn} = 3/2$ [2] (see Chapter 5). The roughness exponent $\alpha_{cn} = -1/2$ is observed in the behavior of $S(k, t) \sim k^{-(2\alpha_{cn}+1)} = k^0$ for large t in both cases, while the exponent z_{cn} is observed by collapsing the structure factor $S = k^{2\alpha_{cn}+1} f(kt^{1/z})$ (as done in the top part of the panel for the stochastic case), or in the behavior of the roughness of the field $h(x, t) = \int_0^x u(y, t) \mathrm{d}y$, trivially expected to scale as $h \sim x^{\alpha+1}$ [17, 2], hence $W \sim t^{\beta_{nc}}$, with $\beta_{nc} = (\alpha_{cn} + 1)/z_{cn} = 1/3$ (as seen in the bottom part of the panel for the deterministic case).

- On the other hand, Eq. (6.18) renormalizes into Burgers equation, Eq. (6.19), with non conserved noise $D \neq 0$, for which $\alpha_{nc} = 0$ and $z_{nc} = 1$ [1] (see Chapter 4), as observed in the behavior of $S(k, t) \sim k^{-(2\alpha_{nc}+1)} = k^{-1}$ for large t and $S(k, t) \sim t^{(2\alpha_{nc}+1)/\alpha_{nc}} = t$ for very low values of k.

The scaling exponent values already imply that the KS equation with non-conserved noise belongs to a different universality class than that of the deterministic and conserved-noise equations, while the latter two share the same asymptotic values of the scaling exponents α and z.

6.2.2   Fluctuation statistics

One-point statistics: skewness and kurtosis

In order to assess in detail the fluctuation statistics for the different forms of the Kuramoto-Sivashinsky equation, we start by addressing the time evolution of both, the skewness and the excess kurtosis of the fluctuations of the u [Eqs. (6.1) and (6.18)] or h [Eq. (6.2)] fields, see Fig. 6.2. This figure presents results for: the deterministic KS equation, Eq. (6.1) with $\tilde{D}_0 = 0$ [panel (a)], the KS equation with conserved noise, Eq. (6.1) with $\tilde{D}_0 \neq 0$ [panel (b)], the KS equation with non-conserved noise, Eq.
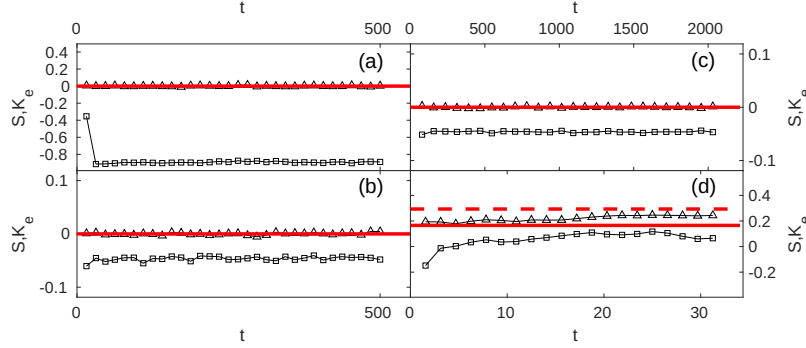
Figure 6.2: *Time evolution of the fluctuation skewness* $\mathcal{S}$ *(triangles) and excess kurtosis* $\mathcal{K}_e = \mathcal{K} - 3$ *(squares) for the Kuramoto-Sivashinsky equation, Eq. (6.1), with (a)* $\tilde{D}_0 = 0$, *(b)* $\tilde{D}_0 = 1$, *Eq. (6.18) with (c)* $D_0 = 0.1$, *and for the Kuramoto-Sivashinsky equation with KPZ-like nonlinearity, Eq. (6.2) with* $D_0 = 1$ *(d). In all cases,* $\nu_0 = \kappa_0 = 1$ *and* $\lambda_0 = 10$. *Red solid (dashed) lines correspond to the exact skewness (excess kurtosis) value of the Gaussian (a,b,c) and GOE-Tracy-Widom (d) distributions.*

(6.18) with $D_0 \neq 0$ [panel (c)], and the KS equation for the h field with non-conserved noise, Eq. (6.2) with $D_0 \neq 0$ [panel (d)], whose fluctuation statistics had not been previously reported in the literature. In all cases, times are prior to saturation to steady state.

In general, we can observe that the fluctuation distributions remain largely unchanged over time. Panels (a-c) actually show that, in the corresponding systems (and at variance with the behavior of the 1D KPZ equation), the PDF within the nonlinear time evolution actually coincides with the corresponding PDF at saturation. Such a saturation PDF is reported in [116] for the deterministic KS equation [panel (a)], while in the cases of the stochastic KS equation with conserved [panel (b)] and non-conserved [panel (c)] noise results are only available for the corresponding stochastic Burgers equation with which they share asymptotic scaling behavior (in terms of scaling exponents and, presumably, of fluctuation PDF), reported in [2] (see Chapter 5) and [1] (see Chapter 4), respectively.

More specifically, the time evolution of the skewness and excess kurtosis shown in Fig. 6.2 implies a PDF which exhibits a symmetric, notably platykurtic, non Gaussian behavior for the deterministic KS equation [panel (a)], and almost Gaussian behavior in the KS equation with conserved [panel (b)] or non-conserved noise [panel (c)]. The emergence of this symmetry in panels (a-c) can be interpreted in the same way as has been done for Burgers equations in Chapters 4 and 5, due to the combined $(u, x) \leftrightarrow (-u, -x)$ symmetry which also holds for Eqs. (6.1) and (6.18). Finite-size
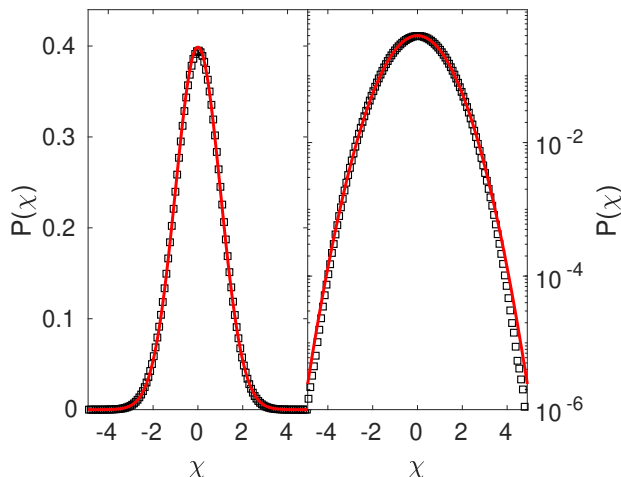
Figure 6.3: Fluctuation PDF for the Kuramoto-Sivashinsky equation with non-conserved noise, Eq. (6.18) (using $\nu_0 = \kappa_0 = 1, \lambda_0 = 10$ and $D_0 = 0.1$), in the nonlinear regime prior to saturation. The solid line provides the exact Gaussian form. The right panel is a linear-log representation of the same data shown on the left panel.

deviations of the excess kurtosis from its exact zero value seen in panels (b,c) are comparable to similar deviations in the corresponding cases of the stochastic Burgers equation with conserved or non-conserved noise (Chapters 5 and 4), respectively [2, 1]. Finally, panel (d) reproduces closely the expected GOE-TW behavior for the KS-KPZ equation with non-conserved noise. However, this case is well-known to feature quite different PDF behavior at steady state (Gaussian), as is the case in the 1D KPZ universality class [33].

One-point statistics: full PDFs

We also investigate the full PDFs for the fluctuation statistics of the u field in Eqs. (6.1) and (6.18) within the nonlinear regime prior to saturation to steady state. The case for the KS equation with non-conserved noise [panel (c) if Fig. 6.2] is presented in Fig. 6.3. It is Gaussian to a high precision, as expected.

For Eq. (6.1), we found a more complex behavior. We assess the full PDF for different values of the conserved-noise amplitude $\tilde{D}_0$; results are shown in Fig. 6.4. In the deterministic $\tilde{D}_0 = 0$ case, the rescaled fluctuations of u around its space average $\bar{u}$, defined as $\chi = (u - \bar{u})/\text{std}(u)$, exhibit a symmetric probability density function (PDF) whose tails decay much faster than those of a Gaussian distribution. Hence,
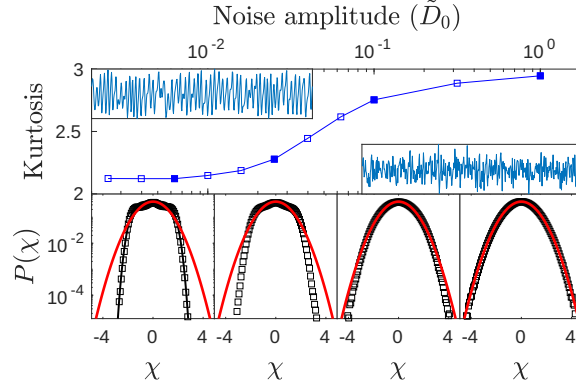
Figure 6.4: *Top panel: Kurtosis of u-fluctuations within the nonlinear regime prior to saturation for Eq. (6.1) with $D_0 = 0$, and different values of $\tilde{D}_0$. The line is a guide to the eye. The bottom panels show the PDF of standardised u-fluctuations (χ) for increasing values of $\tilde{D}_0$ left to right, which correspond to the filled squares in the top panel. Red solid lines show an exact Gaussian PDF; the black solid line is for $P[\chi] \sim \exp(-\chi^{4.5})$. Insets in top panel show representative $u(x)$ profiles for $\tilde{D}_0 = 0$ (deterministic case; left) and $\tilde{D}_0 = 1$ (conserved-noise case; right). Averages are over 10 realizations.*

the kurtosis is much smaller than 3, see Fig. 6.4. This PDF features two symmetric shoulders implying a relatively high frequency for two characteristic fluctuations in u-values, which can be approximately identified by inspection of the $u(x)$ profile shown in the figure. Similar distributions had been earlier reported at steady state [116]. The assessment of the full time evolution of the skewness and the excess kurtosis of the u fluctuations in Fig. 6.2 showed them to remain virtually unchanged along the nonlinear time regime.

The main qualitative features of the PDF are preserved for increasing values of the conserved-noise amplitude $\tilde{D}_0$, up to a certain value. For larger values of $\tilde{D}_0$, the fluctuation PDF starts to approach the Gaussian form, with a kurtosis which approaches the exact Gaussian value, see Fig. 6.4. Inspection of the representative $u(x)$ profile shown for $\tilde{D}_0 = 1$ indeed suggests the smaller predominance of characteristic fluctuations around the mean than in the deterministic case.

Covariance

As a complement of the reciprocal-space discussion and the one-point statistics, we provide details on the behavior of the covariance function in real space $C(x, t)$ as
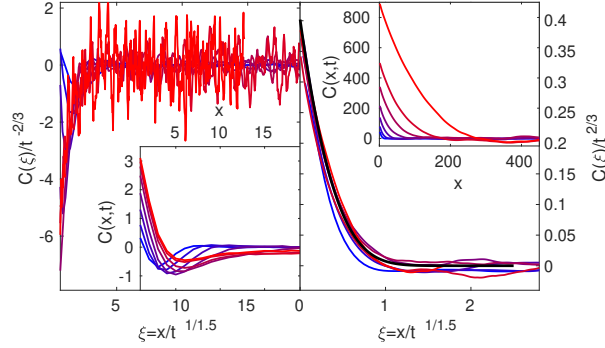
Figure 6.5: Data collapse of the covariance function $C(x,t)$ at different times in the growth regime (increasing from blue to red), from numerical simulations of Eq. (6.1), for $\phi = u$ (left panel) and $\phi = h = \int_0^x u(x',t)\,dx'$ (right panel), for $L = 2048$, $\delta t = 10^{-2}$, $\nu_0 = \kappa_0 = 1$, $\lambda_0 = 10$, $\tilde{D}_0 = 1$. The scaling exponents employed are those determined in the previous section for each case. In each panel the inset shows the uncollapsed data. The black solid line in the right panel shows the exact covariance of the Airy$_1$ process [33]. All units are arbitrary.

defined in Eq. 1.44, which corresponds to the KS equation, for $\phi(x,t) = u(x,t)$, and to the KS-KPZ equation, if we integrate numerically Eq. (6.1) while taking $\phi(x,t) = h(x,t) = \int_0^x u(x',t)\,dx'$. Results are shown in Fig 6.5. As can be seen, the data collapse in both cases to the expected scaling form, $C(x,t) = t^{2\beta}c(x/t^{1/z})$, with $c(y) \sim \text{cst.} - y^{2\alpha}$ for $y \ll 1$ and 0 for $y \gg 1$ [8, 11], using the corresponding values of the scaling exponents as determined in previous subsection. For the h field, collapse is to the exact covariance of the Airy$_1$ process, as expected in the growth regime for 1D KPZ scaling with periodic boundary conditions, see e.g. [33].

6.3 Chaotic-stochastic transition

In this section, we analyze the transition between large and low values of the noise strength both in Eq. (6.1) and in Eq. (6.2) and assess the relation between the changes in the fluctuation PDF and the eventual chaotic-stochastic transition in the predominant nature of the fluctuations. In order to assess the nature of the fluctuations, we measure the so-called scale-dependent Lyapunov exponent $\Lambda(\epsilon)$ discussed in Chapter 3 [75, 76], with ϵ being a distance between trajectories $\{T_i(x_0) = [\phi(x_0, (i+1)\Delta t), u(x_0, (i+2)\Delta t), ..., \phi(x_0, (i+m)\Delta t)]\}_{i=1}^I$ extracted from the time series $\phi(x_0, t)$ with $\phi = u$ for Eq. (6.1), $\phi = h$ for Eq. (6.2), x_0 is any fixed value of

x, and Δt is a sampling time. The full details about the computation of $\Lambda(\epsilon)$ from numerical data contained in time series are provided in Chapter 3.

6.3.1   Conserved KS equation

While the PDFs of the deterministic and the (large) conserved-noise cases of Eq. (6.1) are both even in χ, they are obviously different, specially with respect to the occurrence of "typical" fluctuation values. One could speak of two different sub-classes of a single universality class which additionally features $\alpha_{cn} = -1/2$ (white noise) and $z_{cn} = 3/2$ (superdiffusive spread of correlations, as in the 1D KPZ equation). Further dynamical properties suggest that we could even speak of a change in the universality *class*, with a transition at a well-defined value of $\tilde{D}_0$ separating the predominance of chaotic or of stochastic fluctuations. This interpretation is supported by a study of the behavior of the finite-size Lyapunov exponents of the system [77, 76] as a function of the conserved-noise amplitude.

We have studied numerically the behavior of $\Lambda(\epsilon)$ for Eq. (6.1) and different values of $\tilde{D}_0$, setting $m = 4$, $I = 4997$, and $\Delta t = \delta t$; results are shown in Fig. 6.6. Indeed, in the ($\tilde{D}_0 = 0$) deterministic case, $\Lambda(\epsilon)$ displays a well-defined plateau for small ϵ, and decays monotonously for $\epsilon \gtrsim 3 \cdot 10^{-3}$. The plateau width decreases for increasing $\tilde{D}_0$. In contrast, for "large" $\tilde{D}_0 = 1$, $\Lambda(\epsilon)$ decays monotonically with ϵ. We consider that a transition takes place when the plateau first vanishes, for $\tilde{D}_0 \simeq \tilde{D}_{0,c} = 1.6 \cdot 10^{-3}$. Actually, starting at this value the kurtosis $\mathcal{K}(\tilde{D}_0)$ departs from its deterministic value, approaching Gaussian behavior. Moreover, the L-dependence of the threshold value $\tilde{D}_{0,c}$ seems weak, see Fig. 6.6.

Finally, Fig. 6.7 provide a more detailed view than that provided by Fig. 6.4 on the transition between the deterministic and the stochastic PDF. We have identified the threshold value $\tilde{D}_{0,c} \simeq 0.0016$ as that value of $\tilde{D}_0$ above which not only the kurtosis departs from its deterministic ($\tilde{D}_0 = 0$) value but also for which the scale-dependent Lyapunov exponent $\Lambda(\epsilon)$ changes qualitative behavior from chaos- to stochastic-dominated fluctuations, see Fig. 6.6. Figure 6.7 illustrates how this change is more difficult to see by naked-eye inspection of the form of the field PDF. Note that for all cases considered in this figure, $\tilde{D}_0 > \tilde{D}_{0,c}$. The two leftmost panels display PDFs with inflection points which are akin to those characteristic of the PDF for purely chaotic fluctuations ($\tilde{D}_0 = 0$). Nevertheless, such inflection points disappear once the stochastic-noise amplitude increases even further above $\tilde{D}_{0,c}$, beyond which the fluctuation PDF eventually reaches fully-Gaussian form, as previously shown in Fig. 6.4.

Figure 6.6: (a) Scale-dependent Lyapunov exponent vs ϵ from numerical solutions of Eq. (6.1) within the nonlinear regime prior to saturation, for $D_0 = 0$ and conserved-noise amplitudes $\tilde{D}_0$ as in the legend. (b) Kurtosis of u fluctuations vs $\tilde{D}_0$ for $L = 1024$ (squares) and $L = 4096$ (circles). Inset: Distance bewteen $\mathcal{K}(\tilde{D}_0)$ and the kurtosis of the deterministic system, $\mathcal{K}_{det}$, vs $\tilde{D}_0$. For each L, the difference grows (blue data) to the right of the corresponding red point. All lines are guides to the eye. Averages are over 10 realizations.
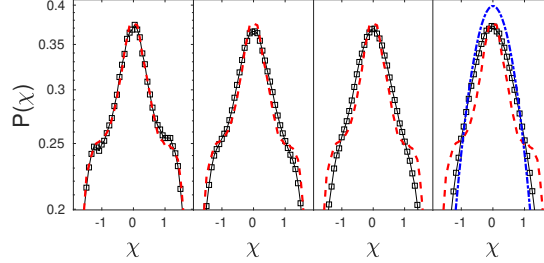
Figure 6.7: *Fluctuation PDF for the standardised u-fluctuations (χ) of the Kuramoto-Sivashinsky Eq. (6.1), using $L = 2048$, $\delta t = 10^{-2}$, $\delta x = 1$, $\nu_0 = \kappa_0 = 1$, $\lambda_0 = 10$, $D_0 = 0$, and increasing values of $\tilde{D}_0 = 0.0063$, 0.016, 0.025, and 0.040, left to right. Red dashed lines show the PDF for the deterministic $\tilde{D}_0 = 0$ case; black solid lines guide the eye for the numerical values shown as squares; the blue dotted-dashed line in the rightmost panel shows the exact Gaussian PDF. All vertical axes are in logarithmic scale. Averages are made over 10 noise realizations.*

6.3.2 KS-KPZ equation

We have additionally assessed the transition between chaotic and stochastic kinetic roughening behavior in the KS equation with KPZ nonlinearity and non-conserved noise, Eq. (6.2), which describes the integral field $h(x,t) = \int_0^x u(x',t) \; dx'$ for Eq. (6.1). In Fig. 6.8 we confirm that, for an increasing noise amplitude D_0, $\Lambda(\epsilon)$ behaves similarly to what has been obtained for Eq. (6.1): the $(D_0 = 0)$ deterministic system shows a plateau of ϵ-independent behavior which disappears for $D_0 \gtrsim 0.01$, beyond which stochastic behavior ensues. However, now the transition does not reflect into a change between two different fluctuation PDFs. Indeed, in the chaotic case $(D_0 = 0)$ fluctuations of Eq. (6.2) are known to be Tracy-Widom distributed in the nonlinear regime prior to saturation [118], while Fig. 6.8 indicates that so do fluctuations for a "large" value of stochastic noise, for which fluctuation PDF had not been reported in the literature yet, to our knowledge. Asymptotic scaling exponent values are known to be 1D KPZ, irrespective of the value of D_0 [120, 118].

6.4 Conclusions

In summary, we have seen that Yakhot's classic argument on the asymptotic equivalence between spatiotemporal chaos and kinetic roughening holds only partly for

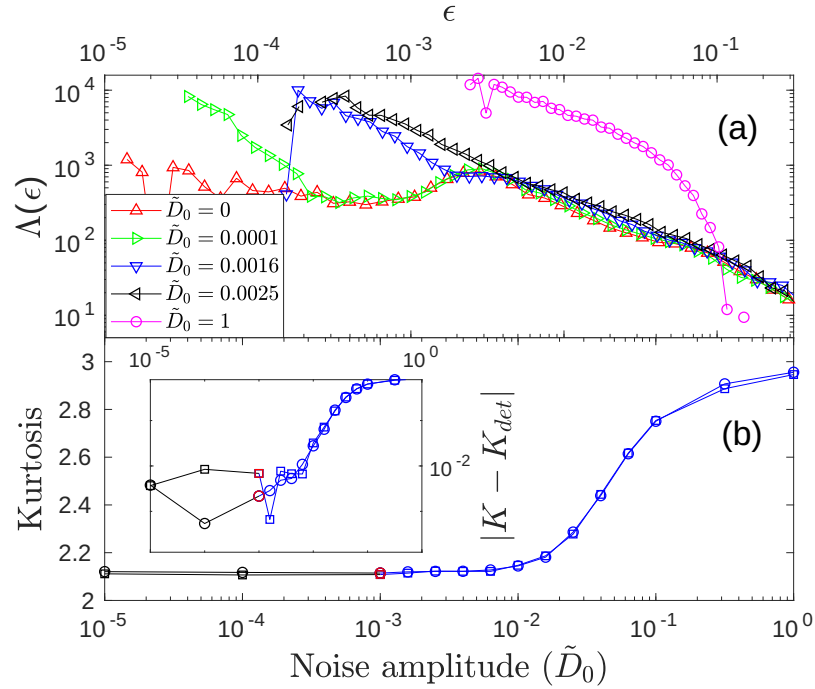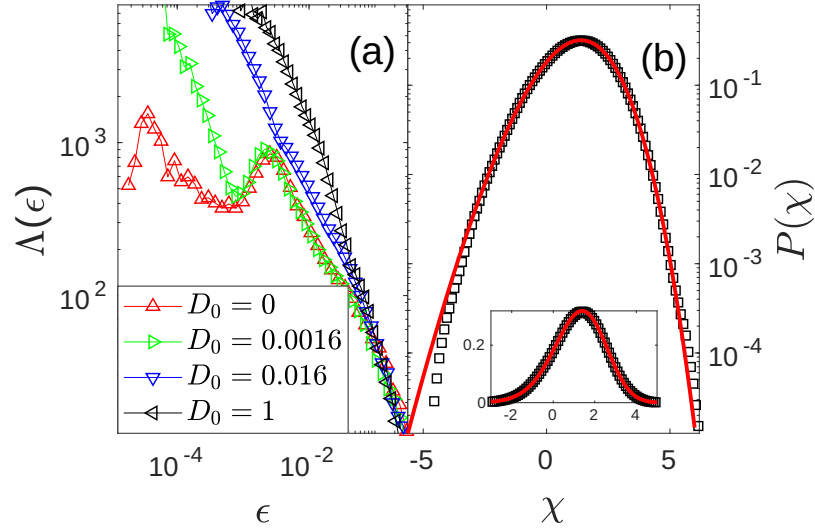*Figure 6.8: (a) Scale-dependent Lyapunov exponent for solutions of the KS Eq. (6.2) within nonlinear regime prior to saturation, for noise amplitudes D_0 as in the legend. Remaining parameters as in previous figures. (b) PDF of h-fluctuations within nonlinear regime for $D_0 = 1$. Red solid line shows the exact GOE-TW PDF [31, 18, 33]. Inset: same data in a linear plot. Averages are over 10 realizations.*

Eqs. (6.1) and (6.2); specifically, for Eq. (6.1), different universality classes occur with different field PDF, albeit with the same scaling exponent values. This fact is not captured by Yakhot's argument which, while incorporating the basic system symmetries (conserved vs non-conserved dynamics, etc.), misses key differences between PDFs which are otherwise consistent with the former. The dynamical role of symmetries can be subtle indeed in the present class of nonequilibrium critical systems [87, 121, 1], as described in Chapters 4 and 5 for the Burgers case.

Crucially, each one of the kinetic roughening universality classes occurring in Eq. (6.1) correlates with the nature (chaotic or stochastic) of the mechanism controlling fluctuations in the system, the transition between them nontrivially occurring at a nonzero stochastic noise amplitude. This transition could be experimentally verified, for instance in epitaxial growth of vicinal surfaces [122], where the KS equation describes the dynamics of atomic steps separating terraces under non-negligible adatom desorption [123]. In such a case the equation for the step slope is Eq. (6.1), where $\tilde{D}_0$ scales as an inverse power of the characteristic desorption time. For the KS-KPZ equation, Eq. (6.2), although an analogous transition takes place in the dominance of chaotic or stochastic fluctuations, on both sides of the transition the field PDF and the scaling exponents are those of the 1D KPZ universality class. Indeed, the TW distribution is not only relevant to the *stochastic* 1D KPZ class, but also describes the fluctuations of *deterministic* chaotic systems [124]. This coincidence might well be accidental and limited to 1D systems. Its exploration in 2D might provide some clue on the relation between the deterministic KS and the stochastic KPZ equations in higher dimensions [125], an open challenge in the fundamental understanding of spatiotemporal chaos [126].

The results reported in this Chapter on the transition between chaotic and stochastic universality classes for Eqs. (6.1) and (6.2) are summarized graphically in Fig. 6.9. Note that, possibly, the most frequent (albeit non-exclusive) interpretation for the noise intensity in physical models in which noisy Kuramoto-Sivashinsky equations have been derived as physical models, is as temperature, although additional ones are also possible and have been proposed, such as an an external particle flux.

With respect to the specifics of the present transition, it would be interesting to obtain analytical estimates on the threshold noise amplitude and to assess nontrivial consequences on physical quantities beyond the field PDF. The behavior discussed above for $S(k, t)$ already indicates differences in the equal-time two-point statistics, but two-time statistics may introduce additional novelties. In this process, it would be interesting to find analogous transitions, but in which the chaotic and stochastic
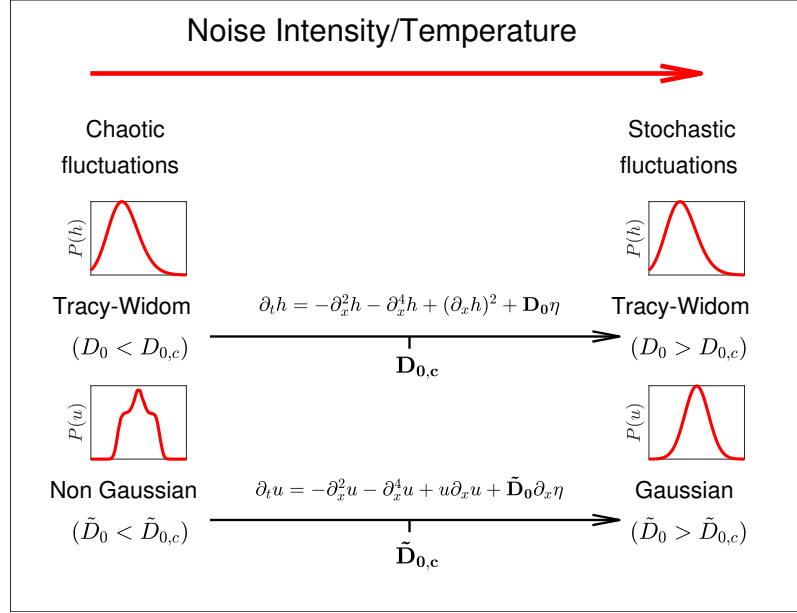
Figure 6.9: Graphical summary of results reported in this Chapter for Eqs. (6.1) and (6.2).

"phases" might also differ by the values of the scaling exponents.

Finally, the correlation between the field PDF and the nature of the fluctuations underscores the importance of assessing the PDF explicitly, to correctly identify the kinetic roughening universality class. This is particularly critical in view of the plethora of experimental complex systems that can be described by a paradigmatic model like the KS equation, in its different (conserved or non-conserved; deterministic or stochastic) forms, especially when both, chaotic and stochastic fluctuations may be operative at comparable space-time scales.

Chapter 7

Inviscid KPZ and Burgers equations: novel universality classes

7.1 Introduction

In this Chapter, self-organization processes are studied in the context of some peculiar limits for thin fluid films. First, consider the addition of a dispersion term to the Kuramoto-Sivashinsky (KS) equation leading to the *generalized* Kuramoto-Sivashinsky (gKS) equation mentioned in section 2.2.2. This equation has been derived in the modelling of thin fluid films, e.g. for a film falling down an uniformly heated wall [127], a film falling down a vertical fiber [128], or liquid films sheared by a turbulent gas [129]. It reads [149]

$$\partial_t u = -\partial_x^2 u - \partial_x^4 u + u\partial_x u + c\partial_x^3 u, \tag{7.1}$$

where c is the parameter that governs the dispersion term. It is known [57, 149] that the gKS equation is a paradigmatic model for a peculiar transition between chaotic behavior and regular behavior in spatially extended systems; specifically, for small values of c the dynamics of the gKS equation exhibits the same spatiotemporal chaotic behavior discussed in Chapter 6 for the KS equation, but for large enough values of c the dynamics of the gKS equation exhibits travelling wave-like solutions [130]. In the limit of large dispersion $c \gg 1$, the travelling waves in the solutions are analogous to those present in the solutions of the celebrated Korteweg-de Vries (KdV) equation,

$$\partial_t u = c\partial_x^3 u + u\partial_x u, \tag{7.2}$$

which has also been proposed in the modelling of thin fluid films, like superfluid Helium films [131].

Our first goal in this Chapter is to assess the behavior of the *stochastic* KdV equation

$$\partial_t u = c\partial_x^3 u + u\partial_x u + \partial_x \eta. \tag{7.3}$$

obtained by adding a conserved noise term to Eq. (7.2) analogous to the additive noise term obtained for the KS equation in Chapter 6, due to thermal fluctuations. Equation (7.3) will be shown below to exhibit an unprecedented kinetic roughening behavior which is similar to a random deposition process (see Chapter 1) but with saturation to steady state. Moreover, under the change of variable $u = \partial_x h$ in analogy with the relation between Burgers and KPZ equations assessed in Chapter 5, Eq. (7.3) becomes

$$\partial_t h = c\partial_x^3 h + (\partial_x h)^2 + \eta. \tag{7.4}$$

As a result of our numerical work, intrinsic anomalous scaling behavior is found for Eq. (7.4), concurrent with symmetry emergence for the field fluctuations.

We will also assess in this Chapter the inviscid $c \to 0$ limit for both Eqs. (7.3) and (7.4). This limit corresponds to the ultra-low viscous and ultra-low surface tension limit in the equation derived in Chapter 6 for an ultrathin fluid film falling down a slope. We find the same kinetic roughening behavior as for Eqs. (7.3) and (7.4) for $c > 0$, hence we conclude that the dispersion term does not affect these properties.

Notice that neither Eq. (7.3) nor Eq. (7.4) had been previously integrated successfully in the literature up to our knowledge for the type of noise we are considering; the addition of such noise makes the solutions numerically unstable unless a proper numerical method is employed.

On the other hand, the relation between continuum equations and discrete models in which similar kinetic roughening processes occur of the same universality class [like the totally asymmetric simple exclusion process (TASEP) [33, 18, 31, 132] and the reaction-diffusion fronts [133] being in the KPZ universality class] is adressed in this Chapter through the study of a surface growth process in the context of the celebrated Ising model, based on the proposal of [134], and in which the scaling exponent values suggest a relation to the inviscid KPZ equation.
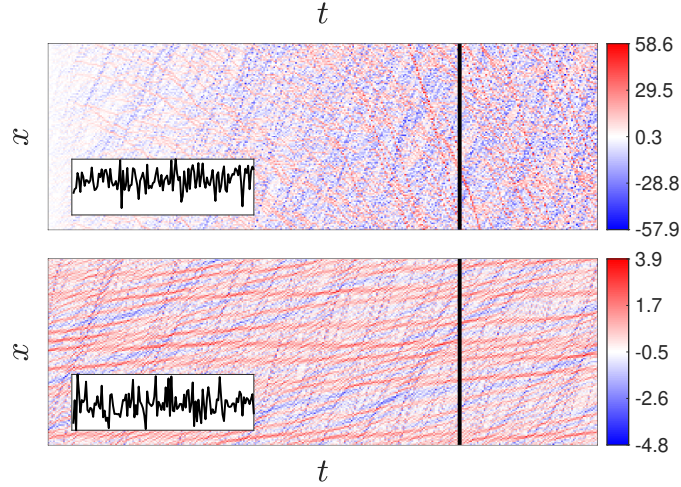
Figure 7.1: Spatiotemporal evolution of Eqs. (7.2) (bottom) and (7.3) (top), namely the deterministic and the stochastic KdV-Burgers equations, respectively. Insets represent the corresponding surface morphology along the black solid line for each case. Here x and t increase bottom to top (1 to 128) and left to right (0 to 64), respectively.

7.2   Kinetic roughening

7.2.1   Kinetic roughening of the KdV equation

The two versions of the stochastic KdV equation, namely, with Burgers and KPZ nonlinearities, equations (7.3) and (7.4) respectively, have been successfully integrated numerically using the pseudo-spectral method developed in [69] (see Chapter 3 for more details). Although there are examples in the literature of successful integration of the KdV equation with temporal noise $\eta(t)$ [135], there are no precedents of numerical integration of the KdV equation under the addition of spatiotemporal noise up to our knowledge. In all cases we have studied, the dispersion parameter c has been set to 1. We begin with a comparison of the field morphologies for the stochastic and the deterministic KdV-Burgers equations with a random initial condition [Eq. (7.3) with $\eta = 0$ and $\eta \neq 0$, respectively] that is shown in Fig. 7.1. Travelling wave-like structures are appreciated in the deterministic case, while a much more disordered pattern appears in the stochastic case, in which fluctuations grow substantially with time. We wonder at this point if a kinetic roughening process is happening in the stochastic case, in which the magnitude of the fluctuations
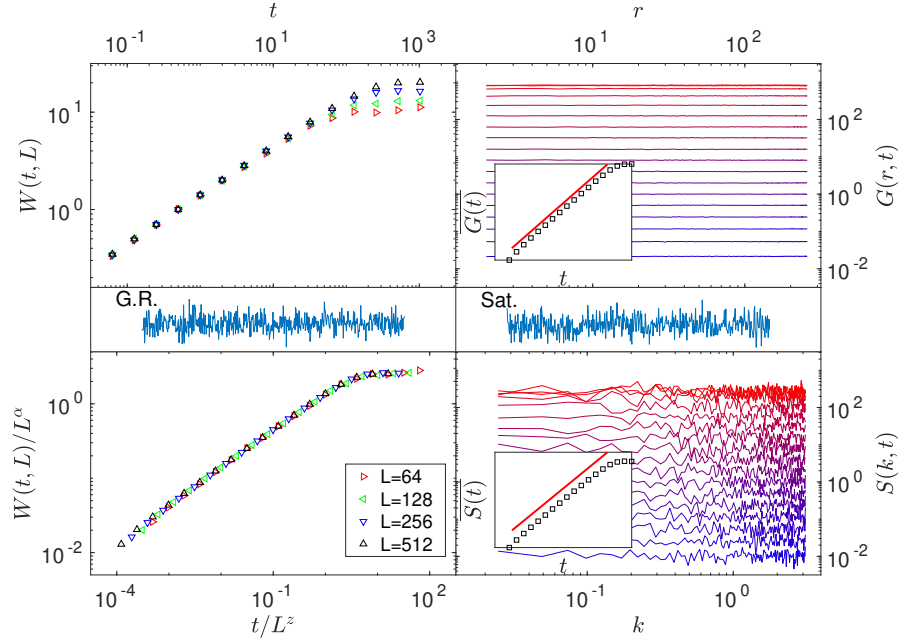
Figure 7.2: *Time evolution for the roughness, $W(t, L)$, height difference correlation function, $G(r, t)$, and structure factor, $S(k, t)$, of the field $u(x, t)$ in Eq. (7.3). The data collapse for the roughness as in Eq. (1.12) is also shown for $\alpha = 1/3$ and $z = 2/3$. Morphologies $u(x)$ for growth regime (G.R.) and saturation (Sat.) are also depicted. Insets represent the evolution in time for the average values of $G(r, t)$ over r and $S(k, t)$ over k (denoted by overbars), where solid red lines have unit slope.*

grows with time. The time evolution of the field roughness $W(t)$ and the structure factor $S(k, t)$ of the stochastic KdV equation in both Burgers-like and KPZ-like [Eqs. (7.3) and (7.4), respectively] versions have been measured. The evolution of $W(t)$ is shown in the left panels of Figs. 7.2 and 7.4. In both cases, the field roughness follows a Family-Vicsek scaling as in Eq. (1.12), leading to the data collapse shown in the left bottom panels of both figures with exponents $\alpha = 1/3$, $\beta = 1/2$, and $z = 2/3$ for KdV-Burgers, and $\alpha = 1$, $\beta = 1$, and $z = 1$ for KdV-KPZ. Notice that these values are in agreement with the Galilean scaling relations (which holds if there is not renormalization of the nonlinear terms of the equation), $\alpha + z = 1, 2$ for Eqs. (7.3) and (7.4), respectively.

The structure factor for KdV-Burgers, Eq. (7.3), exhibits a trivial scaling behavior as it does not depend on k, while it increases with time as $S(t) \sim t^{2\beta}$ for times prior
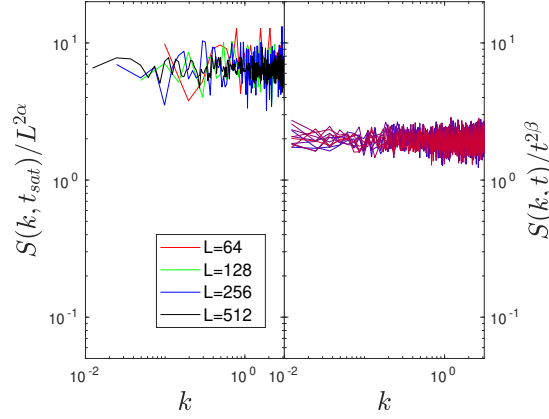
Figure 7.3: *Partial collapses of the structure factor $S(k,t)$ of the field $h(x,t)$ in Eq. (7.3) according to Eq. (7.5) for $\alpha = 1/3$ and $\beta = 1/2$. Blue to red colors correspond to increasing times (prior to saturation t_{sat}) in the right panel.*

to saturation ($t < t_{sat}$); finally, the structure factor scales with the system size as $S(t_{sat}) \sim L^{2\alpha}$ at saturation. This behavior is induced by the independence of S with k and Eq. (1.5), and is also explicitly shown in Fig. 7.3. In summary, the scaling of $S(k,t)$ follows a scaling form which is analogous to the one of the roughness W, namely,

$$ S(k,t) \sim L^{2\alpha} k^{-(2\alpha_s + d)} f_S(t/L^z), \qquad f_S(u) \sim \begin{cases} u^{2\beta}, & u \ll 1 \\ \text{Cnst}, & u \gg 1 \end{cases}, \qquad (7.5) $$

which is *not* conventional anomalous scaling in the sense described in Chapter 1. Its steady state behavior is however similar to that obtained in [136] for a stochastic model of independent pulses. Note that the k-independence $S \sim k^0$ leads to an effective spectral exponent $\alpha_s = -1/2$ in Fourier space, $S(k) \sim k^{-(2\alpha_s + 1)}$, which is closely related with the local roughness exponent α_{loc}, as discussed in Chapter 1. As α_{loc} can be measured from the behavior of the height-difference correlation function $G(r,t) \sim r^{2\alpha_{loc}}$, the dependence $G \sim r^0$ shown in Fig. 7.2 leads to $\alpha_{loc} = 0$. It is unclear if a negative value $\alpha_{loc} < 0$ could be distinguished from $\alpha_{loc} = 0$ in the correlation function.

In contrast, the structure factor for the KdV-KPZ equation, Eq. (7.4), does exhibit an intrinsic anomalous scaling behavior consistent with Eq. (1.17), where $\alpha_s = 1/2$ is the spectral roughness exponent. Both $S(k,t)$ and its collapse are shown on the right panels of Fig. 7.4.

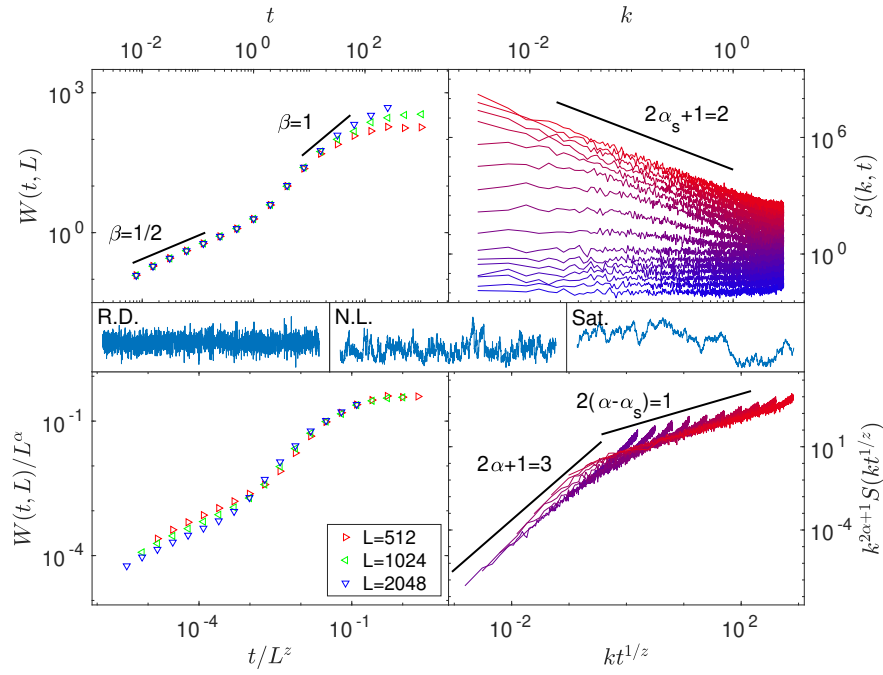Figure 7.4: *Time evolution for the roughness, $W(t, L)$ and the structure factor $S(k, t)$ of the field $h(x, t)$ in Eq. (7.4). The data collapses for the roughness and structure factor (times correspond to the same ones as in W) are also shown using $\alpha = 1$, $z = 1$, and $\alpha_s = 1/2$. Morphologies $h(x)$ for the random deposition (R.D.), nonlinear (N.L.), and saturation (Sat.) regimes are also depicted.*

7.2.2 Kinetic roughening of the inviscid Burgers and KPZ equations

In this section we drop the dispersive term in Eqs. (7.3) and (7.4) and study the ensuing equations, namely

$$\partial_t u = u\partial_x u + \partial_x \eta, \tag{7.6}$$

and

$$\partial_t h = (\partial_x h)^2 + \eta, \tag{7.7}$$

respectively. Note that Eqs. (7.6) and (7.7) correspond directly to the *inviscid* Burgers and KPZ equations, in which the surface tension/viscosity term is set to zero. Quite importantly, in such a case none of the exact results (exponents, PDF) known for the 1D KPZ equation hold, as they use as starting point the so-called Cole-Hopf transformation which requires $\nu \neq 0$ e.g. in Eq. (1.42) [34, 18, 33].

We integrate Eqs. (7.6) and (7.7) numerically. The same observables as those depicted in Figs. 7.2 and 7.4 for Eqs. (7.3) and (7.4), respectively, are shown in Figs. 7.5 and 7.6. They exhibit the same behavior. Hence, this result suggests that the dispersive term has a null effect in the kinetic roughening behavior of these equations. That could be considered to be natural, as the dispersive ik^3 term in Fourier space from the third derivative, being purely imaginary, makes perturbations travel along space at different velocities for different length scales, but does not affect their magnitude.

In order to study the full relation with the KPZ and the Burgers universality classes, which had a conspicuous role in previous chapters of this thesis, the fluctuation statistics for the inviscid Eqs. (7.6) and (7.7) have been studied. In Fig. 7.7, the time evolution of the skewness $\mathcal{S}$ and kurtosis $\mathcal{K}$ is shown and compared with those for a Gaussian PDF. In the evolution of the KdV-Burgers equation, Gaussian fluctuations hold throughout the whole temporal evolution. In the KdV-KPZ case, the fluctuations exhibit a symmetric non-Gaussian behavior. This behavior, however, corresponds to a PDF whose tails can be fitted as $P \sim \exp(-\chi^2)$ but that is much flatter than Gaussian near the origin. Hence, symmetry of the fluctuation PDF emerges for the inviscid Burgers equation in a similar way as it was described in Chapters 4 and 5 for Burgers equation, despite the lack of up-down $u \leftrightarrow -u$ symmetry, which could also be associated to the $(x, u) \leftrightarrow (-x, -u)$ invariance. On the other hand, Eq. (7.7) is also not up-down ($h \leftrightarrow -h$) symmetric, but it *is* $x \leftrightarrow -x$ symmetric, hence there is not a combined symmetry that allows us to understand the symmetry emergence on its fluctuations. Unfortunately, the absence of the linear
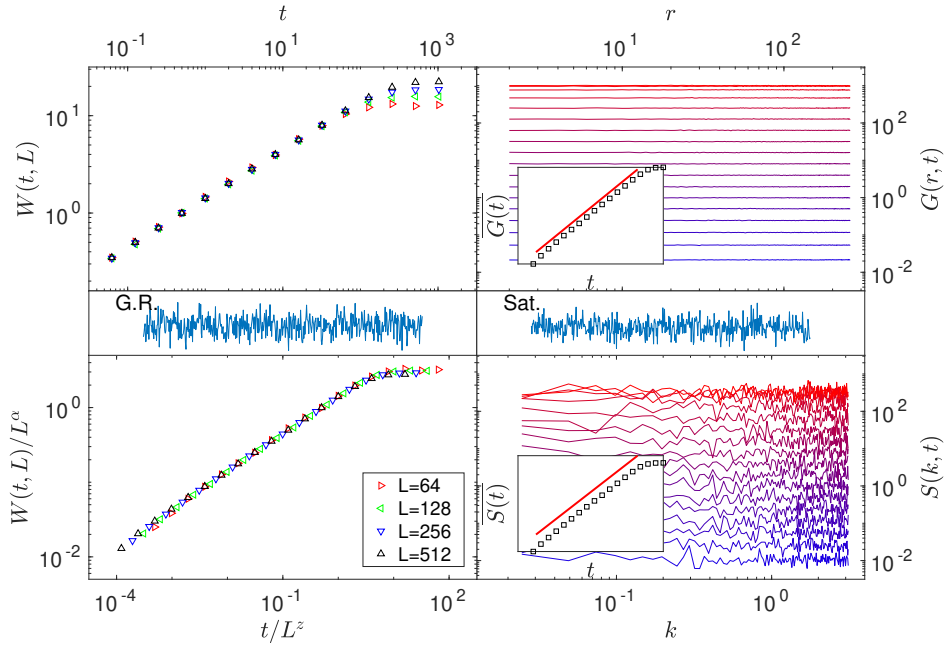
Figure 7.5: *Time evolution for the roughness, $W(t,L)$, the height-difference correlation function, $G(r,t)$, and the structure factor, $S(k,t)$ (times correspond to the same ones as in W), of the field $u(x,t)$ in Eq. (7.6). The data collapse for the roughness as in Eq. (1.12) is also shown for $\alpha = 1/3$ and $z = 2/3$. Morphologies $u(x)$ for growth regime (G.R.) and saturation (Sat.) are also depicted. Insets represent the evolution in time for the average values of $G(r,t)$ over r and $S(k,t)$ over k, where solid red lines have unit slope.*

Figure 7.6: *Time evolution for the roughness, $W(t,L)$ and the structure factor $S(k,t)$ of the field $h(x,t)$ in Eq. (7.7) (times correspond to the same ones as in W). The data collapses for the roughness and structure factor are also shown using $\alpha = 1$, $z = 1$, and $\alpha_s = 1/2$. Morphologies $h(x)$ for the random deposition (R.D.), nonlinear growth (N.L.), and saturation (Sat.) regimes are also depicted.*

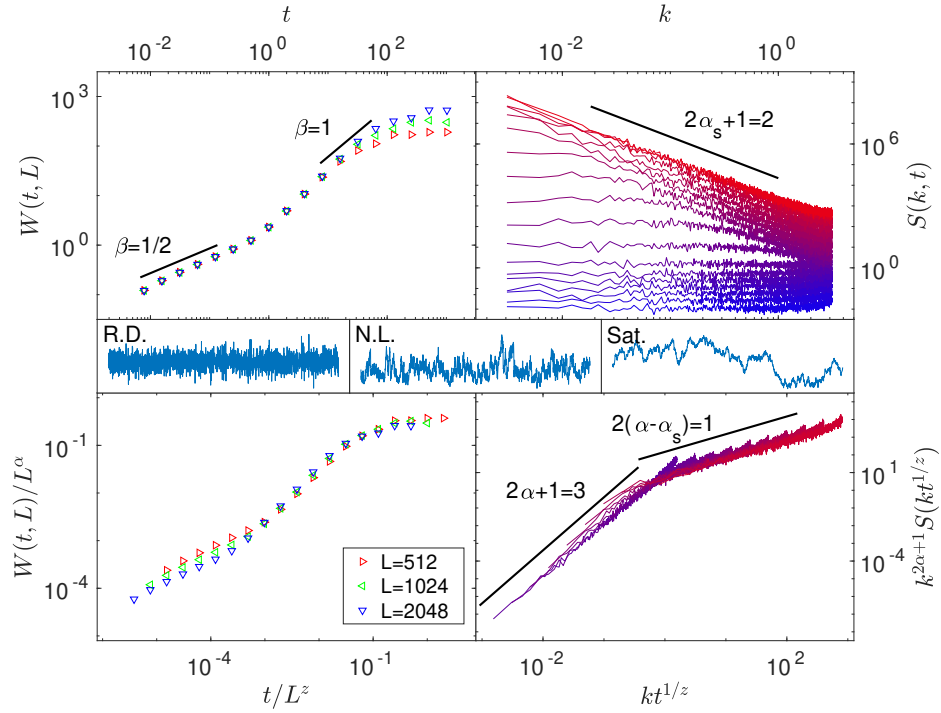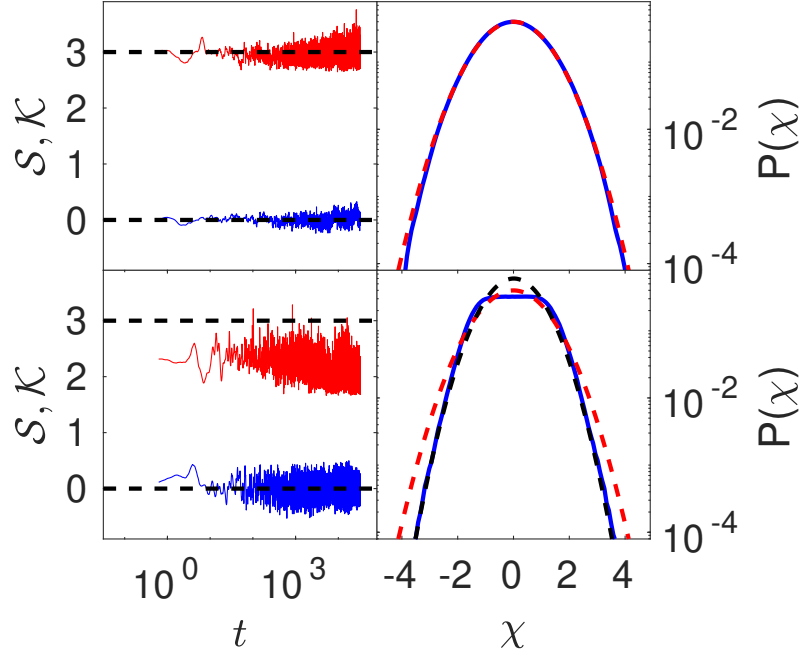Figure 7.7: *Time series for the skewness $\mathcal{S}$ and kurtosis $\mathcal{K}$ (blue and red, respectively, in the left panels) and probability density function (PDF, solid blue lines in right panels) of the normalized field fluctuations [$\chi = (\phi - \overline{\phi})/\mathrm{std}(\phi)$] for the inviscid Burgers equation [Eq. (7.6), here $\phi = u$] (top) and the inviscid KPZ equation [Eq. (7.7), here $\phi = h$] (bottom). Red dashed lines correspond to the Gaussian PDF. The black dashed line corresponds to $P(\chi) = 0.6 \exp(-0.7\chi^2)$.*

term in these equations prevents the use of e.g. dynamic renormalization group for further analysis in these cases.

The scaling exponents and fluctuation statistics found for the inviscid Burgers and KPZ equations lead to the identification of new universality classes. In Table 7.1 we summarize these results and contrast them with the analogous ones for the full stochastic Burgers and KPZ equations, which differ from their inviscid counterparts at least with respect to exponent values. Also, note that the inviscid Burgers equation, while being the space derivative of the inviscid KPZ equation, has exponent values which do not follow trivially from those of the latter, in contrast to the relation studied in Chapter 5 for the $\nu \neq 0$ case.

For the inviscid KPZ equation, its generalization to higher-dimensional substrates

Universality class	Reference equation	α	α_s	z	$P[\phi]$
Burgers	$\partial_t\phi = \partial_x^2\phi + \phi\,\partial_x\phi + \partial_x\eta$	$-1/2$	$-1/2$	$3/2$	Gaussian
Inviscid Burgers	$\partial_t\phi = \phi\,\partial_x\phi + \partial_x\eta$	$1/3$	$1/3$	$2/3$	Gaussian
KPZ	$\partial_t\phi = \partial_x^2\phi + (\partial_x\phi)^2 + \eta$	$1/2$	$1/2$	$3/2$	Tracy-Widom
Inviscid KPZ	$\partial_t\phi = (\partial_x\phi)^2 + \eta$	1	$1/2$	1	Pseudo-Gaussian

Table 7.1: *Scaling exponents and fluctuation statistics in the Burgers and KPZ (in both their viscid and inviscid forms) universality classes for $d = 1$.*

is straightforward, namely,

$$\partial_t h + (\nabla h)^2 + \eta = 0. \tag{7.8}$$

Such is not the case for equations with Burgers-like nonlinearities. Hence, in principle, the definition of an *inviscid KPZ universality class* seems a natural one. However, simulations of the inviscid KPZ equation present numerical stability problems e.g. for $d = 2$. In Fig. 7.8 the numerical $h(x, y, t)$ profiles are shown to exhibit blow-up. This coincides with some expectations from previous results reported in the literature [137], in which a surface described by the 2D KPZ equation is argued to become multivalued in the $\nu = 0$ limit. In the next section, we will assess an alternative approach for the inviscid KPZ equation in higher dimensions, which differs from direct numerical integration; namely, the study of a discrete model, hopefully free from finite-time blow-up, which may potentially belong to the same universality class.
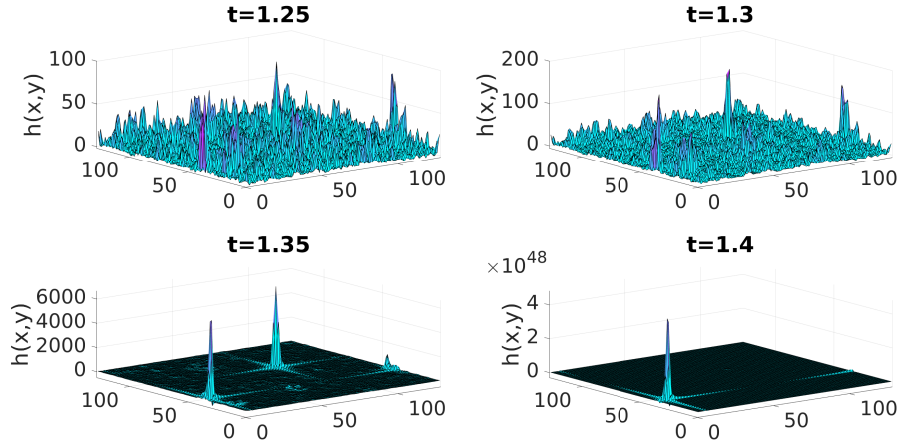
Figure 7.8: Evolution of the field $h(x, y)$ of solutions of the inviscid KPZ equation [Eq. (7.8)] for a two-dimensional substrate at different times close to the numerical blow-up.
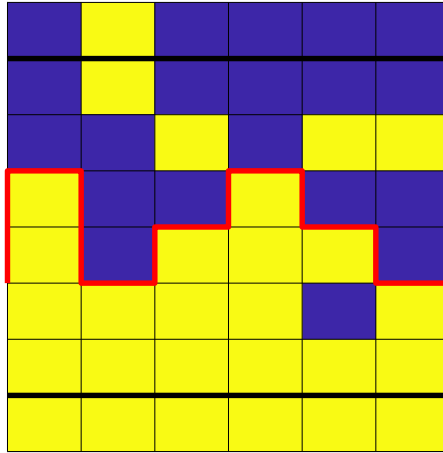
7.3   Ising model and the inviscid KPZ universality class

In this section we will discuss how a surface growth model derived from an Ising system could be classified as a member of this thus-far unreported *inviscid KPZ universality class*. The scaling behavior of a 1D interface associated with an equilibrium 2D Ising system at the critical temperature $T = T_c$ has been studied in [134], see below for precise definitions. They observe anomalous scaling with $\alpha = 1$ ($W_{sat} \sim L$) and $\alpha_s = 1/2$ [$S(k) \sim k^{-2}$], the same exponents as those we have found to describe the spatial scaling of the fluctuations in the inviscid KPZ equation, as seen in the previous section. However, no time-related exponents are measured in [134]. That is the reason why we proceed to study the full dynamics of this process, in order to determine if not only at steady state, but also in the growth regime, the scaling is the same as that found for the inviscid KPZ equation. We will study below the full dynamic scaling, including the temporal behavior, of this system by simulating the temporal evolution of Ising spin domains in 2D and 3D, with the boundary conditions described in Fig. 7.9. For that purpose, two different approaches are considered: assessing the evolution of the spin field from the point of view of the continuous Ginzburg-Landau equation and, alternatively, via a discrete Monte Carlo Metropolis algorithm.

7.3.1   System description

We define a 1D (2D) spatially extended surface $h(x, (y))$ from a 2D (3D) spin domain $\{s_{i,j,(k)}\}$, $s_{i,j,(k)} = \pm 1$, $i, j, k = 1, 2, ..., N$, as proposed in [134]. Dirichlet (fixed) and Neumann (free) boundary conditions are fixed on each boundary in one of the system dimensions; specifically, $s_{0,j,(k)} = +1$ and $s_{N+1,j,(k)} = s_{N,j,(k)}$, respectively. Periodic boundary conditions are considered in the other dimensions, i.e., $s_{i,0,(k)} = s_{i,N,(k)}$, $s_{i,N+1,(k)} = s_{i,1,(k)}$, $s_{i,j,(0)} = s_{i,j,(N)}$, and $s_{i,j,(N+1)} = s_{i,j,(0)}$. We will refer to these boundary conditions as *magnet*. Then, the set $\mathcal{C}_{i,j,(k)}$ is defined, such that $\mathcal{C}_{i,j,(k)} = 1$ for all the spins aligned with the $+1$ spins fixed at the Dirichlet boundary and connected to each other by nearest-neighbor paths, and $\mathcal{C}_{i,j,(k)} = 0$ otherwise. The height of the surface is finally defined as

$$h(x, (y)) = \sum_{i=1}^{N} \mathcal{C}_{i,x,(y)}. \tag{7.9}$$

Figure 7.9: *Definition of a height profile (red solid line) from a certain 6×6 spin domain (yellow and blue colors correspond to $+1$ and -1 spin values, respectively). The spin rows below and above the botton and top black solid lines illustrate the Dirichlet and Neumann boundary conditions, respectively.*

An illustrative 2D spin domain with $N = 6$ under these boundary conditions, as well as its corresponding $h(x)$ surface profile, is depicted in Fig. 7.9.

7.3.2   Ginzburg-Landau approach

The Ginzburg-Landau (GL) equation [138]

$$\partial_t m = \frac{1}{2} \left(\partial_x^2 m + m - m^3 \right) + D\eta, \tag{7.10}$$

where m denotes a local magnetization field and η a white additive noise of unit variance, is an effective coarse-grained model that can be used to describe the evolution of the scalar magnetization of a ferromagnet around thermal equilibrium [139]. We use this model in order to simulate the full dynamic evolution of a ferromagnetic system to equilibrium. We also define here a spin lattice $s_{i,j,(k)}$ by discretizing $s_{i,j,(k)} = +1$ if $m_{i,j,(k)} > 0$ and $s_{i,j,(k)} = -1$ otherwise, from which we will define the field $h(x)$ using Eq. (7.9). The same boundary conditions as those proposed in [134] have been considered, see Fig. 7.9.

Identification of the critical temperature

First, we assess the behavior of this system at different values of the noise strength D in order to determine the noise amplitude corresponding to the critical temperature T_c. A simple finite-difference scheme is used for the integration of Eq. (7.10). In Fig. 7.10 we show how the relative fluctuation of the magnetization field,

$$M = \frac{\langle m^2(\mathbf{x})\rangle - \langle m(\mathbf{x})\rangle^2}{L^d D}, \tag{7.11}$$

at steady state $t \gg 1$ exhibits a divergence as $M \sim L^{\gamma/\nu}$ for the critical value $D = D_c \simeq 0.9$ corresponding to the critical temperature $T = T_c$. Here, $\gamma = 7/4$ and $\nu = 1$ are the Ising critical exponents in two dimensions [138]. This divergence is more clear if we consider a spin system in which all the boundary conditions are periodic, as shown in the bottom panels of Fig. 7.10.
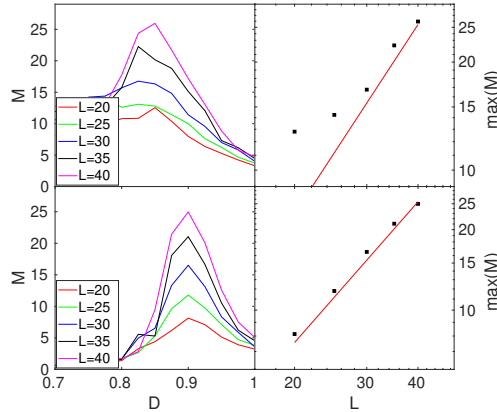
Figure 7.10: Determination of the noise strength D_c corresponding to the critical temperature T_c for the GL equation in a 2-dimensional spatial domain. Left panels show the magnetization fluctuation M at steady state for different values of D and lateral system size L [magnet boundary conditions (top) and periodic boundary conditions (bottom)]. At $D = D_c$, corresponding to $T = T_c$, M diverges with L as a $M \sim L^{7/4}$ (red solid line) as expected from the 2D Ising critical exponents $\gamma = 7/4$ and $\nu = 1$ [140].

Dynamics at $T = T_c$

Once the noise amplitude corresponding to the critical temperature is determined, the full critical dynamics of the field $h(x)(t)$ is evaluated at $D = D_c$. Numerical

simulations of Eq. (7.10) have been carried out and the evolution of the roughness $W(t)$ and the structure factor $S(k,t)$ have been studied. A homogeneous initial condition $m_{i,j} = -1$ for all $i,j = 1,2,...,L$ has been considered, while the opposite spin value has been considered at the Dirichlet boundary corresponding to $i = 0$. In Fig. 7.11, the evolution of both the surface roughness $W(t)$ and the structure factor $S(k,t)$ are depicted, as well as the data collapse corresponding to the scaling exponents $\alpha = 1$ ($W \sim L$), $\alpha_s = 1/2$ [$S(k,t_{sat}) \sim k^{-2}$] and $z = 1$, hence $\beta = 1$. A random deposition regime [with $\beta = 1/2$ and an almost flat $S(k)$] is observed at short times, as for the inviscid KPZ equation. Morphologies for $h(x)$ profiles in the random deposition, nonlinear growth, and steady state regime are also depicted.
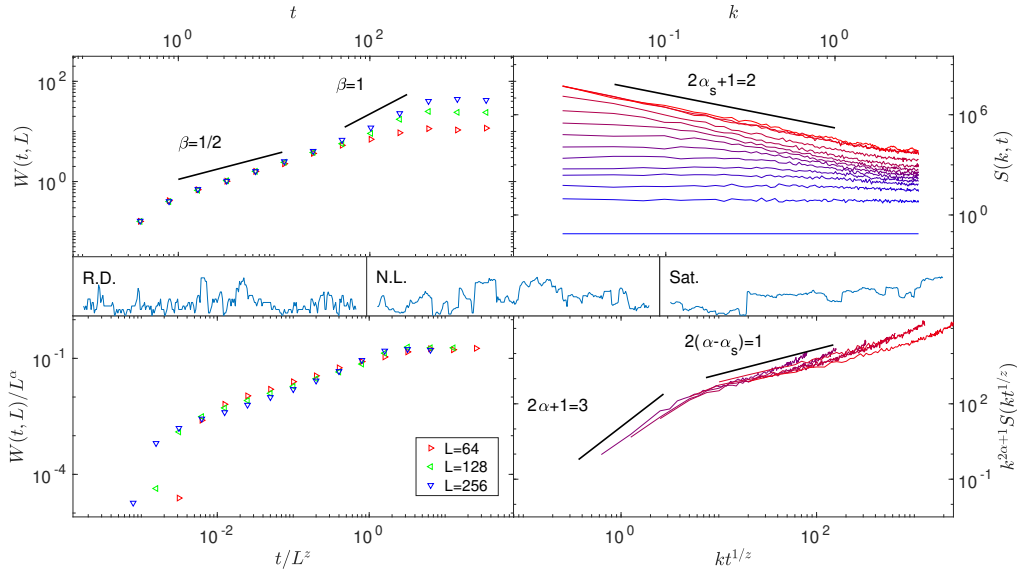
Figure 7.11: *Time evolution for the roughness $W(t,L)$ and the structure factor $S(k,t)$ of the field $h(x,t)$ defined from the solutions of Eq. (7.10) for a 2-dimensional domain. The data collapse for the roughness $W(t,L) = L^\alpha f(t/L^z)$ and structure factor $S(k,t) = k^{-(2\alpha+1)}g(kt^{1/z})$, are also shown. Morphologies $h(x)$ for random deposition (R.D.), nonlinear growth (N.L.) and saturation (Sat.) regimes are depicted.*

In order to assess the full equivalence between this model and the inviscid KPZ equation in terms of universality classes of kinetic roughening, i.e. scaling exponents and fluctuations statistics, the height fluctuations of $h(x)$ have been measured at different times; results are shown in Fig. 7.12. The fluctuations distribution is dis-

Figure 7.12: *Probability density function (PDF) for the height fluctuations* $\chi = (h - \bar{h})/\mathrm{std}(h)$ *over 5000 realizations from GL equation in 2D at critical noise* $D = 0.9 \simeq D_c$ *and* $L = 128$ *for* $t = 1600$ *(left) and* $t = 200$ *(right).*
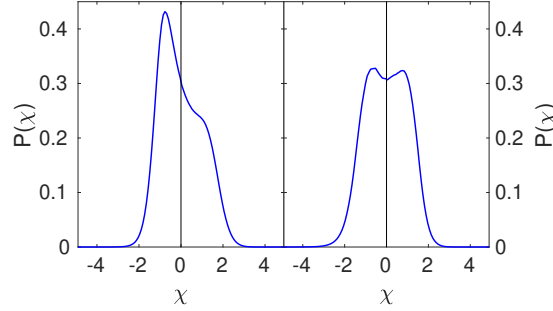
torted by the Dirichlet and Neumann boundary conditions (at the bottom and the top, respectively, in Fig. 7.9). At short times, when some parts of the height profile are close to the bottom (Dirichlet) boundary, the negative range of fluctuations become over-represented. At longer times, the approach to the upper (Neumann) boundary appears to induce a second over-representation, now for a positive range of fluctuations. To avoid this effect as much as possible, for the construction of the fluctuation histograms we have discarded morphologies in which the upper part of the $h(x)$ field touches the upper boundary of the domain. This makes us reject noise realizations very easily, requiring a large number of runs to assess the system behavior at moderate and long times. In spite of these rejections, this effect still seems to play an important role in the shape of the fluctuation PDF for this system size, as seen in Fig. 7.12. We expect much larger system sizes to permit avoidance of these boundary effects; however, this would be very intensive in computational resources, both in terms of memory and processing.

In order to further illustrate the interplay of the morphology with both boundary conditions, we show in Fig. 7.13 the time evolution of the mean value of h, as well as some morphologies $h(x)$ at different times, both in the growth regime and at saturation to steady state. We identify only a narrow interval of t (from t_2 to t_3, approximately) for which $\bar{h} \pm \mathrm{std}(h)$ is close to no system boundary. However, as seen in the depicted morphologies $h(x, t_2)$ and $h(x, t_3)$, there are still realizations for which some parts of the surface $h(x)$ are close to the top and/or bottom boundaries, influencing the shape of the fluctuation PDF.
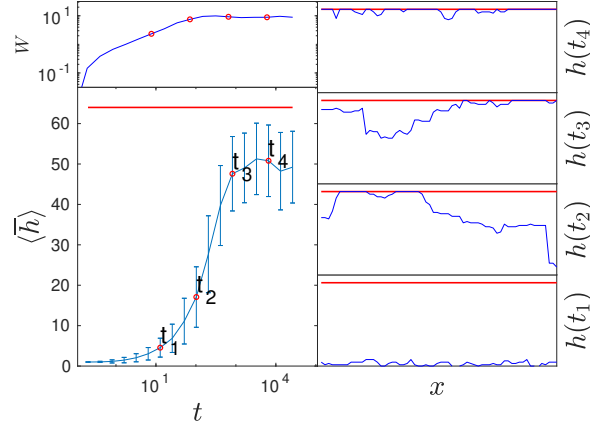
Figure 7.13: Time evolution of the average height profile h over 100 realizations from numerical solutions of the GL equation (left bottom panel) compared to the maximum height achievable (domain lateral size, red solid line). Error bars correspond to the roughness of the front for each time. Left top panel shows the corresponding evolution of the height roughness $W(t)$. One realization of the $h(x,t)$ morphology for each one of the highlighted times, t_1 to t_4, in the left panels is shown in the right panels.

Multiscaling behavior

In spite of having the same scaling exponents, morphologies in the nonlinear growth regime from the inviscid KPZ (see Fig. 7.6) and from the GL model in 2D (see Fig. 7.11) exhibit quite different shapes to the naked eye, due in particular to the abundance of prominent slopes in the latter. We next assess the PDF of the corresponding slope field $u = \partial_x h$ in Fig. 7.14, where the tails of the PDF decay as a power law $P(\chi) \sim \chi^{-2}$. In [141], this type of slope statistics is shown to imply multiscaling behavior (see a brief description in Chapter 1). Hence, different moments q of the height-difference correlation function, Eq. (1.25), exhibit values of roughness exponent α_q which depend nontrivially on q. In the system studied in [141] (a surface growth model related with isotropic percolation), the slope statistics $P(\chi) \sim \chi^{-2}$ implies $\alpha_q = 1/q$. This seems to be also the case in our numerical simulations, quite accurately for $q > 1$, as shown in Fig. 7.15. This multi-fractal property of the morphologies defined in our GL model is a remarkable qualitative difference between them and the morphologies described by the inviscid KPZ equation, in which the fast decay of the fluctuations in h hinders multi-fractality [141].
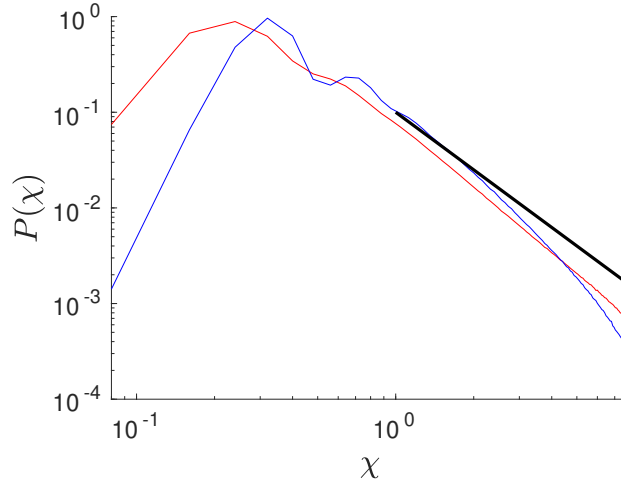
Figure 7.14: *Histogram of slope values [$\chi = (u - \bar{u})/\text{std}(u)$, where for $u = \partial_x h$] from morphologies of the GL growth model within the nonlinear regime identified in Fig. 7.11. Red and blue lines correspond to $L = 128$ and $L = 256$, respectively, while the black solid line is a guide to the eye with slope -2.*
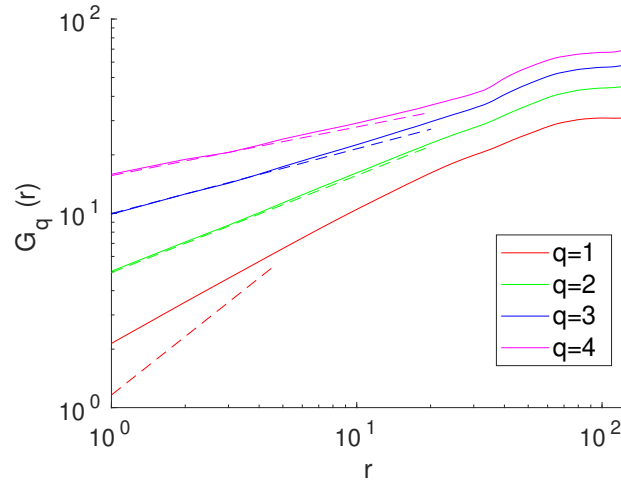
Figure 7.15: *First, second, third and fourth moments (bottom to top) of the height-height correlation function $G_q(x)$ of the surface h from numerical simulations of GL in the nonlinear growth regime identified in Fig. 7.11. Dashed straight lines correspond to the exact value of the slope $1/q$ as predicted in [141].*

Dynamics at $T = T_c$ for a two-dimensional surface

The study of the behavior of the inviscid KPZ equation for 2D substrates was not possible by numerically integrating the inviscid KPZ, Eq. (7.7), directly due to finite-time blow-up behavior, recall Fig. 7.8. We consider here an alternative approach by studying the dynamic behavior of spin configurations in three spatial dimensions which lead to two-dimensional surfaces $h(x, y)$. The noise amplitude that corresponds to the critical temperature in a 3D system is assessed again in analogy to our work for 2D spin domains. From Fig. 7.16, we estimate the critical D to take the value $D_c \simeq 1.25$. Note that the divergence of M at the critical temperature is again in good agreement with the 3D Ising exponents.
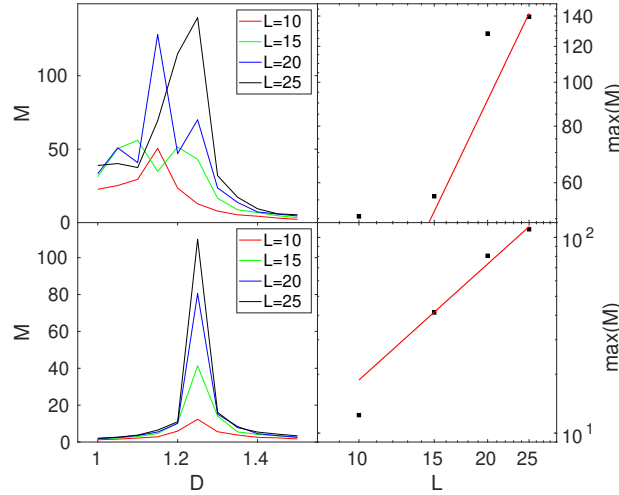
Figure 7.16: *Determination of the noise strength D_c corresponding to the critical temperature T_c for the GL equation in a 3-dimensional domain. Left panels show the magnetization fluctuation M at steady state for different values of D and system lateral size L [magnet boundary conditions (top) and periodic boundary conditions (bottom)]. At $D = D_c$, corresponding to $T = T_c$, M diverges with L as a power law $M \sim L^{1.97}$ (red solid line) as expected from the Ising critical exponents $\gamma \simeq 1.23$ and $\nu \simeq 0.63$ in 3D [140].*

In principle, we can now assess the behavior of the corresponding $h(x, y)$ profiles in terms of their kinetic roughening universality class. The evolution of the field roughness W is depicted for different system lateral sizes in Fig. 7.17. The growth of the roughness is suddenly interrupted and W starts to decay for $t \gtrsim 20$. This behavior is induced by the upper boundary as we can appreciate in Fig. 7.18. The
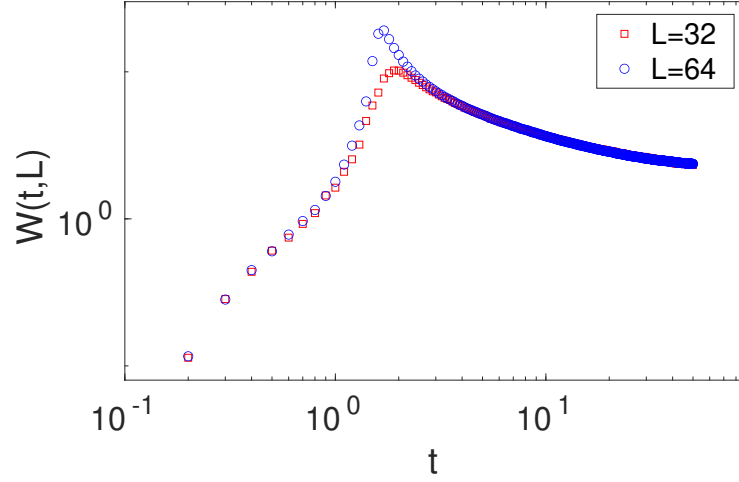
Figure 7.17: Time evolution of the roughness W for the height profiles obtained from numerical solutions of the GL equation Eq. (7.10) in three-dimensional domains with boundary conditions as described in Fig. 7.9, and for different values of the lateral system size L.

mean height $\overline{h}$ suddenly approaches the upper boundary at the same time in which the growth of the roughness is interrupted. For longer times the surface becomes pinned to this boundary, leading to the decrease in the roughness from that time on.
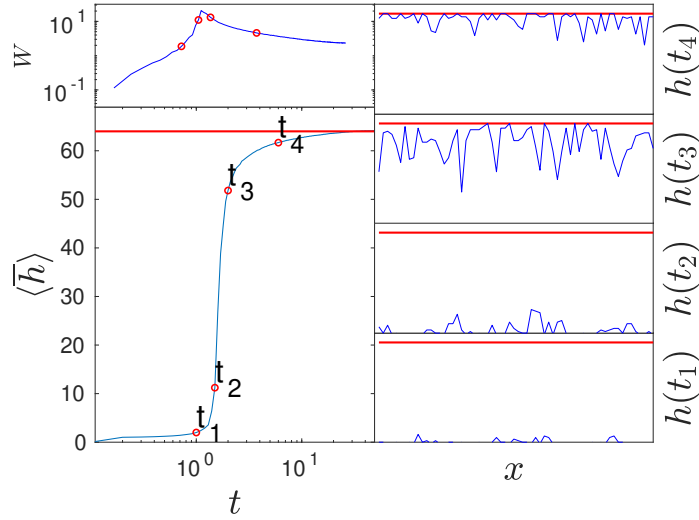
Figure 7.18: *Time evolution of the average height profile h over 10 realizations from numerical solutions of the GL equation Eq. (7.10) (left bottom) compared to the maximum achievable height (domain lateral size, red solid line). Left top panel show the corresponding evolution of the height roughness $W(t)$. One realization of a longitudinal cut $h(x, 1, t)$ for each one of the highlighted times, t_1 to t_4, in the left panels is shown in the right panels.*
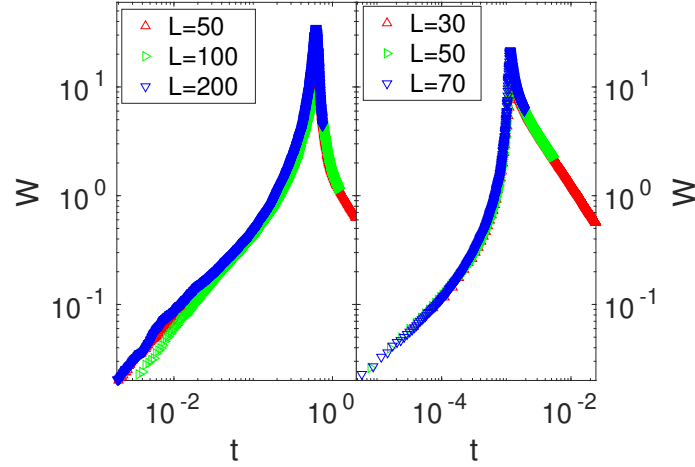
Figure 7.19: Time evolution of the roughness W for the height profiles obtained in the Metropolis evolution of an Ising system in both, two and three-dimensional domains (left and right panels, respectively) with boundary conditions as described in Fig. 7.9 and for different values of the system lateral size L.

7.3.3   Metropolis algorithm

We can alternatively study the dynamical evolution of the spin configurations of a ferromagnetic system using Monte Carlo simulations [142]. A Metropolis algorithm is used here in order to simulate the full evolution of the spin field, while the stationary state was studied in [134] using the Wolff's algorithm. For each Monte Carlo step, one random spin in a position $i, j, (k)$ is chosen and flipped with probability $P_{i,j,(k)}$, such that

$$
P_{i,j,(k)} = \begin{cases} e^{-\Delta E_{i,j,(k)}/T} & \text{if} \quad \Delta E_{i,j,(k)} > 0, \\[2mm] 1/2 & \text{if} \quad \Delta E_{i,j,(k)} = 0, \\[2mm] 1 & \text{if} \quad \Delta E_{i,j,(k)} < 0, \end{cases} \tag{7.12}
$$

where $H[\{s_{i,j,(k)}\}] = J\sum_{i',j',(k')\in\mathcal{N}(i,j,(k))} s_{i',j',(k')}$ is the Hamiltonian [$\mathcal{N}(i, j, (k))$ is the set of all the nearest-neighbours from the position $i, j, (k)$ in the square lattice]. Hence, $\Delta E_{i,j,(k)} = 2Js_{i,j,(k)}\left(\sum_{i',j',(k')\in\mathcal{N}(i,j,(k))} s_{i',j',(k')}\right)$ is the energy change due to the spin flip in the position $i, j, (k)$. The evolution of the field h defined in the same way as in the Ginzburg-Landau approach, i.e. using Eq. (7.9) for both, 2D and 3D

spin lattices, has been measured at $T = T_c$, where $T_c = 2/\ln(1 + \sqrt{2}) \simeq 0.44$ is the exact value for the 2D square lattice and $T_c \simeq 0.22$ for the 3D cubic lattice [134]. The time scale has been set to $t = N/L^d$, where N is the number of Monte Carlo steps.

We find very fast growth of the roughness W with time, as shown in Fig. 7.19 for different lateral sizes L for both 2D and 3D spin domains, hence 1D and 2D surfaces. Such a fast growth process is interrupted when the height approaches the boundary of the system, leading to an abrupt decrease in the roughness from that time on. This behavior is very similar to that found in our Ginzburg-Landau approach to 3D domains. As the GL equation provides a coarse-grained description involving continuum instead of discrete values of the local degrees of freedom, it might be describing effectively larger system sizes with a comparable computational cost.

7.4   Conclusions

In this Chapter we have elucidated novel kinetic roughening behaviors in the *stochastic* KdV equation, both for KPZ and Burgers nonlinearities. A previously unseen random deposition process with saturation, with effective $\alpha = 1/3$, $z = 2/3$ exponents, occurs in the Burgers-like equation, while intrinsic anomaluos scaling takes place in the KPZ-like case. We show both these behaviors also to occur in the *inviscid* Burgers and KPZ equations themselves; hence, the third-derivative term in the stochastic KdV equation is irrelevant to the kinetic roughening behavior, as it does not interact with the amplitude of the fluctuations at any scale.

The intrinsic anomalous scaling found in the inviscid KPZ equation can be interpreted as a counterexample for the conclusion reached in [143] where intrinsic anomalous roughening was argued, via perturbative dynamic renormalization group arguments, not to be compatible with the asymptotic scaling of growth systems with local dynamics, subject to time-dependent noise. These arguments do not apply to the particular case of the inviscid KPZ equation, since the $\nu = 0$ coefficient of the linear term leads to an ill-defined KPZ coupling, $g \propto \lambda^2 D/\nu^3$. As already noted, the inviscid KPZ equation also evades direct conclusions from exact solutions of the KPZ equation, which require a Hopf-Cole transformation involving $1/\nu$ factors. Our numerical work is in this sense a novel approach to this equation for which stable solutions have thus far remained unknown, up to our knowledge.

We also propose potential inviscid Burgers and KPZ universality classes. The fluctuation statistics of both processes exhibit symmetric fluctuations, with an emergent symmetry in the case of Burgers resulting from the $(u, x) \leftrightarrow (-u, -x)$ invari-

ance, as it occurred in the *viscous* stochastic Burgers equations studied in Chapters 4 and 5. However, the symmetric (even if non Gaussian) fluctuations exhibited by the inviscid KPZ equation are due to an even more unexpected symmetry emergence, which can not be explained in terms of a $(h, x) \leftrightarrow (-h, -x)$ invariance.

We have also tried to assess the inviscid KPZ universality class for two-dimensional substrates. To circumvent the finite-time blow-up occurring in the numerical integration of the 2D inviscid KPZ equation, the connection with a surface growth system related with an Ising model has been pursued. An approach via the GL equation seems feasible in the one-dimensional case and has been extended to two-dimensional interfaces. However, the interaction of the effective surface in the spin system with the free boundary does not allow us to follow the long-time evolution in two-dimensional substrates, both for (continuous) GL or (discrete) Metropolis dynamics. Either much larger systems (involving a huge computational cost) or some alternative approach would be necessary in order to determine the behavior of the inviscid KPZ universality class for dimensions higher than one, if at all possible.

Chapter 8

Ordered pattern formation in untrathin ferrofluid films

8.1 Introduction

Recent advances in thin film production have considered the manipulation of thin fluid films by means of external magnetic or electric fields in order to produce ordered patterns. Such type of morphologies are very well known to form in ferrofluids, which are colloidal suspensions of magnetic nanoparticles that react to magnetic forces, both at macroscopic and microscopic scales, when a magnetic field is applied which is intense enough, as depicted in Figure 8.1. However, there are no experimental evidences of this type of ordered patterns at the nanoscale in the literature.
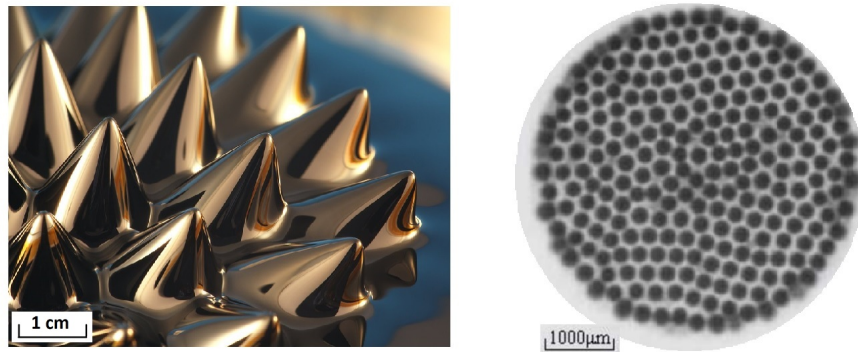

Figure 8.1: Pattern formation in both macro [144] and microscopic [47] ferrofluid films.

The morphological instability that leads to the formation of patterns in ferrofluid films under a magnetic field was described by Rosensweig [48, 5] and is known as Rosensweig instability (see Chapter 2 for further details). Linear stability analysis of the hydrodynamic problem considering a thick and inertial ($\mathrm{Re} \gg 1$) film lead to a dispersion relation which presents a narrow band of unstable modes for large enough magnetic field intensity (type-I instability, see [145]) that predicted the formation of a highly-ordered hexagonal pattern. Based on Rosensweig's work, Abou et al [64] carried out a linear stability analysis of the full Navier-Stokes and Maxwell equation system in four different asymptotic regimes, combining the prevalence of viscous vs inertial forces ($\mathrm{Re} \ll 1$ vs $\mathrm{Re} \gg 1$) and the thin vs thick limits for the film depth. For a thin and viscous film (the case of interest for our work), the dispersion relation does also exhibit a narrow band of unstable modes, hence an ordered pattern was also expected.

Some interfacial effective evolution equations describing the dynamics of the surface of thin/ultrathin ferrofluid films under a magnetic field, which provide a useful tool in the assessment of the pattern formation processes beyond the linear regime, were published several years later [146, 147]. Despite the preliminar prediction of the presence of a narrow band of unstable modes in ferrofluid thin viscous films assessed in [64], the effective equations derived in these works do not predict a narrow band of unstable modes in the ultrathin limit. In this Chapter, we deepen the study of ferrofluids as a paradigmatic case of ordered pattern formation in thin fluid films, by deriving an effective evolution equation and assessing the conditions under which ordered and disordered patterns of drops can be obtained at the nanoscale, i.e. when the fluid film is *ultra*thin. This study is a proof of concept about the theoretical viability of ordered patterns of ferrofluid drops at the nanoscale achieved by selecting materials (ferrofluid and substrate) with suitable physical properties and tuning the external magnetic field. The level of order achieved in the drop formation induced by an external magnetic field is assessed under different scenarios involving several types of interactions between the ferrofluid and the substrate (i.e. different types of disjoining pressure or interface potentials). The scenarios for which a high level of spatial order is predicted by the linear dispersion relation of the evolution equation exhibit appreciably better ordered drops at steady state than those for which the dispersion relation has a wide band of unstable Fourier modes.

8.2   Interfacial equations for thin ferrofluid films: state of the art

The most conspicuous interfacial equations derived for thin ferrofluid films proposed in the literature are described in this section. We next consider the reasons why they are, however, not suitable for the prediction of ordered patterns in ultrathin ferrofluid films.

8.2.1   SAK model

The thin film model proposed by Seric, Afkhami, and Kondic (SAK) in [146] is consistent with an ultrathin film as a disjoining pressure (specifically, a spinodal dewetting potential) is explicitly considered, together with the magnetic field interaction with the ferrofluid, and surface tension. The Re = 0 approximation, congruent with the *ultra*thin condition, is also made in [146], leading to negligible gravity effects. The evolution equation obtained has the form

$$\partial_t h = -\partial_x \left(\frac{h^3}{3} \partial_x (A\Pi(h) + Bh + C\partial_x^2 h) \right), \qquad (8.1)$$

where A, B, and C are physical constants related to the disjoining pressure, magnetic field, and surface tension interactions, respectively. Linear stability analysis gives a dispersion relation of the form

$$\omega = \frac{h_0^3}{3} \left(A(\Pi'(h_0) + B)k^2 - Ck^4 \right), \qquad (8.2)$$

where a destabilizing $\sim k^2$ term is obtained due to both the disjoining pressure and to the magnetic field, and the stabilizing $\sim -k^4$ term is generated by surface tension. Notice that, according to this linear dispersion relation, a disordered pattern is expected (perturbations with very large wavelengths are unstable [43]), hence this model is not compatible with the formation of an ordered drop pattern.

8.2.2   Conroy-Matar model

The second case found in the literature [147] describes a thin ferrofluid film falling down an inclined plane under the action of an external magnetic field. Being proposed for macroscopically thin films, it *(i)* does not take into account the effect of the

disjoining pressure and *(ii)* does not consider the Reynolds number to be negligible, in contrast to the model by Seric *et al.* The following evolution equation is derived,

$$\partial_t h = -\partial_x \left(\frac{h^3}{3} \left(G + \partial_x[B\Omega + C\partial_x^2 h - G'h] \right) \right),$$ (8.3)

where B, C, G, and G' are physical constants related to the magnetic field, surface tension, and inertial (G, G') contributions, respectively, and Ω is an effective magnetic pressure; we will provide additional details in the derivation of the ferrofluid film equation discussed in the next section. The linear dispersion relation reads

$$\omega = \frac{h_0^3}{3} \left(-G'k^2 + B \left(1 - \frac{1}{2 + \beta\xi|k|/3} \right) |k|^3 - Ck^4 \right),$$ (8.4)

where β and ξ describe magnetic properties of the ferrofluid (see also more details in the full derivation assessed in the next section).

In the particular case of a ferrofluid with a very large magnetic permeability, Conroy and Matar [147] derive a simplified interface equation, which is virtually identical to a previously-known model of an electrically perfectly conducting fluid film under an external *electric* field [148]. It reads

$$\partial_t h = -\partial_x \left(\frac{h^3}{3} \left[G + \partial_x(B\mathcal{H}[\partial_x h] + C\partial_x^2 h - G'h) \right] \right),$$ (8.5)

where $\mathcal{H}[\cdot]$ is the Hilbert transform. A very similar evolution equation is also derived [150] in the modeling of the formation and coarsening dynamics of islands in a strained epitaxial semiconductor film. In the present case, the linear stability analysis yields a dispersion relation of the form

$$\omega = \frac{h_0^3}{3}(-G'k^2 + B|k|^3 - Ck^4),$$ (8.6)

where the destabilizing $\sim |k|^3$ term comes from the magnetic field contribution, the stabilizing $\sim -k^4$ term comes again from surface tension, and the stabilizing $\sim -k^2$ term comes from gravity. According to this linear dispersion relation, a narrow band of unstable modes can occur, hence ordered patterns could form. However, as the disjoining pressure is not taken into account, this evolution equation could be questioned for ultrathin films for which the interaction with gravity is negligible, while the interaction with the substrate becomes relevant and should be considered in the physical derivation.

Numerical solutions of the full Eq. (8.3) are provided in [147], while they are not reported for the reduced Eq. (8.5). However, the latter equation has been demonstrated to exhibit numerical blow-up [148], hence the full magnetic term in Eq. (8.3) must be considered in the derivation of physical models to assess the dynamics beyond the linear approximation.

The different boundary conditions considered for the Maxwell equations for the magnetic field explain the difference between the magnetic field contribution terms in the effective equations (8.1) and (8.3) (which lead to contributions for the linear dispersion relation of orders k^2 and $|k|^3$ in equations (8.2) and (8.4), (8.6), respectively). In [146], the magnetic potential value is fixed both at the substrate-fluid interface and at a parallel upper plane. In [147], the derivative of the magnetic potential (vertical component of the magnetic field) at $y = \pm\infty$ is fixed to have the value of the external magnetic field. We consider this second condition, namely, a constant value for the magnetic field far from the ferrofluid film, more realistic for an actual physical experiment. Furthermore, in an ultrathin fluid film, the cancellation of the inertial terms ($G' = 0$) and the consideration of the disjoining pressure ($\sim k^2$ in the dispersion relation) make a destabilizing $\sim |k|^3$ term capable to induce a narrow band of unstable modes in the dispersion relation, while a destabilizing $\sim k^2$ term could not induce it. For the purpose of this Chapter, we derive a thin film model for a ferrofluid ultrathin film based on the physical model in [147], Eq. (8.3), but considering *(i)* a horizontal substrate, *(ii)* a negligible Re = 0, and *(iii)* a disjoining pressure contribution to the film dynamics.

8.3   Ultrathin ferrofluid film equation

A viscous ultrathin (Re = 0) ferrofluid film over a flat ($\theta = 0$) solid substrate, with which the fluid interacts by means of a disjoining pressure, is considered next, as sketched in Figure 8.2. In this Chapter, we present the physical laws that govern this system, as well as the mathematical derivation and approximations required in order to obtain a novel evolution equation for the thickness of the film.

Hydrodinamic equations

The evolution equation for the ferrofluid film interface is derived from the same set of hydrodinamic equations (mass balance and Navier-Stokes equations) as in Chapter 2. Here the stress tensor, which includes the disjoining pressure and magnetic
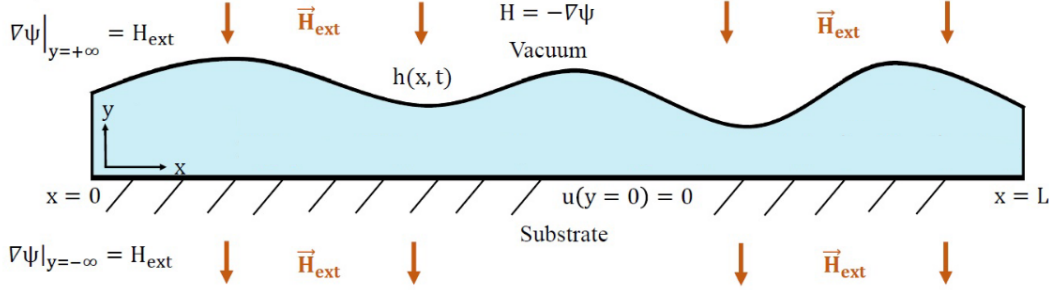
Figure 8.2: The thin ferrofluid film.

contributions, takes the form

$$
\mathcal{T} = \mathcal{T}^f + \mathcal{T}^m, \qquad \mathcal{T}^m = \begin{pmatrix} B_x H_x - \frac{\mu_0}{2}|\vec{H}|^2 & B_x H_y \\ B_y H_x & B_y H_y - \frac{\mu_0}{2}|\vec{H}|^2 \end{pmatrix}, \qquad (8.7)
$$

where T^f is the hydrodynamic contribution to the stress tensor as in Eq. (2.7), and $\vec{H} = (H_x, H_y)$ and $\vec{B} = (B_x, B_y)$ are the magnetic field and induction, respectively, such that $\vec{B} = \mu_0(\vec{H} + \vec{M})$. Here the magnetization $\vec{M}$ is null for both the air and substrate, and we consider a Langevin form

$$
\vec{M}(\vec{H}) = M_s \left(\coth(\xi|\vec{H}|) - \frac{1}{\xi|\vec{H}|} \right) \frac{\vec{H}}{|\vec{H}|}. \qquad (8.8)
$$

Here, $\xi = 3\chi_0/M_s$, with M_s being the saturation magnetization value and χ_0 being the initial magnetic susceptibility for the ferrofluid.

As there are no electric currents, Ampere's law $\nabla \times \vec{H} = 0$ holds, hence the magnetic field is irrotational and scalar magnetic potentials ψ^i can be defined for each medium (air, ferrofluid, and substrate) such that $\vec{H^i} = -\nabla\psi^i$ for $i = a, f, s$ respectively. Furthermore, the continuity of both the magnetic field and the magnetic induction fields require the $||\vec{B} \cdot \vec{n}|| = 0$ and $||\vec{H} \cdot \vec{t}|| = 0$ jump boundary conditions at both interfaces [147].

The effective pressure p_{eff} for the Navier-Stockes equation is a combination of the hydrostatic p and the magnetic Ω pressures, which takes the form

$$
p_{eff} = p + \Omega, \qquad \Omega = \mu_0 \int_0^{\vec{H}} M(|\vec{H}|') \, d|\vec{H}|' = -\frac{M_s}{\xi} \ln\left(\frac{\xi|\vec{H}|}{\sinh(\xi|\vec{H}|)} \right), \qquad (8.9)
$$

as the fluid is considered to be incompressible.

Consider the average thickness of the liquid layer h_0 as a typical length scale, $w_0 = \rho g h_0^2/2\mu$ as a velocity scale, w_0/h_0 as a time scale, $\mu w_0/h_0$ as a representative scale for pressure and stress, the magnitude of the external magnetic field $|\vec{H}_{ext}|$ as a magnetic field scale, and we introduce a small parameter $\epsilon = h_0/L$ and the new variables $x' = \epsilon x$, $t' = \epsilon t$, and $v' = v/\epsilon$. In such rescaled variables, the momentum balance equations and the surface boundary conditions $||\vec{n}\,\mathcal{T}\,\vec{n}|| = \gamma\mathcal{C}$ and $||\vec{n}\,\mathcal{T}\,\vec{t}|| = 0$ become, respectively,

$$0 = \epsilon^2 u_{x'x'} + u_{yy} - \epsilon(p+\Omega)_{x'}, \tag{8.10}$$

$$0 = \epsilon^3 v'_{x'x'} + \epsilon v'_{yy} - (p+\Omega)_y - 2, \tag{8.11}$$

$$p + \Pi + \frac{2H_{ext}^2}{\rho g h_0}\left(\partial_y \psi^a|_h\right)^2 + \mathcal{O}(\epsilon^2) =$$

$$= \frac{\epsilon^2 h_{x'}^2 (2\epsilon u_{x'}) - \epsilon h_{x'}[2(u_y + \epsilon^2 v'_{x'})] + 2\epsilon v'_y}{1 + \epsilon^2 h_{x'}^2} - \frac{1}{\epsilon \mathrm{Ca}''}h_{x'x'}, \tag{8.12}$$

$$0 = -\epsilon^2 h_{x'}^2 (u_y + \epsilon^2 v'_{x'}) + \epsilon^2 h_{x'}[2(v'_y - u_{x'})] + u_y + \epsilon^2 v'_{x'}. \tag{8.13}$$

We consider for convenience that the capillarity number $\mathrm{Ca} = \mu w_0/\gamma$ is $\mathcal{O}(\epsilon^3)$ [147] and define $\mathrm{Ca}'' = \mathrm{Ca}/\epsilon^3$, which is $\mathcal{O}(1)$. We also expand again $u = u_0 + \epsilon u_1 + \mathcal{O}(\epsilon^2)$, $v' = v'_0 + \epsilon v'_1 + \mathcal{O}(\epsilon^2)$ and $p = p_0 + \epsilon p_1 + \mathcal{O}(\epsilon^2)$, and consider a flat surface, hence $u_0 = 2\sin\theta\left(hy - \frac{y^2}{2}\right) = 0$. The u contribution at $\mathcal{O}(\epsilon)$ becomes

$$u_1 = -p_{0x'}\left(hy - \frac{y^2}{2}\right). \tag{8.14}$$

The p_0 contribution can be obtained from Eq. 8.11 at $\mathcal{O}(1)$, $(p_0+\Omega)_y = -2$, with $p_0 = -h_{x'x'}/\epsilon\mathrm{Ca}'' - \Pi - \frac{2H_{ext}^2}{\rho g h_0}\left(\partial_y \psi^a|_h\right)^2$ as the boundary condition at the fluid surface. We consider both the disjoining pressure Π and the quotient $2H_{ext}^2/\rho g h_0$ to be $\mathcal{O}(\epsilon^{-1})$ and define $\Pi' = \epsilon\Pi$ and $Q = \epsilon 2H_{ext}^2/\rho g h_0$ to be $\mathcal{O}(1)$. Hence, we obtain $p_0 = 2(h-y) - h_{x'x'}/\epsilon\mathrm{Ca}'' - \Pi'/\epsilon - Q\left(\partial_y \psi^a|_h\right)^2/\epsilon - Q\Omega/\epsilon$.

Magnetic contributions to the surface boundary condition

The contribution of the magnetic tensor to the $||\vec{n}\,\mathcal{T}\,\vec{n}||$ product, taking into account that $\vec{B}^a \cdot \vec{n} = \vec{B}^f \cdot \vec{n}$, is

$$||\vec{n}\mathcal{T}^m\vec{n}|| = \vec{n}\mathcal{T}^{am}\vec{n} - \vec{n}\mathcal{T}^{fm}\vec{n} = \vec{n}(B^a H^{at} - B^f H^{ft})\vec{n} + \frac{\mu_0}{2}(H^{f2} - H^{a2}) =$$

$$= \vec{n}\vec{B}^a(H^{at} - H^{ft})\vec{n} + \frac{\mu_0}{2}(H^{f2} - H^{a2}) = \tag{8.15}$$

(considering that $\vec{H^a} \cdot \vec{t} = \vec{H^f} \cdot \vec{t}$, one has that $H^{f2} - H^{a2} = (\vec{H^a} \cdot \vec{n})^2 - (\vec{H^f} \cdot \vec{n})^2$ and $B^a = \mu_0 H^a$)

$$= \mu_0 \left[(\vec{H^a} \cdot \vec{n})^2 - (\vec{n} \cdot \vec{H^a})(\vec{H^f} \cdot \vec{n}) + \frac{1}{2}(\vec{H^f} \cdot \vec{n})^2 \right] - \frac{1}{2}(\vec{H^a} \cdot \vec{n})^2 =$$

$$= \frac{\mu_0}{2}(\vec{H^a} \cdot \vec{n} - \vec{H^f} \cdot \vec{n})^2 = \frac{\mu_0}{2}(\vec{H^a} \cdot \vec{n})^2. \tag{8.16}$$

In terms of the magnetic scalar potential,

$$\frac{\mu_0}{2}(\vec{H^a} \cdot \vec{n})^2 = \frac{\mu_0}{2} \left(\begin{pmatrix} \epsilon\partial_x\psi^a, & \partial_y\psi^a \end{pmatrix} \begin{pmatrix} -\epsilon\partial_x h \\ 1 \end{pmatrix} \right)^2 = (\partial_y\psi^a)^2 + \mathcal{O}(\epsilon^2). \tag{8.17}$$

Magnetic equations

Here we take L as the x scale, h_0 as the y scale for the fluid, *but* L also as the y scale for air and substrate. We consider $\epsilon = h_0/L \ll 1$ to be very small.

The magnetic Gauss' law $\nabla \cdot \vec{B} = 0$ holds. The magnetic induction $\vec{B}$ is given by $\vec{B} = \mu_0(\vec{H} + \vec{M})$, with $\vec{M} = 0$ for the air and substrate, and $\vec{M} = \beta F(|\vec{H}|)\vec{H}$ for the ferrofluid [F is as in Eq. (8.8) and it is considered to be $\mathcal{O}(\epsilon^{-1})$ so we define $F' = \epsilon F$ to be $\mathcal{O}(1)$], hence Gauss' law in air (a), substrate (s) and fluid (f) can be rewritten, respectively, as

$$\mu_0 \left(\partial_x^2\psi^a + \partial_y^2\psi^a \right) = 0, \qquad \mu_0 \left(\partial_x^2\psi^s + \partial_y^2\psi^s \right) = 0,$$

$$\mu_0 \left(\partial_y((1 + \epsilon^{-1}\beta F')\partial_y\psi^f) + \epsilon^2\partial_x((1 + \epsilon^{-1}\beta F')\partial_x\psi^f) \right) = 0. \tag{8.18}$$

Furthermore, the $||\vec{B}\cdot\vec{n}|| = 0$ and $||\vec{H}\cdot\vec{t}|| = 0$ jump boundary conditions are requested at both interfaces for the magnetic induction and the magnetic field, respectively [147], leading to

$$(1 + \epsilon^{-1}\beta F)(\partial_y\psi^f - \epsilon^2\partial_x h \, \partial_x\psi^f) = \epsilon\partial_y\psi^a - \epsilon^2\partial_x h \, \partial_x\psi^a,$$

$$\partial_x h \, \partial_y\psi^f + \partial_x\psi^f = \epsilon\partial_x h \, \partial_y\psi^a + \partial_x\psi^a, \tag{8.19}$$

for the fluid-air interface $(y = h)$ and

$$(1 + \epsilon^{-1}\beta F)\partial_y\psi^f = \epsilon\partial_y\psi^s, \qquad \psi^f = \psi^s, \tag{8.20}$$

for the fluid-substrate interface $(y = 0)$.

For the computation of ψ^a, we define Ψ^a such that $\partial_y \psi^a = \partial_y \Psi^a + H_{ext}$, hence

$$\partial_x^2 \Psi^a + \partial_y^2 \Psi^a = 0, \qquad \lim_{y \to \infty} \partial_y \Psi^a = 0. \tag{8.21}$$

After Fourier transforming in the x-coordinate, the solutions of $\partial_y^2 \widehat{\Psi^a} = k^2 \widehat{\Psi^a}$ take the form $\widehat{\Psi^a} = C_1 e^{-|k|y} + C_2 e^{|k|y}$. As $\partial_y \widehat{\Psi^a} \to 0$ when $y \to \infty$, then C_2 must be 0. The constant C_1 is evaluated to assure the continuity of the magnetic potential. If we fix arbitrarily the potential Ψ^a to be 0 for $y = 0$,

$$\psi^f = \psi^a(h) = \Psi^a(h) + H_{ext}h \quad \Rightarrow \quad \widehat{\Psi^a} = (\widehat{\psi^f} - H_{ext}\widehat{h})e^{-|k|y}. \tag{8.22}$$

Finally, considering h to be $\mathcal{O}(\epsilon)$, we can evaluate $\partial_y \Psi^a(h)$ as

$$\partial_y \Psi^a(h) = \mathcal{F}^{-1}\left(-|k|(\widehat{\psi^f} - H_{ext}\widehat{h})e^{-|k|h}\right) \simeq \frac{1}{2\pi} \int_{-\infty}^{\infty} -|k|(\widehat{\psi^f} - H_{ext}\widehat{h})e^{ikx}dk. \tag{8.23}$$

Analogously, we compute ψ^s by defining Ψ^s such that $\partial_y \psi^s = \partial_y \Psi^s + H_{ext}$, hence

$$\partial_x^2 \Psi^s + \partial_y^2 \Psi^s = 0, \qquad \lim_{y \to -\infty} \partial_y \Psi^s = 0. \tag{8.24}$$

Here, $\widehat{\Psi^s} = (\psi^f + H_{ext})e^{|k|y}$ and

$$\partial_y \Psi^s(0) = \frac{1}{2\pi} \int_{-\infty}^{\infty} |k|(\widehat{\psi^f} + H_{ext})e^{ikx}dk. \tag{8.25}$$

For the computation of ψ^f, we expand $\psi^f = \psi_0^f + \epsilon^2 \psi_1^f + \mathcal{O}(\epsilon^4)$ and solve Gauss' equation at leading order $\mathcal{O}(\epsilon^{-1})$,

$$\partial_y(\beta F' \partial_y \psi_0^f) = 0, \tag{8.26}$$

hence $\beta F' \partial_y \psi_0^f = f(x)$ where $f(x) = 0$ from the boundary conditions. Integrating again $\psi_0^f = \psi_0^f(x)$ (hence F' does only depend on x at leading order), which is computed from Gauss' equation at next order in ϵ, i.e.,

$$F' \partial_y^2 \psi_1^f + \partial_x(F' \partial_x \psi_0^f) = 0 \quad \Rightarrow \quad \partial_y^2 \psi_1^f = -\frac{1}{F'} \partial_x(F' \partial_x \psi_0^f), \tag{8.27}$$

subject to

$$\beta F'(\partial_y \psi_1^f(h) - \partial_x h \, \partial_x \psi_0^f) = \partial_y \psi^a(h), \qquad \beta F' \partial_y \psi_1^f(0) = \partial_y \psi^s(0). \tag{8.28}$$

Integrating Eq. (8.27) once with respect to y between $y = 0$ and $y = h$, we get

$$\partial_y \psi_1^f(h) - \partial_y \psi_1^f(0) = \partial_x h \; \partial_x \psi_0^f + \frac{\partial_y \psi^a(h)}{\beta F'} - \frac{\partial_y \psi^s(0)}{\beta F'} = -\frac{1}{F'} \partial_x(F' \partial_x \psi_0^f) h. \quad (8.29)$$

In Fourier space, using Eqs. (8.23) and (8.25), we finally obtain an integral equation for the computation of $\psi_0^f(x)$,

$$\frac{1}{2\pi} \int_{-\infty}^{\infty} |k|(H_{ext}\hat{h} - 2\hat{\psi}_0^f)e^{-ikx}dk = -\beta F' \left(\frac{1}{F'} \partial_x(F' \partial_x \psi_0^f)h + \partial_x h \; \partial_x \psi_0^f \right). \quad (8.30)$$

Interface equation

Finally, mass balance reads $h_t + \left(\int_0^h \epsilon u_1 \, dy \right)_x = 0$, hence

$$\partial_t h = \partial_x \left[\frac{h^3}{3} \partial_x \left(-\frac{\partial_x^2 h}{Ca''} - \Pi' - Q \left(\partial_y \psi^a|_h \right)^2 - Q\Omega \right) \right] + \mathcal{O}(\epsilon). \quad (8.31)$$

The $\left(\partial_y \psi^a|_h \right)^2$ term appearing in this equation can be evaluated from

$$\left(\partial_y \Psi^a + H_{ext}|_h \right)^2 \simeq H_{ext}^2 + 2H_{ext}\partial_y \Psi^a|_h \quad (8.32)$$

if we consider that the magnitude of the external field H_{ext} is much larger than the induced $\partial_y \Psi^a|_h$. Finally, the interface evolution equation for the ferrofluid thin film at leading order takes the form

$$\partial_t h = \partial_x \left\{ \frac{h^3}{3} \partial_x \left[Q \left(\frac{H_{ext}}{\pi} \int_{-\infty}^{\infty} |k|(\widehat{\psi^f} - H_{ext}\widehat{h})e^{ikx}dk - \Omega \right) - \frac{\partial_x^2 h}{Ca''} - \Pi' \right] \right\}, \quad (8.33)$$

where $\hat{\psi}^f$, at leading order in ϵ, is computed from

$$\frac{1}{2\pi} \int_{-\infty}^{\infty} |k|(H_{ext}\hat{h} - 2\hat{\psi}_0^f)e^{-ikx}dk = -\beta F' \left(\frac{1}{F'} \partial_x(F' \partial_x \psi_0^f)h + \partial_x h \; \partial_x \psi_0^f \right). \quad (8.34)$$

Equations (8.33) and (8.34) coincide with the model obtained in [147] [see Eq. (8.3)] if the inertial contributions are neglected and a new contribution for the disjoining pressure is allowed for. The behavior of equations (8.33) and (8.34) in terms of pattern formation is expected to depend on the form of the disjoining pressure potential (unstable, stable, or metastable, see Chapter 2). We assess that dependence via a linear stability analysis.

Linear stability analysis

Next, we consider small variations of, both, $h = h_0 + \tilde{h}e^{\omega t + ikx}$ and $\psi^f = \psi^f_b + \tilde{\psi}^f e^{ikx}$, in order to assess the linear behavior of Eq. (8.33). For a single mode (omitting tildes), Eq. (8.34) reduces to

$$|k|(H_{ext}h - 2\psi^f) = -\beta \left(\partial_x (F' \partial_x \psi^f) h + \partial_x h' \partial_x \psi^f \right), \qquad (8.35)$$

which at leading order in small variations, and Taylor expanding F' at leading order, reduces to

$$|k|(H_{ext}h - 2\psi^f) = \frac{\beta \xi \psi^f k^2 h_0}{3} \quad \Rightarrow \quad \psi^f = \frac{H_{ext}}{2 + \beta \xi h_0 |k|/3} h. \qquad (8.36)$$

Hence, the linear dispersion relation takes the form

$$\omega(k) = \frac{h_0^3}{3} \left[\Pi'(h_0)k^2 - \frac{1}{Ca''}k^4 + 2QH_{ext} \left(1 - \frac{H_{ext}}{2 + \beta \xi h_0 |k|/3} \right) |k|^3 \right]. \qquad (8.37)$$

The contributions of this dispersion relation allow for a narrow band of unstable modes when $\Pi'(h_0) < 0$ (see e.g. the metastable scenario in Fig. 8.3, in which a narrow band of unstable modes are obtained under proper parameter conditions) as the equivalent dispersion relation for the full model in [147] did; however, in the latter it was due to the gravity $\sim -k^2$ contribution, which is neglected if the film is considered to be ultrathin ($Re = 0$).

The behavior beyond the linear approximation will be numerically assessed in the next section, focusing on the level of order of the drop patterns formed at steady state.

8.4   Simulation results

Numerical simulations of Eq. (8.33) have been carried out in order to study its nonlinear behavior, by means of the numerical scheme described in Chapter 3, namely, a mixed implicit-explicit method, in which the term with the highest-order derivative is treated implicitly and the remaining terms are treated explicitly. In the case of the magnetic field term, the numerical treatment is implemented by means of a pseudospectral method, while ψ^f is computed by an iterative fixed point method from Eq. (8.34).

In order to determine if narrow or wide bands of unstable Fourier modes in the dispersion relation lead to more or less ordered patterns of drops, respectively, we

will consider stable, metastable, and null disjoining pressure potentials based on the models proposed in [61] (see Chapter 2 for more details). The functional dependence of Π with the field height h has been considered of the form

$$\Pi_u(h) = A\left(\frac{c_1}{h^2} - \frac{c_2}{h^3}\right), \tag{8.38}$$

$$\Pi_m(h) = A\left(-\frac{c_3}{(h + c_4)^2} + \frac{c_5}{h^2} - \frac{c_6}{h^3}\right), \tag{8.39}$$

as unstable and metastable scenarios, respectively. Here the parameter values are $c_1 = c_5 = 1$, $c_2 = 0.15$, $c_3 = 15$, $c_4 = 0.5$, and $c_6 = 0.05$.
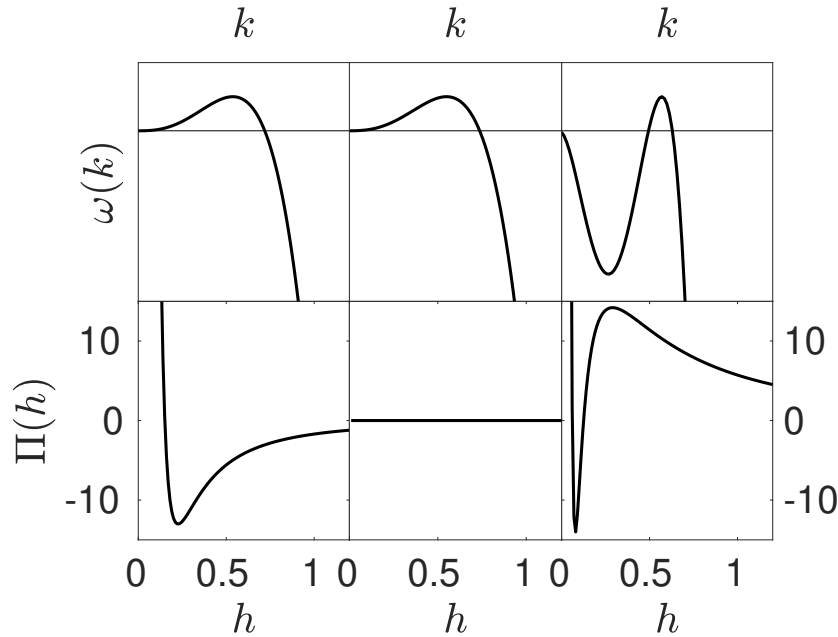

Figure 8.3: Linear dispersion relation $\omega(k)$ (top panels) of equation (8.37) for the selected parameters in numerical simulations considering the different types of disjoining pressure potentials [as in Eqs. (8.38)-(8.39)] depicted in the bottom panels (unstable, null, and metastable disjoining pressure, respectively, from left to right).

Periodic boundary conditions have been considered and averages over random initial conditions $h(x, 0) = 1 + \eta$, where $\langle \eta(x) \rangle = 0$ and $\langle \eta(x_1)\eta(x_2) \rangle = 0.05\delta(x_1 - x_2)$, have been carried out. In all simulations, $\beta = \xi = 1$. A system size value $L = 1024$

is considered, where the discretization steps are $\delta x = 1$ and $\delta t = 0.5$. Parameters governing the disjoining pressure (A), the magnetic field ($B = QH_{ext}/\pi$), and the surface tension ($C = 1/\mathrm{Ca}''$) have been selected by sweeping the parameter space looking for values such that the most unstable mode corresponds as close as possible to 40 drops [$k \simeq 2\pi/(1024/40)$]. A representative example of these drop profiles is depicted in Fig. 8.4. In the metastable case, parameters have been chosen such that this mode is the only unstable one. In Figs. 8.5-8.7 we display both the morphology $h(x)$ and the structure factor $S(k)$ at several times for no disjoining pressure (Fig. 8.5), unstable potential (Fig. 8.6), and metastable potential (Fig. 8.7), respectively. Drops stabilize into a steady state in all cases. This stabilization becomes evident in the evolution of the surface roughness W, which is depicted in the top panels of Figs. 8.5-8.7. Each one of these drops exhibits a similar characteristic form, which makes the drop pattern a discontinuous periodic geometry, hence the envelope of the structure factor $S(k)$ at high values of k follows quite closely a power law (in these cases, $S(k) \sim k^{-4}$), as is frequently the case for these type of periodic geometric patterns [151]. Different levels of order are achieved for different types of disjoining pressure potentials. This spatial order level is measured by assessing the distribution of the heights of the drops (height of each drop at its maximum), the distance between the drops (distance between two consecutive drop maximums), the width of the drops, and the separation between the drops, as defined in Fig. 8.4.
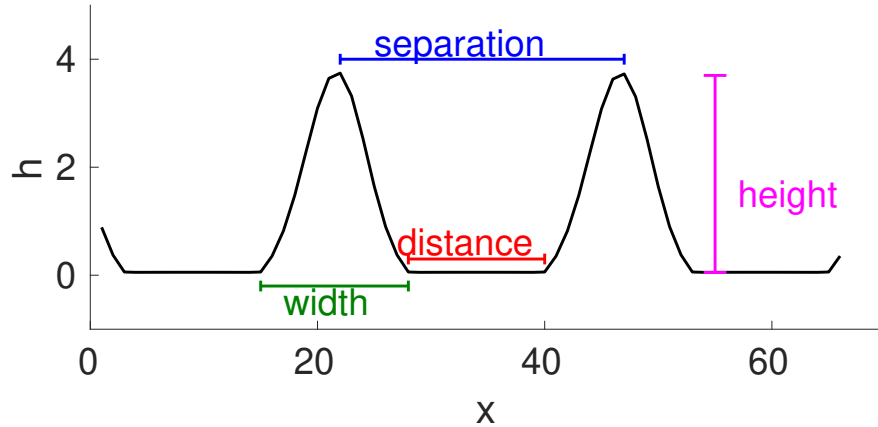

Figure 8.4: Visual guide for the definitions of drop height, width, distance, and separation. Drops correspond to a steady state profile $h(x)$ for the same simulation as depicted in Fig. 8.5, namely, no disjoining pressure ($A = 0$) and parameter values $B = 0.615$ and $C = 1$.

In Fig. 8.8 histograms are shown for these four observables. As expected from the linear behavior, the metastable surface (the only one for which the dispersion relation of Eq. (8.33) presents a narrow band of unstable modes) is the case in which all the histograms are substantially more concentrated than for the other scenarios, in which the distribution of drop heights, widths, distances, and separations appear to be much broader.
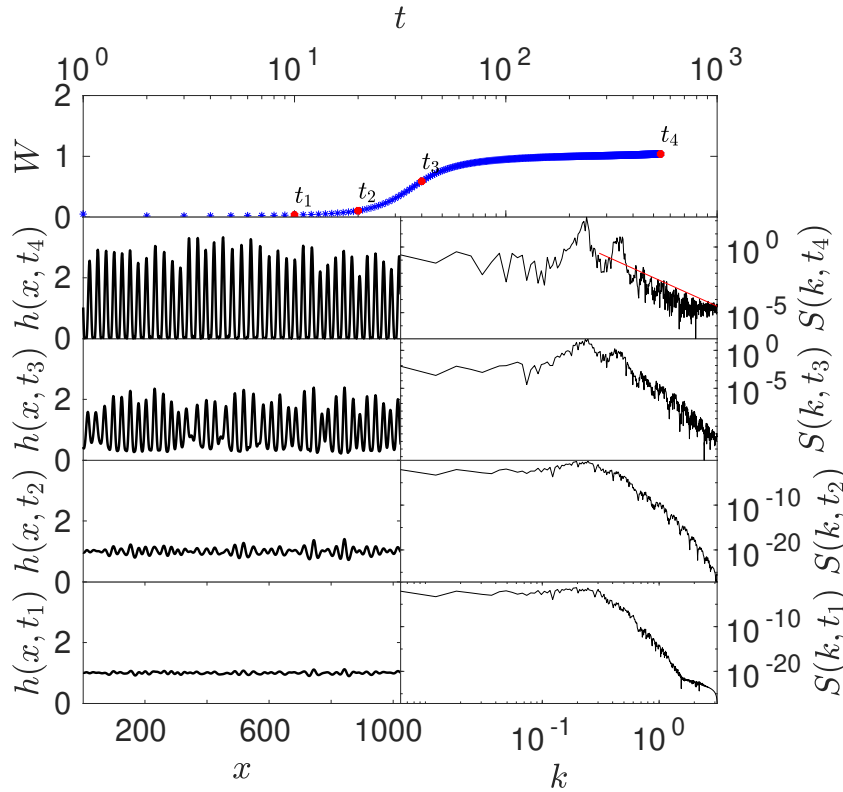
Figure 8.5: *Surface morphology and structure factor in numerical simulations of Eq. (8.33) without disjoining pressure. Here, $A = 0$, $B = 0.615$, and $C = 1$. The red solid line is a guide to the eye with -4 slope.*

Figure 8.6: Surface morphology and structure factor in numerical simulations of Eq. (8.33) using the unstable effective interface potential as in Eq. (8.38). Here, $A = 0.02$, $B = 0.45$, and $C = 1$. The red solid line is a guide to the eye with -4 slope.
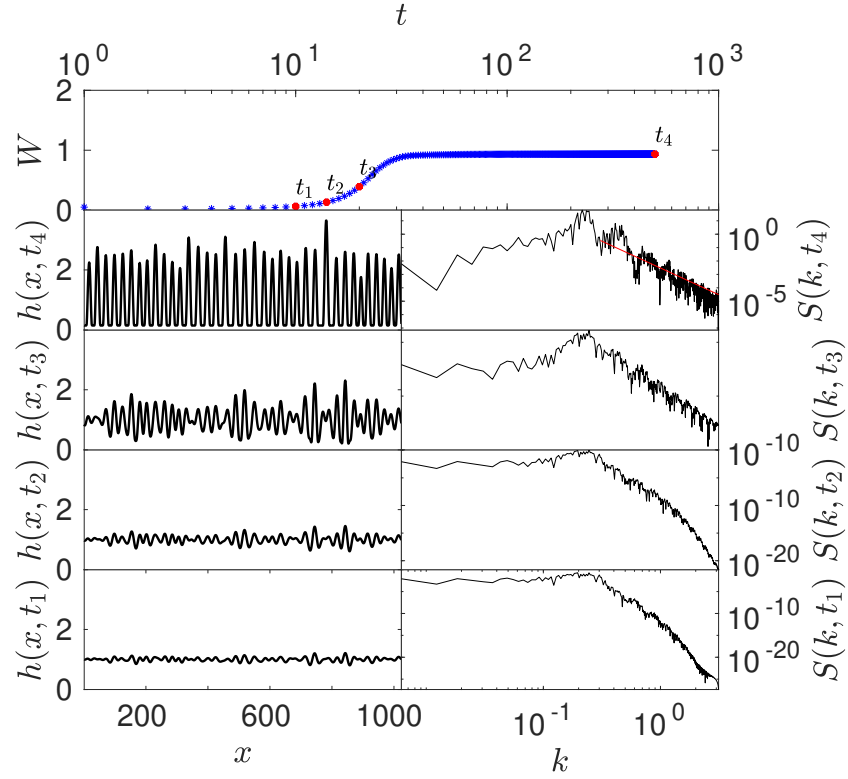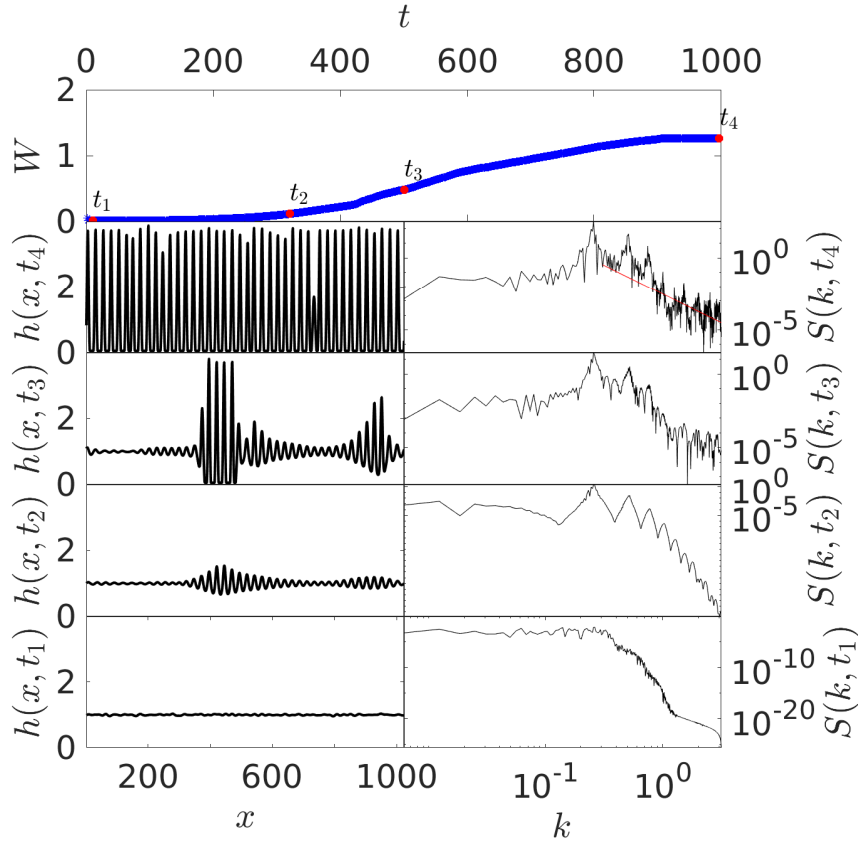
Figure 8.7: *Surface morphology and structure factor in numerical simulations of Eq. (8.33) using the metastable effective interface potential as in Eq. (8.39). Here, $A = 0.008$, $B = 0.92$, and $C = 1$. The red solid line is a guide to the eye with -4 slope.*
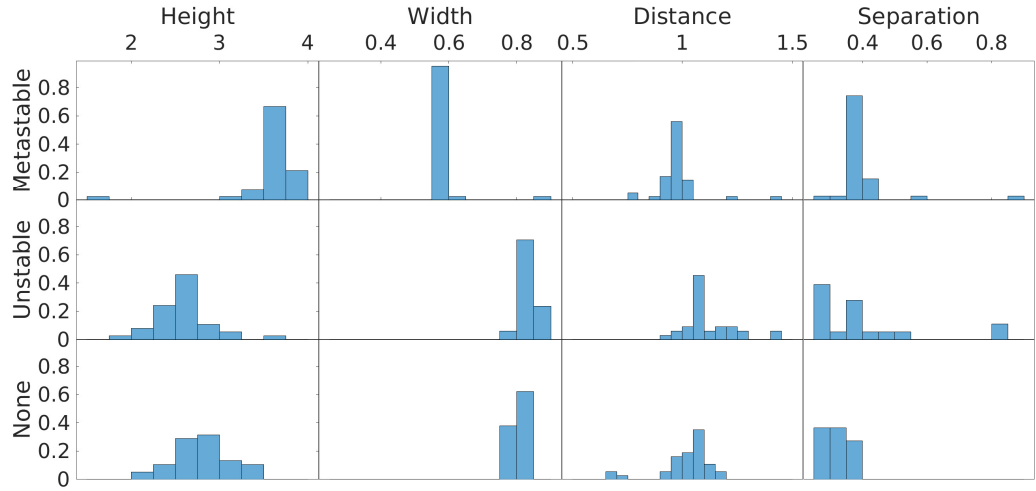
Figure 8.8: *Histogram for the drops at steady state from simulations of Eq. (8.33) (see Figs. 8.5-8.7). For each type of interface potential, the distribution of drop height (maximum value), width, distance, and separation (as defined in Fig. 8.4) is depicted. Values of width, distance, and separation have been normalized such that 1 corresponds to the distance between drops predicted by the most unstable mode in the corresponding linear dispersion relation.*

8.5   Conclusions

Although ferrofluid films are well known to form ordered patterns of drops at macro and microscopic scales [47] and this pattern formation has successfully been mathematically modelled [48, 64], there are no evidences of *nano*scopic well-ordered patterns for ferrofluids, either experimental or theoretical, as the available models in the literature for thin ferrofluid films either do not consider physical effects suitable for those ultrasmall scales (disjoining pressure potential) [147], or are based on assumptions that lead to expect disordered patterns [146]. In this Chapter we derive an interfacial equation for an ultrathin ferrofluid film that considers the disjoining pressure potential and the magnetic field interaction with the fluid under assumptions that lead to a nonlinear behavior predicting a highly-ordered pattern under some specific conditions (specifically, metastable disjoining pressure potential [61]).

Further investigation of this phenomenon based on Eq. (8.33) could elucidate the formation (or not) of these patterns under further different types of disjoining pressure potentials, the behavior of these patterns on two dimensional substrates, and the sensitivity of the order achieved at steady state to different levels of thermal fluctuations, which could be relevant at these small scales [59]. Moreover, the information extracted from the conditions and physical parameter values that lead to the ordered pattern formation could guide the selection of materials and conditions under which experiments should be carried out, in order to replicate the high degree of order that has been already observed experimentally at macro and microscales. At the nanoscale, ferrofluids could have novel practical applications in fields like electronics and optoelectronics, in which the fabrication of well-ordered micro to nanometer patterns is one of the current challenges [152].

Conclusions and outlook

Throughout this thesis we have studied different self-organization processes in the specific context of fluid films when the film thickness is *ultra*small. In this context, inertial effects can be neglected, as the Reynolds number becomes extremely low, *but* two important physical effects become relevant at these small scales: thermal fluctuations and the interaction between the fluid surface and the substrate, the so-called *disjoining pressure*.

Two main physical systems in the context of fluid films have been considered. The first system we deal with is an ultrathin fluid film falling down an inclined slope. The surface evolution of this film can be modelled using the classic Kuramoto-Sivashinsky equation. Although the linearly unstable term of the KS equation induced by the gravitational effects is negligible here due to the ultra small scale, when the fluid-substrate interaction is governed by a spinodal (unstable) potential, it induces an equivalent unstable term. Moreover, thermal fluctuations, expected to be relevant at ultra small scales, induce a novel conserved noise term in the evolution equation.

The kinetic roughening behavior of the KS equation in the hydrodynamic limit is expected to be described by Burgers equation. The universality classes of the stochastic Burgers equation, both with *non-conserved* and *conserved* noise, have been studied, focusing on the role of the fluctuation statistics. In both cases, there is an emergent up-down symmetry that is not predicted by the bare interactions of the nonlinear terms. This result allows us to deepen the understanding of the relation between fluctuation statistics and the symmetries of the corresponding equations. Further research in this context could involve the assessment of the fluctuation statistics in additional equations in which the $(x, h) \leftrightarrow (-x, -h)$ is present in spite of not being up-down symmetric. Moreover, we have proved that the fluctuation statistics of the Burgers equation with conserved noise, which had been considered almost equivalent to the KPZ equation —as the former can be obtained as the slopes evolution equation for the latter—, can not be trivially deduced from that of the KPZ equation. Indeed, the Gaussian fluctuations in the Burgers equation with conserved

noise constitute a nontrivial example of Gaussian random variables obtained as the sum of non-Gaussian (in this case, Tracy-Widom distributed) random variables. This result suggests that there could be a nontrivial relation between the universality class of other pairs of equations in which one of them is obtained as the slope evolution equation of the other one, as e.g. for the case of the nonlinear MBE equation. The Gaussian nature of fluctuations in both versions of the noisy Burgers equation does also allow for the derivation of simple linear models that are exact approximations in terms of the universality class.

In the novel context of the KS equation with conserved noise, we have assessed a transition between universality subclasses controlled by e.g. the system temperature, the transition occurring at a non-zero value of the critical temperature T_c. This type of transition is unprecedented and is accompanied by a transition in the dominant nature of the surface fluctuations (chaotic for $T < T_c$ vs stochastic for $T > T_c$). Finding other physical systems in which this kind of universality (sub)class transition occur due to a change in the dominant type of fluctuations would improve the understanding of this novel mechanism.

We also assess the ultra-low viscosity and surface tension limits in the KS equation, leading to the study of the stochastic KdV equation with either Burgers or KPZ nonlinearities, both of which exhibit anomalous scaling behaviors. In the case of the Burgers nonlinearity, an unprecedented random-deposition like process with saturation is observed. In the case of a KPZ nonlinearity, an intrinsic anomalous scaling is observed, which is also unprecedented in local stochastic equations with time-dependent noise. The inviscid KPZ equation seems not to be numerically integrable in two-dimensional substrates. We have also demonstrated that there is a growth model based on an Ising system in which the same scaling exponents are achieved, hence it provides an alternative approach to the study of this universality class. However, interaction between the growing surface with the system boundaries hinders the study of that model in higher dimensions. Further research involving much larger systems could be interesting in this context, as well as deepening the study of the potential relationship between Ising and the inviscid limit of the KPZ equation beyond the kinetic roughening universality class.

Finally, as an example of an ordered ultrathin film, we have studied the dynamics of an ultrathin ferrofluid film under an applied magnetic field. We have demonstrated that, for suitable parameter conditions and a metastable interaction between the fluid and the substrate, a substantially higher level of order can be achieved for the stationary drops that form, than under other conditions. The study of the influence of thermal fluctuations, which can be relevant in the context of ultrathin fluid flows, in

the level of order achieved, is an interesting possibility for future research. Moreover, analogous studies for two-dimensional substrates should be performed as a previous step to the experimental study of these systems.

Appendix

A. DRG analysis of field statistics for the 1D noisy Burgers equation

This section provides additional details on the evaluation of field cumulants for the noisy Burgers equation with conserved noise, Eq. 5.1 (see Chapter 5), following the Dynamical Renormalization Group (DRG) approach of [78], previously applied to the evaluation of field statistics in the cases of the KPZ [80, 81, 83], the non-linear Molecular Beam Epitaxy [82] equations, and of the Burgers equation with non-conserved noise (see Chapter 3).

As derived in Chapter 3, the n-th cumulant of u reads

$$\langle u^n \rangle_c = \int_{\mathbb{R}^{2(n-1)}} G(k_n, \omega_n) L_n \prod_{j=1}^{n-1} \frac{dk_j d\omega_j}{(2\pi)^2} G(k_j, \omega_j), \qquad (8.40)$$

with $G(k, \omega) = (-\mathrm{i}\omega + \nu_<(k)k^2)^{-1}$, $\nu_<(k) = \sqrt{\frac{\lambda^2 D}{2\pi\nu}} |k|^{-1/2}$ (see [80] for details), $G(k, \omega)\hat{\eta} = \hat{u}(k, \omega)$, hat is space-time Fourier transform, k is wave-number, ω is time frequency, $k_n = -\sum_{j=1}^{n-1} k_j$, and $\omega_n = -\sum_{j=1}^{n-1} \omega_j$. The correction L_n is perturbatively computed to one loop order as

$$L_n = (2D)\delta_{n,2} + L_{n,1}, \qquad (8.41)$$

where $L_{n,1} = K\lambda^n \mathrm{i}^n k_n l_{n,1} \prod_{j=1}^{n-1} k_j$ is the lowest-order correction in the Feynman expansion of the cumulants, with $K = (2n-2)!!$ being a combinatorial factor (number of different fully-connected diagrams). As we are interested in the $(k_i, \omega_i) \to (0, 0)$ limit,

$$l_{n,1} = \int_{-\infty}^{\infty} \frac{d\Omega}{2\pi} \int^> \frac{dq}{2\pi} |G_0(q, \Omega)|^{2n} (2Dq^2)^n, \qquad (8.42)$$

151

where $G_0(k, \omega) = (-i\omega + \nu k^2)^{-1}$ and the integration domain in $\int^>$ is the region $\{q \in \mathbb{R} | \Lambda(\ell) = \Lambda_0 e^{-\ell} < |q| < \Lambda_0\}$. After integration,

$$l_{n,1} = \frac{2^{n+1}\Gamma(n - \frac{1}{2})}{4\pi^{3/2}(n-1)!} \frac{D^n \nu^{1-2n}}{\Lambda^{2n-3}(\ell)} \frac{e^{(3-2n)\ell} - 1}{3 - 2n}. \tag{8.43}$$

Taking $\ell \to 0$, and considering the dependence of ν and D with Λ, [80], the following differential equation is obtained,

$$\frac{dl_{n,1}}{d\ell} = \frac{2^{n+1}\Gamma(n - \frac{1}{2})}{4\pi^{3/2}(n-1)!} \frac{(D\nu\frac{D\lambda^2}{2\pi\nu^3})^{(1-n)/4}}{\Lambda^{\frac{5}{2}(n-1)}(\ell)}, \tag{8.44}$$

whose solutions for large ℓ become

$$l_{n,1}(\ell) \simeq \frac{2^{n+1}\Gamma(n - \frac{1}{2})}{4\pi^{3/2}(n-1)!} \frac{(D\nu\frac{D\lambda^2}{2\pi\nu^3})^{(1-n)/4}}{\frac{5}{2}(n-1)\Lambda^{\frac{5}{2}(n-1)}(\ell)}. \tag{8.45}$$

Due to symmetry among $k_1, \ldots, k_{n-1}$, we take [78, 80, 81, 83]

$$l_{n,1}(k) = \frac{2^{n+1}\Gamma(n - \frac{1}{2})}{4\pi^{3/2}(n-1)!} \frac{(D\nu\frac{D\lambda^2}{2\pi\nu^3})^{(1-n)/4}}{\frac{5}{2}(n-1)} \prod_{j=1}^{n-1} \frac{1}{k_j^{5/2}}. \tag{8.46}$$

For $n > 1$, as $k^{5/2}f(\omega/k^z) = k^{-3/2}\nu(k)^{-2}|G(k, \omega)|^{-2}$, where f is a scaling function $[f(u) \to 1$ as $u \to 0]$, we substitute $k_i^{-5/2} \simeq k_i^{3/2}\nu^2(k_i)|G(k_i, \omega_i)|^2$. Finally,

$$\langle u^n \rangle_c = A \int_{\mathbb{R}^{2(n-1)}} G(k_n, \omega_n)k_n \times$$
$$\prod_{i=1}^{n-1} \frac{dk_i d\omega_i}{(2\pi)^2} k_i G(k_i, \omega_i)k_i^{3/2}\nu^2(k_i)|G(k_i, \omega_i)|^2, \tag{8.47}$$

where $A = \pi^{n-1/2}i^n\Gamma(n - 1/2)K2D/[n!(n-1)\lambda^{n-2}]$.

Bibliography

[1] E. Rodriguez-Fernandez and R. Cuerno, *Gaussian statistics as an emergent symmetry of the stochastic scalar Burgers equation*, Phys. Rev. E **99**, 042108 (2019).

[2] E. Rodriguez-Fernandez and R. Cuerno, *Non-KPZ fluctuations in the derivative of the Kardar-Parisi-Zhang equation or noisy Burgers equation*, Phys. Rev. E **101**, 052126 (2020).

[3] E. Rodriguez-Fernandez and R. Cuerno, *Transition between chaotic and stochastic universality classes of kinetic roughening*, Phys. Rev. Research **3**, L012020 (2021).

[4] H. Bruus, *Theoretical Microfluidics*, Oxford University Press (2008).

[5] R. E. Rosensweig, *Ferrohydrodynamics*, Dover Publications Inc (2014).

[6] S. Prakash and J. Yeom, *Nanofluidics and Microfluidics*, Elsevier (2014).

[7] N. Ghoniem and D. Walgraef, *Instabilities and Self-Organization in Materials*, Oxford University Press (2008).

[8] A.-L. Barabási and H. E. Stanley, *Fractal concepts in surface growth*, Cambridge University Press (1995).

[9] E. Vivo, *Generic Scale Invariance in Continuum Models of Two-Dimensional Surfaces*, PhD thesis, Universidad Carlos III de Madrid (2014).

[10] K. Christensen and N. R. Moloney, *Complexity and Criticality*, Imperial College Press (2005).

[11] J. Krug, *Origins of scale invariance in growth processes*, Adv. Phys. **46**, 139 (1997).

[12] J. G. Moreira, J. K. L. d. Silva, and S. O. Kamphorst, *On the fractal dimension of self-affine profiles*, J. Phys. Math. Gen. **27**, 8079 (1994).

[13] T. Sarlat, A. Lelarge, E. Søndergard, and D. Vandembroucq, *Frozen capillary waves on glass surfaces: an AFM study*, Eur. Phys. J. B **54**, 121–126 (2006).

[14] J. J. Ramasco, J. M. López, and M. A. Rodríguez, *Generic Dynamic Scaling in Kinetic Roughening* Phys. Rev. Letters **84**, 10 (2000).

[15] E. Vivo, M. Nicoli, and R. Cuerno, *Strong anisotropy in two-dimensional surfaces with generic scale invariance: Gaussian and related models.* Phys. Rev. E **86**, 051611 (2012).

[16] J. Krug and P. Meakin, *Kinetic Roughening of Laplacian Fronts*, Phys. Rev. Lett. **66**, 703 (1991).

[17] M. Kardar, G. Parisi, and Y.-C. Zhang, *Dynamic Scaling of Growing Interfaces*, Phys. Rev. Lett. **56**, 889 (1986).

[18] T. Halpin-Healy and K. A. Takeuchi, *A KPZ Cocktail-Shaken, not Stirred...*, J. Stat. Phys. **160**, 794 (2015).

[19] O. Hallatschek, P. Hersen, S. Ramanathan, and D. R. Nelson, *Genetic drift at expanding frontiers promotes gene segregation*, Proc. Natl. Acad. Sci. U.S.A. **104**, 19926 (2007).

[20] M. Nicoli, R. Cuerno, and M. Castro, *Unstable nonlocal interface dynamics*, Phys. Rev. Lett. **102**, 256102 (2009).

[21] K. A. Takeuchi and M. Sano, *Evidence for Geometry-Dependent Universal Fluctuations of the Kardar-Parisi-Zhang Interfaces in Liquid-Crystal Turbulence*, J. Stat. Phys. **147**, 853 (2012).

[22] H. Van Beijeren, *Exact results for anomalous transport in one-dimensional hamiltonian systems*, Phys. Rev. Lett. **108**, 180601 (2012).

[23] C. B. Mendl and H. Spohn, *Dynamic correlators of Fermi-Pasta-Ulam chains and nonlinear fluctuating hydrodynamics*, Phys. Rev. Lett. **111**, 230601 (2013).

[24] S. G. Alves, T. J. Oliveira, and S. C. Ferreira, *Non-universal parameters, corrections and universality in Kardar-Parisi-Zhang growth*, J. Stat. Mech.: Theor. Exp. P05007 (2013).

[25] S. N. Santalla, J. Rodríguez-Laguna, T. Lagatta, and R. Cuerno, *Random geometry and the Kardar-Parisi-Zhang universality class*, New J. Phys. **17**, 33018 (2015).

[26] E. Altman, L. M. Sieberer, L. Chen, S. Diehl, and J. Toner, *Two-dimensional superfluidity of exciton polaritons requires strong anisotropy*, Phys. Rev. X **5**, 011017 (2015).

[27] L. Chen, C. F. Lee, and J. Toner, *Mapping two-dimensional polar active fluids to two-dimensional soap and one-dimensional sandblasting*, Nature Comm. **7**, 12215 (2016).

[28] A. Ballestad, B. J. Ruck, J. H. Schmid, M. Adamcyk, E. Nodwell, C. Nicoll and T. Tiedje, *Surface morphology of GaAs during molecular beam epitaxy growth: Comparison of experimental data with simulations based on continuum growth equations*, Phys. Rev. B **65**, 205302 (2002).

[29] M. Kardar, *Statistical Physics of Fields*, Cambridge University Press (2012).

[30] I. S. S. Carrasco and T. J. Oliveira, *Universality and geometry dependence in the class of the nonlinear molecular beam epitaxy equation*, Phys. Rev. E **94**, 050801(R) (2016).

[31] T. Kriecherbauer and J. Krug, *A pedestrian's view on interacting particle systems, KPZ universality and random matrices*, J. Phys. A: Math. Theor. **43**, 403001 (2010).

[32] K. A. Takeuchi, *Crossover from Growing to Stationary Interfaces in the Kardar-Parisi-Zhang Class*, Phys. Rev. Lett. **110**, 210604 (2013).

[33] K. A. Takeuchi, *An appetizer to modern developments on the Kardar-Parisi-Zhang universality class*, Physica A **504**, 77 (2018).

[34] I. Corwin, *The Kardar-Parisi-Zhang Equation and Universality Class*, Random Matrices: Theo. Appl. **1**, 1130001 (2012).

[35] F. Bornemann, *On the numerical evaluation of Fredholm determinants*, Math. Comput. **79** 871 (2010).

[36] N. Wolchover, *At the Far Ends of a New Universal Law*, book chapter in *The Best Writing on Mathematics*, Princeton University Press (2016).

[37] M. Nicoli, R. Cuerno and M. Castro, *Dimensional fragility of the Kardar–Parisi–Zhang universality class*, J. Stat. Mech. P11001 (2013).

[38] Y. Saito, M. Dufay, and O. Pierre-Louis, *Nonequilibrium Cluster Diffusion During Growth and Evaporation in Two Dimensions*, Phys. Rev. Lett. **108**, 245504 (2012).

[39] K. A. Takeuchi, M. Sano, T. Sasamoto, and H. Spohn, *Growing interfaces uncover universal fluctuations behind scale invariance*, Sci. Rep. **1**, 34 (2011).

[40] R. Livi and P. Politi, *Nonequilibrium Statistical Physics: A Modern Perspective* (Cambridge University Press, Cambridge, England, 2017).

[41] M. Prähofer and H. Spohn, *Exact Scaling Functions for One-Dimensional Stationary KPZ Growth*, J. Stat. Phys. **115**, 255 (2004).

[42] T. Imamura and T. Sasamoto, *Exact Solution for the Stationary Kardar-Parisi-Zhang Equation*, Phys. Rev. Lett. **108**, 190603 (2012).

[43] R. Hoyle, *Pattern formation. An introduction and methods* (Cambridge University Press, 2006).

[44] M. Cross and H. Greenside, *Pattern Formation and Dynamics in Nonequilibrium Systems*, Cambridge University Press (2009).

[45] J. M. Yeomans, *Statistical Mechanics of Phase Transitions*, Oxford University Press (1992).

[46] R. Seemann, S. Herminghaus, and K. Jacobs, *Gaining control of pattern formation of dewetting liquid films*, J. Phys.: Condens. Matter **13** 4925 (2001).

[47] C.Y. Chen and C.S. Li, *Ordered microdroplet formations of thin ferrofluid layer breakups*, Phys. Fluids **22**, 014105 (2010).

[48] M. D. Cowley and R. E. Rosensweig, *The interfacial stability of a ferromagnetic fluid*, J. Fluid. Mech. **30**, 671-688 (1967).

[49] M. Pradas, G. A. A. Pavliotis, S. Kalliadasis, D. T. T. Papageorgiou, and D. Tseluiko, *Additive noise effects in active nonlinear spatially extended systems*, Eur. J. Appl. Math. **23**, 563 (2012).

[50] D. Benney, *Long waves on liquid films*, J. Math. Phys. (NY) **45**, 150 (1966).

[51] V. Yakhot, *Large-scale properties of unstable systems governed by the Kuramoto-Sivashinksi equation*, Phys. Rev. A **24**, 642 (1981).

[52] D. Forster, D. R. Nelson, and M. J. Stephen, *Large-distance and long-time properties of a randomly stirred fluid*, Phys. Rev. A **16**, 732 (1977).

[53] L. Bertini, N. Cancrini, and G. Jona-Lasinio, *The Stochastic Burgers Equation*, Commun. Math. Phys. **165**, 211 (1994).

[54] J. Bec and K. Khanin, *Burgers turbulence*, Phys. Rep. **447**, 1 (2007).

[55] E. Vivo, M. Nicoli, and R. Cuerno, *Strong anisotropy in two-dimensional surfaces with generic scale invariance: Nonlinear effects*, Phys. Rev. E **89**, 042407 (2014).

[56] T. Hwa and M. Kardar, *Avalanches, hydrodynamics, and discharge events in models of sandpiles*, Phys. Rev. A **45**, 7002 (1992).

[57] D. Tseluiko and D. T. Papageorgiou, *Dynamics of an electrostatically modified Kuramoto–Sivashinsky–Korteweg–de Vries equation arising in falling film flows*, Phys. Rev. E **82**, 016322 (2010).

[58] M. Rauscher and S. Dietrich, *Wetting phenomena in nanofluidics*, Annu. Rev. Mater. Res. **38**, 143-172 (2008).

[59] K. Mecke and M. Rauscher, *On thermal fluctuations in thin film flow*, J. Phys. Condens. Matter **17**, S3515 (2005).

[60] R. V. Craster and O. K. Matar, *Dynamics and stability of thin liquid films*, Rev. Mod. Phys. **81**, 1131 (2009).

[61] R. Seeman and S. Herminghaus and K. Jacobs, *Dewetting patterns and molecular forces: a reconciliation*, Phys. Rev. Lett. **86**, 5534-5537 (2001).

[62] J. Becker, G. Grun, R. Seemann, H. Mantz, K. Jacobs, K. R. Mecke, and R. Blossey, *Complex dewetting scenarios captured by thin-film models*, Nat. Mater. **2**, 59-63 (2002).

[63] R. Richter and I. V. Barashenkov, *Two-Dimensional Solitons on the Surface of Magnetic Fluids*, Phys. Rev. Lett. **94**, 184503 (2005).

[64] B. Abou, G. Naron de Surgy and J. E. Wesfreid, *Dispersion Relation in a Ferrofluid Layer of Any Thickness and Viscosity in a Normal Magnetic Field; Asymptotic Regimes*, J. Phys. II Fance **7**, 1159-1171 (1997).

[65] H. W. Xi, R. Toral, J. D. Gunton, and M. I. Tribelsky, *Extensive chaos in the Nikolaevskii model*, Phys. Rev. E **62**, R17 (2000).

[66] L. Giada, A. Giacometti, and M. Rossi, Pseudospectral method for the Kardar-Parisi-Zhang equation, Phys. Rev. E **65**, 036134 (2002).

[67] R. Gallego, M. Castro, and J. M. López, *Pseudospectral versus finite-difference schemes in the numerical integration of stochastic models of surface growth*, Phys. Rev. E **76**, 051121 (2007).

[68] M. Nicoli, M. Castro, and R. Cuerno, *Unified moving-boundary model with fluctuations for unstable diffusive growth*, Phys. Rev. E **78**, 021601 (2008).

[69] R. Gallego, *Predictor-corrector pseudospectral methods for stochastic partial differential equations with additive white noise*, Appl. Math. Comput. **208**, 3905 (2011).

[70] R. Toral and P. Colet, *Stochastic Numerical Methods: An Introduction for Students and Scientists* (Wiley-VCH, Weinheim, 2014).

[71] M. Hairer and J. Voss, *Approximations to the Stochastic Burgers Equation*, J. Nonlinear. Sci. **21**, 897 (2011).

[72] T. Sasamoto and H. Spohn, *Superdiffusivity of the 1D lattice Kardar-Parisi-Zhang equation*, J. Stat. Phys. **137**, 917 (2009).

[73] S. Nesic, *Stochastic Dynamics of Substrate-confined Systems: Fisher Fronts and Thin Liquid Films*, PhD thesis, Universidad Carlos III de Madrid, (2015).

[74] M. H. Kalos, P. A. Witlock, *Monte Carlo Methods*, Wiley VCH (2004).

[75] J. B. Gao, J. Hu, W. W. Tung, and Y. H. Cao, *Distinguishing chaos from noise by scale-dependent Lyapunov exponent*, Phys. Rev. E **74**, 066204 (2006).

[76] M. Cencini and A. Vulpiani, *Finite size Lyapunov exponent: Review on applications*, J. Phys. A: Math. Theor. **46**, 254019 (2013).

[77] A. Pikovsky and A. Politi, *Lyapunov Exponents: A Tool to Explore Complex Dynamics* (Cambridge University Press, Cambridge, England, 2016).

[78] V. Yakhot and S. A. Orszag, *Renormalization-Group Analysis of Turbulence*, Phys. Rev. Lett. **57**, 1722 (1986).

[79] G. Grinstein, Generic scale invariance and self-organized criticality, in *Scale Invariance, Interfaces, and Non-Equilibrium Dynamics*, edited by A. McKane, M. Droz, J. Vannimenus, and D. Wolf (Springer, Cambridge, England, 1995).

[80] T. Singha and M. K. Nandy, *Skewness in (1 + 1)-dimensional Kardar-Parisi-Zhang-type growth*, Phys. Rev. E **90**, 062402 (2014).

[81] T. Singha and M. K. Nandy, *Kurtosis of height fluctuations in (1 + 1) dimensional KPZ Dynamics*, J. Stat. Mech.: Theor. Exp. 05020 (2015).

[82] T. Singha and M. K. Nandy, *A renormalization scheme and skewness of height fluctuations in (1 + 1)-dimensional VLDS dynamics*, J. Stat. Mech.: Theor. Exp. 023205 (2016).

[83] T. Singha and M. K. Nandy, *Hyperskewness of (1+1)-dimensional KPZ height fluctuations*, J. Stat. Mech.: Theor. Exp. 013203 (2016).

[84] P. M. Chaikin and T. C. Lubensky, *Principles of Condensed Matter Physics*, Cambridge University Press (1995).

[85] J. P. Sethna, *Statistical Mechanics: Entropy, Order Parameters, and Complexity*, Oxford University Press (2006).

[86] C. D. Batista and G. Ortiz, *Algebraic approach to interacting quantum systems*, Adv. Phys. **53**, 1 (2004).

[87] L. M. Sieberer, S. D. Huber, E. Altman, and S. Diehl, *Dynamical Critical Phenomena in Driven-Dissipative Systems*, Phys. Rev. Lett. **110**, 195301 (2013).

[88] U. C. Täuber, *Critical Dynamics*, Cambridge University Press (2014).

[89] C. Castellano, S. Fortunato, and V. Loreto, *Statistical physics of social dynamics*, Rev. Mod. Phys. **81**, 591 (2009).

[90] M. A. Munoz, Colloquium: *Criticality and dynamical scaling in living systems*, Rev. Mod. Phys. **90**, 31001 (2018).

[91] G. Pruessner, *Self-Organised Criticality: Theory, Models and Characterisation*, Cambridge University Press (2012).

[92] E. Frey, U. C. Täuber, and H. K. Janssen, *Scaling regimes and critical dimensions in the Kardar-Parisi-Zhang problem*, Europhys. Lett. **47**, 14 (1999).

[93] F. Hayot and C. Jayaprakash, *Multifractality in the stochastic Burgers equation*, Phys. Rev. E **56**, 4259 (1997).

[94] C. Gardiner, *Stochastic Methods, a Handbook for the Natural and Social Sciences* (Springer, New York, 2009).

[95] J. M. Burgers, *The Nonlinear Diffusion Equation* (D. Reidel, Dordrecht, Holland, 1974).

[96] S. Bendaas, *Periodic wave shock solutions of Burgers equations*, Cogent Math. Stat. **5**, 1463597 (2018).

[97] G. Da Prato, A. Debussche, and R. Temam, *Stochastic Burgers' equation*, Nonlin. Diff. Eq. Appl. **1**, 389 (1994).

[98] L. Bertini and G. Giacomin, *Stochastic Burgers and KPZ Equations from Particle Systems*, Comm. Math. Phys. **183**, 571 (1997).

[99] M. Gubinelli and M. Jara, *Regularization by noise and stochastic Burgers equations*, Stoch. PDE Anal. Comp. **1**, 325 (2013).

[100] U. Frisch, *Turbulence: the legacy of A. N. Kolmogorov* (Cambridge University Press, Cambridge, England, 1995).

[101] J. A. Krommes, *Fundamental statistical descriptions of plasma turbulence in magnetic fields*, Phys. Rep. **360**, 1 (2002).

[102] H. Spohn, *Large Scale Dynamics of Interacting Particles* (Springer-Verlag, Berlin, 1991).

[103] J.-Y. Fortin, and M. Clusel, *Applications of Extreme Value Statistics*, J. Phys. A: Math. Theor. **48**, 183001 (2015).

[104] M. Clusel and E. Bertin, *Global fluctuations in physical systems a subtle interplay between sum and extreme value statistics*, Int. J. Mod. Phys. B **22**, 3311 (2008).

[105] K. Ueno, H. Sakaguchi, and M. Okamura, *Renormalization-group and numerical analysis of a noisy Kuramoto-Sivashinsky equation in 1+1 dimensions*, Phys. Rev. E **71**, 046138 (2005).

[106] D. Squizzato, L. Canet, and A. Minguzzi, *Kardar-Parisi-Zhang universality in the phase distributions of one-dimensional exciton-polaritons*, Phys. Rev. B **97**, 195453 (2018).

[107] N. R. Smith, B. Meerson, and P. V. Sasorov, *Local average height distribution of fluctuating interfaces*, Phys. Rev. E **95**, 012134. (2017).

[108] H. Sakaguchi, *Shock Structures and Velocity Fluctuations in the Noisy Burgers and KdV-Burgers Equations*, Prog. Theor. Phys. **110**, 187 (2003).

[109] J. Stoyanov, *Counterexamples in Probability* (John Wiley and Sons, Chichester, 1997).

[110] I. S. S. Carrasco, K. A. Takeuchi, S. C. Ferreira, and T. J. Oliveira, *Interface fluctuations for deposition on enlarging flat substrates*, New J. Phys. **16**, 123057 (2014).

[111] Y. T. Fukai and K. A. Takeuchi, *Kardar-Parisi-Zhang Interfaces with Inward Growth*, Phys. Rev. Lett. **119**, 030602 (2017).

[112] I. S. S. Carrasco and T. J. Oliveira, *Kardar-Parisi-Zhang growth on one-dimensional decreasing substrates*, Phys. Rev. E **98**, 010102(R). (2018).

[113] S. N. Santalla, J. Rodríguez-Laguna, A. Celi, and R. Cuerno, *Topology and the Kardar-Parisi-Zhang universality class*, J. Stat. Mech.: Theory Exp. (2017), 023201.

[114] I. S. S. Carrasco and T. J. Oliveira, *Circular Kardar-Parisi-Zhang interfaces evolving out of the plane*, Phys. Rev. E **99**, 032140 (2019).

[115] I. S. S. Carrasco and T. J. Oliveira, *Geometry dependence in linear interface growth*, Phys. Rev. E **100**, 042107 (2019).

[116] F. Hayot, C. Jayaprakash, and C. Josserand, *Long-wavelength properties of the Kuramoto-Sivashinsky equation*, Phys. Rev. E **47**, 911 (1993).

[117] K. Sneppen, J. Krug, M. H. Jensen, C. Jayaprakash, and T. Bohr, *Dynamic scaling and crossover analysis for the Kuramoto-Sivashinsky equation*, Phys. Rev. A **46**, R7351 (1992).

[118] D. Roy and R. Pandit, *One-dimensional Kardar-Parisi-Zhang and Kuramoto-Sivashinsky universality class: Limit distributions*, Phys. Rev. E **101**, 030103(R) (2020).

[119] R. Cuerno, H. A. Makse, S. Tomassone, S. T. Harrington, and H. E. Stanley, *Stochastic model for surface erosion via ion sputtering: Dynamical evolution from ripple morphology to rough morphology*, Phys. Rev. Lett. **75**, 4464 (1995).

[120] R. Cuerno and A.-L. Barabási, *Dynamic scaling of ion-sputtered surfaces*, Phys. Rev. Lett. **74**, 4746 (1995).

[121] S. Mathey, E. Agoritsas, T. Kloss, V. Lecomte, and L. Canet, Kardar-Parisi-Zhang equation with short-range correlated noise: Emergent symmetries and nonuniversal observables, Phys. Rev. E **95**, 032117. (2017).

[122] C. Misbah, O. Pierre-Louis, and Y. Saito, *Crystal surfaces in and out of equilibrium: A modern view*, Rev. Mod. Phys. **82**, 981 (2010).

[123] A. Karma, and C. Misbah, *Competition between noise and determinism in step flow growth*, Phys. Rev. Lett. **71**, 3810 (1993).

[124] H. Spohn, in *Thermal Transport in Low Dimensions*, Lecture Notes in Physics Vol. 921, edited by S. Lepri (Springer International Publishing, Cham, 2016), Chap. 3, pp. 107-158.

[125] P. Manneville and H. Chaté, *Phase turbulence in the two-dimensional complex Ginzburg-Landau equation*, Physica D **96**, 30 (1996).

[126] B. M. Boghosian, C. C. Chow, and T. Hwa, *Hydrodynamics of the Kuramoto-Sivashinsky equation in two dimensions*, Phys. Rev. Lett. **83**, 5262 (1999).

[127] S. Kalliadasis, E. A. Demekhin, C. Ruyer-Quil, and M. G. Velarde, *Thermocapillary instability andwave formation on a film falling down a uniformly heated plane*, J. Fluid Mech **492**, 303 (2003).

[128] C. Ruyer-Quil and S. Kalliadasis, *Wavy regimes of film flow down a fiber*, Phys. Rev. E **85**, 046302 (2012).

[129] S. Kalliadasis and U. Thiele, *Thin Films of Soft Matter*, Springer (2007).

[130] T. Kawahara, *Formation of saturated solitons in a nonlinear dispersive system with instability and dissipation*, Phys. Rev. Lett. **51**, 381 (1983).

[131] C. A. Condat and R. A. Guyer, *Korteweg-de Vries solitons and helium films*, Phys. Rev. B **25**, 3117 (1982).

[132] A. E. Derbyshev and A. M. Povolotsky, *Nonstationary Generalized TASEP in KPZ and Jamming Regimes*, J. Stat. Phys. **185**, 16 (2021).

[133] B. G. Barreales, J. J. Meléndez, R. Cuerno, and J. J. Ruiz-Lorenzo, *Kardar–Parisi–Zhang universality class for the critical dynamics of reaction–diffusion fronts*, J. Stat. Mech.: Theor. Exp., 023203 (2020).

[134] H. Dashti-Naserabadi, A. Ali Saberi, S. H. E. Rahbari, and H. Park, *Two-dimensional super-roughening in the three-dimensional Ising model*, Phys. Rev. E **100**, 060101(R) (2019).

[135] R. L. Herman and A. Rose, *Numerical realizations of solutions of the stochastic KdV equation*, Math. Comput. Simul. **80**(1), 164-172 (2009).

[136] M. A. Rodriguez, *Class of perfect 1/f noise and the low-frequency cutoff paradox*, Phys. Rev. E **92**, 012112 (2015).

[137] A. Bahraminasab, S.M.A. Tabei, A. A. Masoudi, F. Shahbazi, and M. R. R. Tabar, *Zero Tension Kardar-Parisi-Zhang Equation in (d + 1)-Dimensions*, J. Stat. Phys. 116(5-6), 1521-1544 (2004).

[138] J. Garcia-Ojalvo and J. M. Sancho, *Noise in Spatially Extended Systems* (Springer, Barcelona, 1999).

[139] S. Taverniers, F. J. Alexander, and D. M. Tartakovsky, *Noise propagation in hybrid models of nonlinear systems: The Ginzburg–Landau equation*, J. Comput. Phys. **262**, 313 (2014).

[140] J. Cardy, *Scaling and Renormalization in Statistical Physics* (Cambridge University Press, 1996).

[141] J. Asikainen, S. Majaniemi, M. Dubé, and T. Ala-Nissila, *Interface dynamics and kinetic roughening in fractals*, Phys. Rev. E *65*, 052104 (2002).

[142] T. Blanchard, L. F. Cugliandolo, M. Picco, and A. Tartaglia, *Critical percolation in the dynamics of the 2D ferromagnetic Ising model*, J. Stat. Mech. 113201 (2017)

[143] J. M. Lopez, M. Castro, and R. Gallego *Scaling of Local Slopes, Conservation Laws, and Anomalous Roughening in Surface Growth*, Phys. Rev. Lett. **94**, 166103 (2005).

[144] D. Pavlicek, *ferrofluid*, 2011 [onlinevisited on 2021-09-09], https://www.deviantart.com/dusanpavlicek/art/ferrofluid-252816677

[145] M. C. Cross and P. C. Hohenberg, *Pattern formation outside of equilibrium*, Rev. Mod. Phys. **65**, 851 (1993).

[146] I. Seric, S. Afkhami, and L. Kondic, *Interfacial instability of thin ferrofluid films under a magnetic field*, J. Fluid Mech. **755**, R1 (2014).

[147] D. Conroy and O.K. Matar, *Thin viscous ferrofluid film in a magnetic field*, Phys. Fluids **27**, 092102 (2015).

[148] D. Tseluiko and D. T. Papageorgiou, *Wave evolution on electrified falling films*, J. Fluid Mech. **556**, 361-386 (2006).

[149] H. Gotoda, M. Pradas, and S. Kalliadasis, *Nonlinear Forecasting of the Generalized Kuramoto–Sivashinsky Equation*, Int. J. Bif. Chaos **25**, 1530015 (2015).

[150] G. Schifani, T. Frisch, and M. Argentina and J. N. Aqua, *Shape and coarsening dynamics of strained islands*, Phys. Rev. E **94**, 042808 (2016).

[151] P. Keblinski, *Comment on Columnar Growth and Kinetic Roughening in Electrochemical Deposition*, Phys. Rev. Lett. **75**, 5 (1993).

[152] Y. H. Suh, D. W. Shin, and Y. T. Chun, *Micro-to-nanometer patterning of solution-based materials for electronics and optoelectronics*, RSC Adv. **9**, 38085 (2019).